

---

# **Germanium thin film integration on silicon substrates via oxide heterostructure buffers**

---

**Dissertation (kumulativ)**

**zur Erlangung des Grades eines Doktors der Naturwissenschaften  
(Dr. rer. nat.)**

**dem Fachbereich Physik der Universität Osnabrück vorgelegt von**

**Alessandro Giussani, Dipl.-Phys.**

**Osnabrück, im Februar 2010**



## Acknowledgements

First of all, I thank Dr. Thomas Schroeder and Prof. Hans-Joachim Müssig for giving me the chance to work in the Material Research Department of IHP and make my PhD there. In especial, I express my gratitude to Dr. Thomas Schroeder for supervising my activity throughout these three years and for his guidance in all the fields I have worked at. I also want to thank Prof. Joachim Wollschläger at the University of Osnabrück for accepting my candidature as a PhD student and following my work all along the way. I am grateful to Dr. Peter Storck and Siltronic AG for financing the heteroepitaxy project I was involved in.

The list of people I have to thank at IHP is pretty long, starting from Dr. Peter Zaumseil for his precious support and his teachings on x-ray diffraction; Hans Thieme for his help with molecular beam epitaxy; Dr. Jarek Dabrowski for his theoretical calculations; Dr. Ioan Costina and Dr. Rainer Kurps for support with surface analysis characterization; Dr. Guenter Weidner and Dr. Markus Andreas Schubert for transmission electron microscopy measurements and explanations; Mrs. Morgenstern and colleagues for scanning electron microscopy support; all the colleagues with whom I have shared these three years, namely, Mindaugas Lukosius, Lidia Tarnawska, Dr. Olaf Seifarth, Dr. Gunther Lippert, Dr. Grzegorz Lupina, Dr. Christian Wenger, Dr. Mario Birkholz, Christian Walczyk, Grzegorz Kozlowski, Piotr Dudek, David Kot, Oliver Skibitzki, Marvin Zöllner, Andreas Wilke, Alexander Fromm, Yvonne Heier, Felipe Dominguez, and Manja Krause. Special thanks go to Peter Rodenbach, who has worked with me in the heteroepitaxy project during his diploma thesis at IHP.

I also want to thank the colleagues from the University of Osnabrück, namely, Dr. Thomas Weisemöller, Sebastian Gevers, and Dr. Carsten Deiter for the collaboration on the study of praseodymia thin films and the measurements at HasyLab (*Hamburger Synchrotronstrahlungslabor*) in Hamburg; Dr. Dorin Geiger from TU Dresden for TEM support; the ESRF (*European Synchrotron Radiation Facility*) in Grenoble and the ID-32 beamline staff for the beam-time spent there, in particular Dr. Jérôme Roy and Dr. Sebastian Thiess for support and explanations; once more IHP for offering an internal German course, and the German teacher Dr. David James Prickett. Finally, I want to acknowledge DFG (*Deutsche Forschungsgemeinschaft*) and DAAD (*Deutscher Akademischer Austausch Dienst*) for providing financial support for participation to international conferences.



# Contents

<b>1 Introduction.....</b>	<b>7</b>
1.1 ENGINEERED SI WAFERS .....	7
1.2 APPLICATIONS .....	9
1.2.1 <i>Highly integrated microelectronics</i> .....	10
1.2.2 <i>Optoelectronics</i> .....	14
1.2.3 <i>Photovoltaics</i> .....	16
1.3 GE SUBSTRATES .....	18
1.3.1 <i>Czochralski Ge crystal growth</i> .....	18
1.3.2 <i>Thin film Ge substrates</i> .....	21
1.4 AIM OF THIS THESIS .....	28
<b>2 Oxide heterostructures as buffers for the integration of alternative semiconductors on the Si platform.....</b>	<b>30</b>
2.1 THE OXIDE BUFFER APPROACH.....	30
2.2 EXAMPLES OF SINGLE CRYSTALLINE OXIDE BUFFERS ON Si(111) .....	31
2.3 OXIDE BUFFER FLEXIBILITY: ISOMORPHISM AND POLYMORPHISM .....	33
2.4 THE CHOICE OF PRASEODYMIUM OXIDE AS BUFFER ON Si(111) .....	34
2.5 THE HETEROEPITAXIAL OVER-GROWTH OF THE BUFFER OXIDE.....	41
<b>3 Experimental background .....</b>	<b>43</b>
3.1 SAMPLE GROWTH.....	43
3.1.1 <i>Substrate</i> .....	43
3.1.2 <i>Molecular Beam Epitaxy</i> .....	44
3.1.3 <i>Preparation of the oxide buffer</i> .....	46
3.1.4 <i>Deposition of the Ge epilayer</i> .....	47
3.2 SAMPLE CHARACTERIZATION .....	48
3.2.1 <i>Main methods</i> .....	48
3.2.1.1 X-ray Diffraction .....	48
3.2.1.2 X-ray Reflectivity .....	62
3.2.2 <i>Additional methods</i> .....	66
3.2.2.1 Reflection High Energy Electron Diffraction .....	66
3.2.2.2 Photoelectron Spectroscopy .....	69
3.2.2.3 Dynamic Secondary Ion Mass Spectroscopy .....	72
3.2.2.4 Scanning Electron Microscopy .....	74
3.2.2.5 Transmission Electron Microscopy .....	76
<b>4 The influence of lattice oxygen on the initial growth behaviour of heteroepitaxial Ge layers on single crystalline PrO<sub>2</sub>(111) / Si(111) support systems .....</b>	<b>82</b>
<b>5 Atomically smooth and single crystalline Ge(111) / cubic Pr<sub>2</sub>O<sub>3</sub>(111) / Si(111) heterostructures: structural and chemical composition study.....</b>	<b>83</b>
<b>6 Defect Structure of Ge(111) / cubic Pr<sub>2</sub>O<sub>3</sub>(111) / Si(111) Heterostructures: Thickness and Annealing Dependence</b>	<b>84</b>
<b>7 Summary and outlook .....</b>	<b>85</b>

7.1	MOTIVATION .....	85
7.2	RESULTS .....	87
7.2.1	<i>In-situ growth study of Ge thin epifilms</i> .....	87
7.2.2	<i>Morphology and structure characterization of the Ge(111) epilayer</i> .....	88
7.2.3	<i>Defect structure of the Ge(111) epilayer</i> .....	89
7.3	OUTLOOK .....	90
	<b>Scientific visibility during the PhD .....</b>	<b>92</b>
	PUBLICATIONS IN PEER-REVIEWED JOURNALS.....	92
	PUBLICATIONS IN CONFERENCE PROCEEDINGS.....	93
	PRESENTATIONS AT CONFERENCES AND COURSES.....	93
	<b>Bibliography .....</b>	<b>94</b>

# 1 Introduction

## 1.1 Engineered Si wafers

The integration of single crystalline 100% epitaxial (epi) germanium (Ge) layers on (111)-oriented silicon (Si) substrates via a crystalline buffer oxide is based on the concept of *Si wafer engineering* (Fig. 1.1). An *engineered Si wafer* is a material that can be created and injected into the Si-manufacturing infrastructure, resulting in finished products that are unique and cannot be created with only a bare Si substrate.<sup>1</sup>

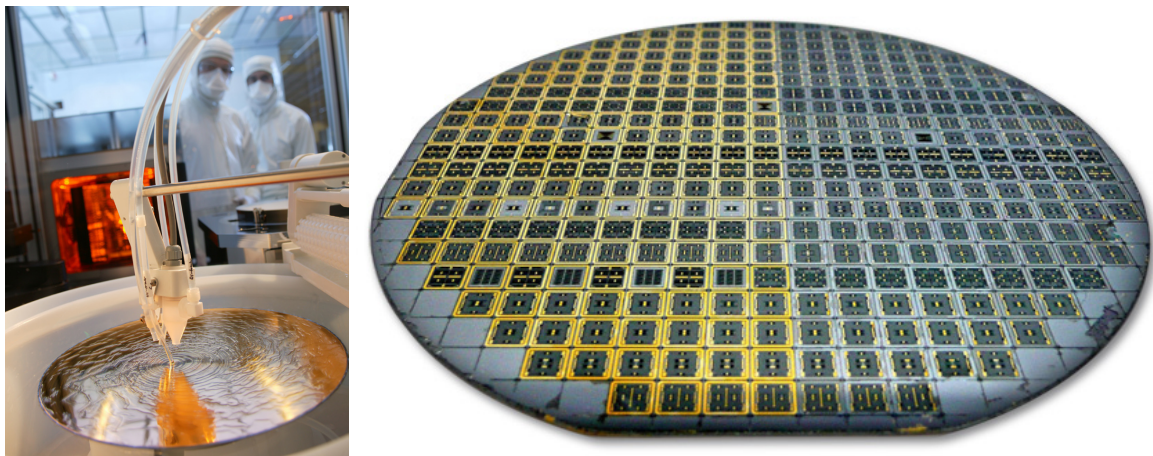


**Fig. 1.1: An example of Si wafer engineering, the Soitec's Smart Cut™ technology for Silicon-on-Insulator (SOI) wafer fabrication. Using standard semiconductor manufacturing equipment, SOI chips are produced, which generate less heat, consume less power, and have a lower overall operating cost with respect to conventional devices.**

It is a general trend in semiconductors that, as the lattice constant increases, the elastic modulus and the band gap decrease, whereas the electron mobility  $\mu_e$  is enhanced (Tab. 1.1). Thus, materials with bigger lattice constants present higher electron mobility, but suffer of increasing softness and lower band gap, which limit potential applications. The highest mobility semiconductors, e.g., indium antimonide (InSb), are available in small wafer diameter, are very expensive, and are relatively more defective with respect to Si substrates. The wafer engineering vision to combine large lattice constants on the Si platform is therefore intriguing, allowing furthermore processing compatible with the Si manufacturing environments. Crucial is to manage the lattice mismatch between the desired thin film and Si, which causes the formation of defects in the overlayer, mining the quality of the final product.

The requirements, which engineered Si wafers are supposed to meet, can be summarized by the following six key-points:<sup>2</sup>

- 1) The integrated material system is itself an active circuit element;**
- 2) The integrated material system serves as a buffer layer;**
- 3) The integrated material system can be dealt with, exploiting the mature Si wafer technology;**
- 4) The integrated material system exhibit an optimal combination of favorable thermal and mechanical properties;**
- 5) The integrated material thin film properties differ from the bulk ones;**
- 6) Large-diameter substrates of the integrated material can be produced.**

In the case of Ge integration on Si, single crystalline Ge thin film substrates are pursued because they

- 1) can be utilized as active element in infra-red photodetectors or multi-junction solar cells;
- 2) can be employed as epitaxial template for the over-growth of gallium arsenide (GaAs) and indium gallium phosphide (InGaP) for photovoltaic applications, owing to the minimal lattice and thermal mismatch between Ge and GaAs;
- 3) can be processed in clean-room making use of the standard tools employed for the mainstream Si flow, being the Ge thin films grown on standard Si support wafers;
- 4) can benefit of the higher thermal conductivity and mechanical stability of the Si support wafers;
- 5) can exhibit strain and quantum size effects, for instance enhanced two-dimensional hole gas (2DHG) mobilities and conductivity at room temperature (RT) in ultra-thin strained Ge quantum well (QW) incorporated into modulation doped heterostructures (MODH);<sup>3</sup>
- 6) could provide a solution to the problem of Ge material availability. Indeed, if the microelectronics industry decided to switch over to Ge, at the moment there would not be sufficient 200 and 300 mm wafers and suppliers to cover the market needs.

In the next chapter, the main prospective applications of thin epi-Ge films grown accordingly to the wafer engineering philosophy on Si are presented. The basics, the advantages and the drawbacks of the most common and successful methods for the preparation of epi-Ge layers are illustrated. Finally, the heteroepitaxial approach through high quality, single crystalline oxide buffers, subject of this thesis, is introduced.

	<i>Si</i>	<i>Ge</i>	<i>GaAs</i>	<i>InP</i>	<i>InSb</i>
<b><i>Electron mobility (cm<sup>2</sup>·V<sup>-1</sup>·s<sup>-1</sup>)</i></b>	1400	3900	8500	54000	77000
<b><i>Hole mobility (cm<sup>2</sup>·V<sup>-1</sup>·s<sup>-1</sup>)</i></b>	450	1900	400	200	850
<b><i>Effective density of states in valence band, N<sub>V</sub> (10<sup>18</sup>·cm<sup>-3</sup>)</i></b>	6.0	10.0	7.0	11.0	7.3
<b><i>Effective density of states in conduction band, N<sub>C</sub> (10<sup>16</sup>·cm<sup>-3</sup>)</i></b>	1.04·10 <sup>3</sup>	2.8·10 <sup>3</sup>	47	57	4.2
<b><i>Bandgap (eV)</i></b>	1.12	0.66	1.42	1.34	0.17
<b><i>Electron affinity, χ (eV)</i></b>	4.05	4.00	4.07	4.38	4.59
<b><i>Lattice constant (nm)</i></b>	0.5431	0.5658	0.5653	0.5869	0.6749
<b><i>Dielectric constant</i></b>	11.7	16.2	12.9	12.5	16.8
<b><i>Melting point, T<sub>m</sub> (°C)</i></b>	937	1412	1240	1060	527
<b><i>Thermal conductivity (W·cm<sup>-1</sup>·°C<sup>-1</sup>)</i></b>	1.30	0.58	0.55	0.68	0.18
<b><i>Linear thermal expansion (·10<sup>-6</sup>·°C<sup>-1</sup>)</i></b>	2.60	5.90	5.73	4.60	5.37

Tab. 1.1: Properties of high mobility semiconductors.<sup>4-6</sup>

## 1.2 Applications

Germanium is a hard, brittle semimetal that was discovered about one-half century ago as a potential semiconductor material in radar units and in transistors. Today, its market is continuously expanding. In 2007, the Ge worldwide end-use pattern was estimated to be as follows: polymerization catalyst for polyethylene terephthalate (PET), a commercially important plastic, 31%; telecommunications fiber-optics, 24%; infrared optics, 23%; electronics and photovoltaics, 12%; and other uses (such as phosphors, metallurgy, and chemotherapy), 10%. However, the domestic end-use pattern was significantly different, with infrared optics accounting for 50%; fiber-optics, 30%; electronics and photovoltaics, 15%; and other uses, 5%.<sup>7</sup> Germanium lenses and windows are transparent to mid- and long-wavelength infrared (MWIR: 3-8 μm; LWIR: 8-15 μm, respectively)<sup>6</sup> radiation, which allows

them to be employed in infrared optical systems in the same way that ordinary glass lenses and windows are used in visible-light optical systems. Ge is preferred to Si, which is about 6 to 7 times cheaper, because it offers a higher refractive index  $n$  in the MWIR ( $n_{\text{Ge}} = 4.01$  vs  $n_{\text{Si}} = 3.4$  at  $\lambda = 5 \mu\text{m}$ )<sup>8</sup> and a wider transmission spectrum in the LWIR.<sup>9</sup> Applications are navigation systems, detection and search equipment, optical imaging, and target evaluation systems for military operations, as well as firefighters search and rescue devices, surveillance night-vision goggles, and night vision systems in some higher luxury cars. In the telecommunications, germanium is employed as a dopant within the pure silica glass core of optical fibers, aiming at increasing the refractive index without absorbing light.

The other mentioned application fields, microelectronics, optoelectronics and photovoltaics, are closely related to the subject of this thesis and will therefore be dealt with in more detail.

### 1.2.1 Highly integrated microelectronics

Germanium is the material with which the first transistor was realized in 1947 (Fig. 1.2).<sup>4</sup> However, in the sixties it was abandoned in favor of silicon, mainly because of the poorer electrical properties of Ge oxide compared to  $\text{SiO}_2$ .

Here, the *Metal Oxide Semiconductor Field Effect Transistor* (MOSFET), the most important device for high-density *Integrated Circuits* (ICs) such as microprocessors and semiconductor memories, is considered (Fig. 1.3). Briefly, a common MOSFET is a four-terminal device that consists of a p-type semiconductor substrate into which two  $n^+$ -regions, the *source* and the *drain*, are formed, usually by ion implantation. The  $\text{SiO}_2$  film is typically formed by thermal oxidation of Si for a high quality  $\text{SiO}_2$ -Si interface. The insulator is named *gate dielectric*, as it is placed below the so called *gate* electrode (commonly heavily doped polysilicon covered with silicide). The basic device parameters are the channel length  $L$ , which is the distance between the two metallurgic  $n^+$ -p source and drain junctions; the channel width  $Z$ ; the insulator thickness  $d$ ; the junction depth  $r_j$ ; and the substrate doping  $N_A$ . In an IC, a MOSFET is electrically isolated from adjacent devices by means of a thick *field oxide* or *trenches* filled with insulator. When ground or low voltage is applied to the gate, the main channel is shut off, and the source-to-drain electrodes correspond to two p-n junctions connected back to back. When a sufficiently large positive bias is applied to the gate so that a surface inversion layer (or channel) is formed between the two  $n^+$ -regions, the source and the drain are then

connected by a conduction surface  $n$ -channel through which a large current can flow. The conducting of this channel can be modulated by varying the gate voltage  $V_G$  (for comprehensive understanding of MOSFET and other types of transistors consult Ref. <sup>10</sup>).



**Fig. 1.2: In 1947 Bell Labs' John Bardeen, Walter Brattain, and William Shockley invent the transistor, revolutionizing the entire electronics world. The team was awarded a Nobel Prize in 1956.**

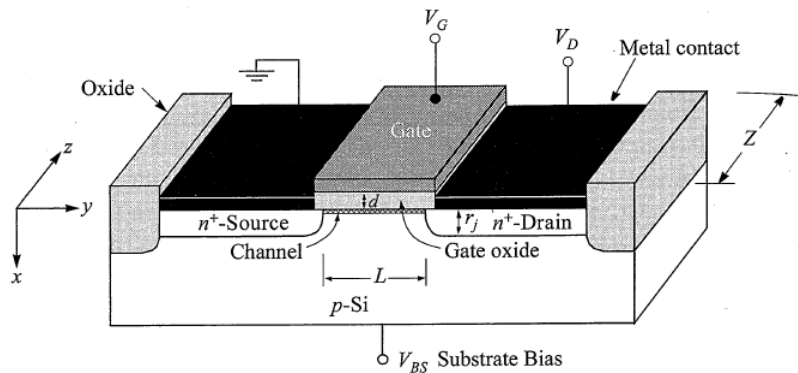


**Fig. 1.3: Schematic diagram of a MOSFET.<sup>10</sup>**

Over the past decades, the MOSFET has continually been scaled down in size; typical MOSFET channel lengths were once several  $\mu\text{m}$ , but modern ICs are incorporating MOSFETs with channel lengths of less than 50 nm. The main reason to make transistors smaller is to pack more and more devices in a given chip area. This results in a chip with the same functionality in a smaller area, or chips with more functionality in the same area. Since fabrication costs for a semiconductor wafer are relatively fixed, the cost per integrated circuits is mainly related to the number of chips that can be produced per wafer. Hence, smaller ICs allow more chips per wafer, reducing the price per chip. In fact, over the past 30 years the number of transistors per chip has been doubled every 2-3 years once a new technology node

was introduced (Fig. 1.4). This doubling of the transistor count was first observed by Gordon Moore in 1965 and is commonly referred to as *Moore's law*.<sup>11</sup>

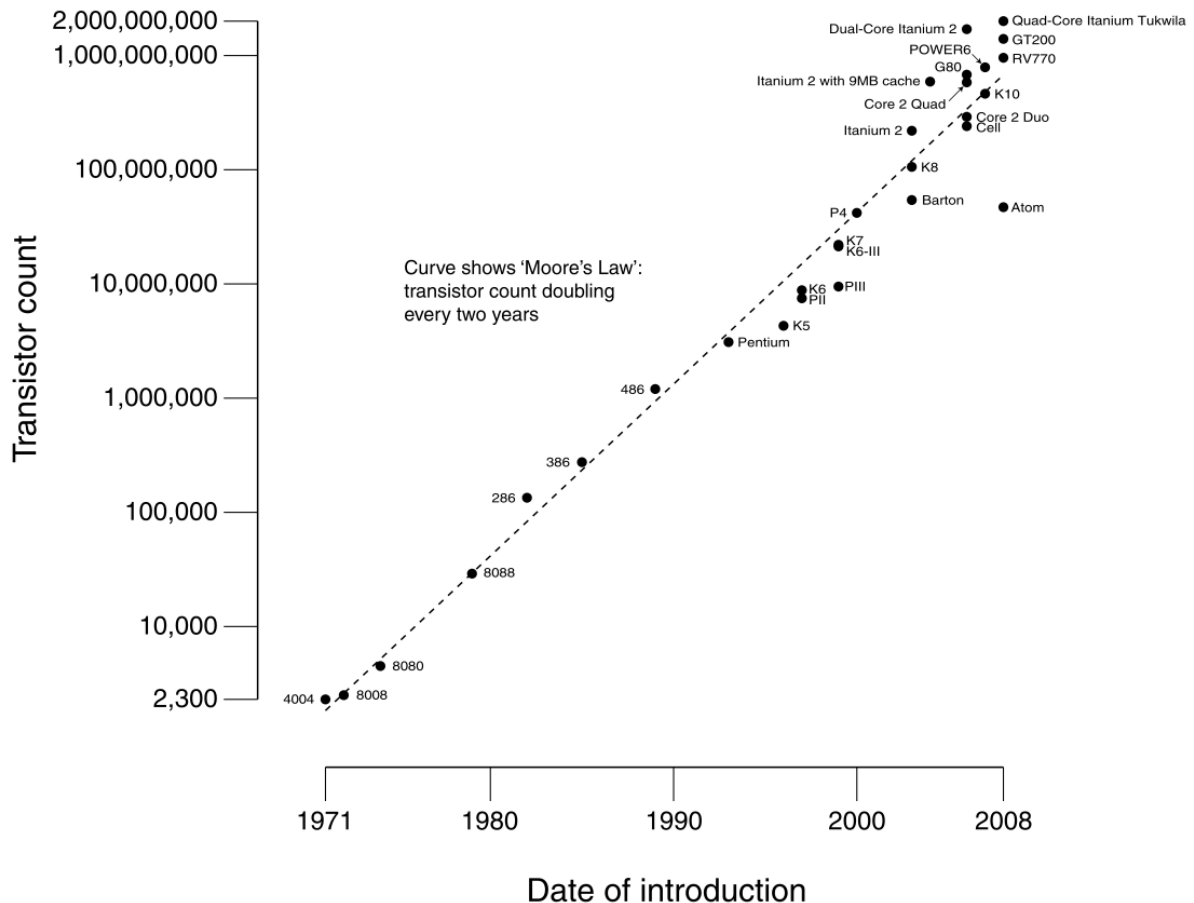


Fig. 1.4: CPU (Central Processing Unit) transistor counts 1971-2008 and Moore's Law.

However, already in the late 1990s, it became clear that drive current would no longer increase by a power-law with time, and that, unless drive current enhancements were introduced, scaling would come to an end. A solution was found in the implementation of strained Si,<sup>12</sup> an example of “*More than Moore*”, that is to say the introduction of novel materials into the mainstream silicon transistor technologies to assist ICs miniaturization. Another critical issue is represented by the shrinking of the SiO<sub>2</sub> gate oxide, whose thickness has nowadays reached the physical limit of ~ 1 nm, below which transistors suffer of intolerable gate leakage current, poor reliability and electron channel mobility degradation, rendering device scaling ineffective. In the last decade, high dielectric constant (*high-k*) materials have been widely investigated, aiming at replacing SiO<sub>2</sub>. High-k oxides can indeed match the desired equivalent SiO<sub>2</sub> thickness at a higher physical thickness.<sup>13</sup> The market-leader among the *Integrated Circuit Manufacturers* (ICMs), *Intel® Corporation*, claimed that its 45 nm silicon technology, the latest in production, employs a combination of new materials

including hafnium-based high-k gate dielectrics and metal gates. This new transistor breakthrough, Intel® Corporation guarantees, ensures that Moore's Law thrives well into the next decade.<sup>14</sup> On the other hand, *René Penning de Vries*, Chief Technology Officer of NXP, another preeminent ICM, predicts alternative scenarios to miniaturization for ICs. He recently announced that “*just as transistor density in production has increased, so too has the cost of developing the process that enables it. The result is that the most cost-effective IC solution today is no longer by default based on the smallest – and most expensive – CMOS technology available. So, Moore's Law, which dominated process technology in semiconductors for decades, will remain the driver in a limited number of high volume areas. But it may cease to exist the moment the boundaries of physical ability or economical feasibility are achieved. Trends in society all create significant market opportunities for companies who provide state-of-the-art ICs in areas such as energy-saving in consumer electronics and lighting, medical diagnostics equipment, food safety, and traffic management systems. Growth of these markets is not hindered by the economic downturn, since most of the chip innovations offer great return-on-investment; the product costs are often earned back easily on energy saving, less costs for medical care, less economic damage through traffic congestion. This way, real need-driven innovations in semiconductors can often pay for themselves*”.<sup>15</sup>

In this context of demand for innovation in microelectronics, Ge strongly returns on stage as promising candidate for high mobility channel material in *Complementary Metal Oxide Semiconductor* (CMOS) devices.<sup>16</sup> It indeed exhibits higher electron and hole mobility than Si, and higher hole mobility and density of states in the conduction band than any III-V semiconductor (Tab. 1.1), as well as a low dopant activation energy and a similar electron affinity as Si, permitting larger drive currents.<sup>5,17</sup> As already mentioned, GeO<sub>2</sub> shows poor thermodynamic and electrical properties<sup>5,18</sup> as well as low conduction and valence band offsets at the Ge / GeO<sub>2</sub> interface<sup>19</sup> so that it cannot be utilized as gate insulator. High-k oxides represent the choice (e.g., HfO<sub>2</sub> (Refs. <sup>5,20-24</sup>), ZrO<sub>2</sub> (Ref. <sup>5</sup>), Al<sub>2</sub>O<sub>3</sub> / HfO<sub>2</sub> (Ref. <sup>25</sup>), and Al<sub>2</sub>O<sub>3</sub> / Y<sub>2</sub>O<sub>3</sub> (Ref. <sup>26</sup>)) and this is not a drawback with respect to Si-based CMOS any longer, since, at the current Si technology node, SiO<sub>2</sub> needs anyhow to be replaced with novel high permittivity dielectrics. Rather, the instability of GeO<sub>2</sub>, in the past an enormous handicap, now turns into a major advantage. Indeed, it has been demonstrated that for the same deposition conditions, the interfacial oxide thickness is significantly lower in the case of a Ge substrate compared with Si.<sup>24</sup>

In conclusion, high quality Ge integration on Si wafers is a hot topic today in transistor research, triggering the development of appropriate engineered Si wafer products.<sup>27</sup>

## 1.2.2 Optoelectronics

Optoelectronics is the study and application of electronic devices that create, detect and control light.<sup>28</sup> One such device is the photodetector, which convert optical signals into electronic ones.<sup>10</sup> In this technology, Ge is an interesting subject of research, owing to its ability to absorb in the near-infrared (NIR: 0.75-1.4  $\mu\text{m}$ ) and short-wavelength infrared (SWIR: 1.4-3  $\mu\text{m}$ ),<sup>6</sup> at wavelengths  $\lambda$  at which Si has a very low or null absorption coefficient  $\alpha$  (Fig. 1.5).

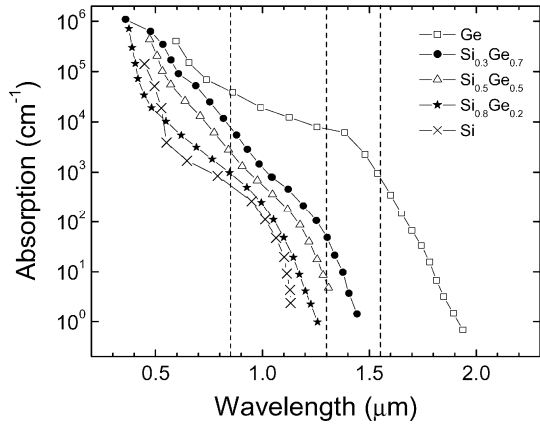


**Fig. 1.5: Plot of absorption coefficient versus wavelength for relaxed SiGe layers with [Ge] ranging from 0 to 100 at %.<sup>29</sup>**

For instance, at a wavelength of 850 nm, that is the standard Local Area Network (LAN) optical communication wavelength, the absorption length  $\alpha^{-1}$  in Ge is only a few hundred nm versus  $\sim 20 \mu\text{m}$  in Si, opening the way to extremely fast detectors due to the thin absorbing layer needed. In addition, Ge shows larger mobilities than Si, permitting not only higher device speed, but also operation at lower voltages, a key priority for integrated detector applications. As an example, Fig. 1.6 reports a cross-section sketch of a *lateral PIN photodetector* that utilizes a Ge film deposited on a ultra-thin SOI substrate<sup>29,30</sup> (consult Ref. <sup>10</sup> and Ref. <sup>31</sup> for details about photodetectors and SOI technology, respectively). In this design, the high absorption coefficient of the Ge layer allows the absorbing region to be kept very thin, while the buried oxide serves to prevent any carriers generated in the underlying Si from reaching the top electrodes. The SOI layer is also kept as thin as possible, not only to maintain maximum efficiency in the absorbing region, but also to minimize the amount of Si available for diffusion into the Ge layer upon subsequent annealing.<sup>30,32</sup> In fact, contamination of the Ge layer purity with even a small amount of Si can reduce the detector efficiency, especially at longer wavelengths (see Fig. 1.5). Finally, metal fingers are defined over the

implanted electrodes, with the aim of reducing the series resistance of the device, which is crucial for high-speed operation.

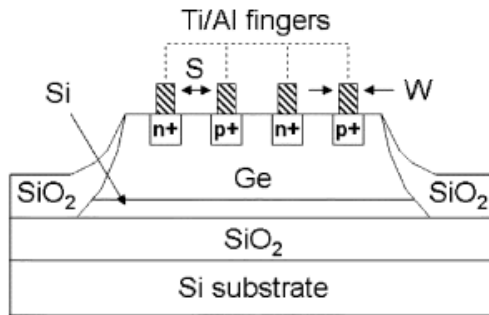


**Fig. 1.6: Cross-section schematic of a Ge lateral PIN photodetector on SOI.<sup>30</sup>**

This type of photodiodes showed bandwidths as large as 29 GHz, peak quantum efficiencies as high as 46% and low operational voltages and dark currents. Of course, improvements can still be achieved, creating more functional device architectures and reducing the defect density in the Ge film, which affect the dark current. In this perspective, it looks reasonable to expect better device performances if *Ge-on-Insulator* (GeOI) heterostructures are employed, which would at least resolve the issue of Si in-diffusion into the Ge film from the SOI substrate.

Ge-based optoelectronic devices like the presented photodetector have potential for integration with Si-based CMOS and SiGe *heterobipolar transistors* (HBTs) (see for example Fig. 1.7).<sup>33-35</sup> In addition, considering the small lattice and thermal mismatch between Ge and GaAs,<sup>36</sup> Ge thin films could also be utilized as virtual substrates for GaAs growth to fabricate *light-emitting diodes* (LEDs) and lasers within the mainstream Si technology, paving the way to the long-dreamed monolithic combination of III-V materials-based optoelectronics with Si-based microelectronics.

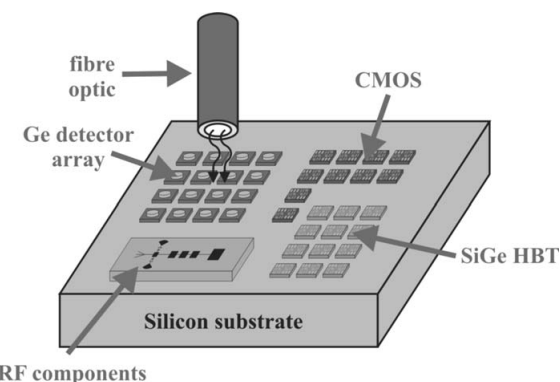


**Fig. 1.7: Schematic diagram of a potentially cost-effective Ge photodetector array, integrated on a Si chip with Si-CMOS and SiGe-HBT devices for optical communication.<sup>35</sup>**

### 1.2.3 Photovoltaics

Harvesting energy directly from sunlight using photovoltaic (PV) technology is a way to address growing global energy needs with a renewable resource, while minimizing detrimental effects on the environment by reducing atmospheric emissions. Huge potential is available, considering that, of the over  $1.5 \cdot 10^{22}$  J (15000 EJ) of solar energy that reach Earth everyday, only approximately 1.3 EJ are consumed daily by human activity.<sup>37</sup>

A photovoltaic device, or solar cell, converts photons directly into electrical charges that are used to energize an external circuit (Fig. 1.8(a)).

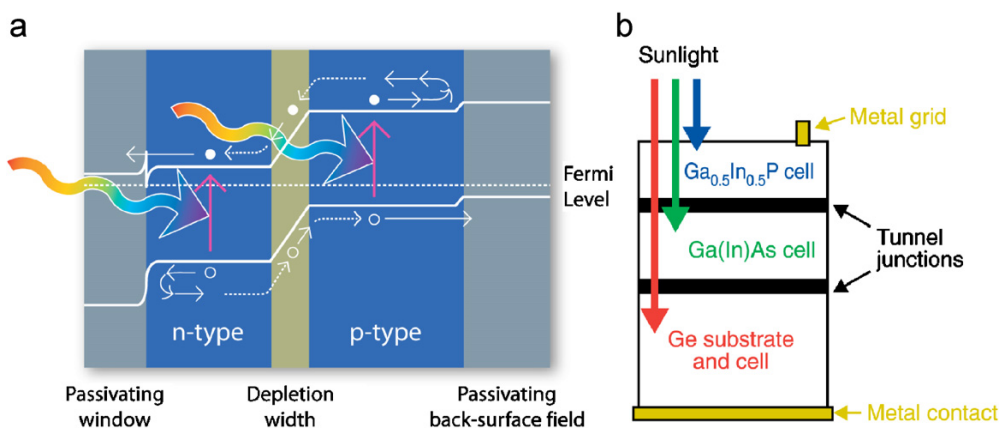


**Fig. 1.8:** (a) Schematic describing the functioning of a solar cell (not to scale). The curved white arrows show how the minority carriers are repelled from the cladding layers and separated in the field region. (b) Structure of three-junction GaInP / Ga(In)As / Ge cell.<sup>38</sup>

Sunlight is absorbed by the solar cell, exciting valence band electrons into the conduction band. Excess minority carriers are thus photo-generated, namely holes in n-type material and electrons in p-type material. The solar cell separates the excess minority carriers from the majority carriers at a p-n junction and delivers them to an outside circuit, as shown by the white arrows in Fig. 1.8(a). Some of the excess carriers recombine before reaching the p-n junction and are therefore lost in the process. The biggest challenge of creating a high-efficiency solar cell is to remove all defects that can lead to non-radiative recombination (radiative recombination can also decrease the efficiency of a solar cell, but cannot be entirely eliminated, because it represents the reverse of the absorption process.) For high-quality epitaxial layers, excess carriers mainly recombine at the front and back surfaces of the solar cell. This problem can be limited by continuing the crystal lattice with a different material with a larger bandgap, to reduce the concentration of defects and build-in a field that deflects

the minority carriers. In general, a potential barrier with a height of about five times the *thermal energy*  $kT$  ( $\sim 25\text{meV}$ , being the Boltzmann constant  $k = 8.617343 \cdot 10^{-5} \text{ eV}\cdot\text{K}^{-1}$ ) is sufficient to contain the excess carriers in the active region (the surfaces around the perimeter of the solar cell cannot be passivated as effectively as the front and back surfaces, but do not usually dominate the device performance). A multi-junction cell combines two or more of the structural units shown in Fig. 1.8(a) with highly doped shorting (tunnel) junctions or some other means of interconnection. Today's commercial high-efficiency multi-junction cells are grown on Ge substrates with three active junctions, as shown in Fig. 1.8(b). The spectrum is naturally sorted as each subcell passes light of sub-bandgap energies on to the lower subcells. Each subcell includes a p–n junction with passivation (cladding) layers on the front and back, as shown in Fig. 1.8(a). In this way, the broad solar spectrum is divided into smaller sections, each of which can be converted to electricity more effectively, permitting cell efficiencies beyond the *Shockley-Queisser theoretical limit* for single-junction cells.<sup>39</sup> The highest photo-electric efficiencies so far reported, around 40%, have been indeed achieved with GaInP / GaInAs / Ge multi-junction solar cells.<sup>40,41</sup> However, although on the one hand Ge substrates account for more than 80% of satellite PV applications,<sup>7</sup> 94% of the solar cells manufactured for terrestrial purposes were still Si-based in 2005.<sup>42</sup> The main reason resides in the high costs of electronic grade germanium versus silicon ( $\sim 1240 \text{ US\$ / kg}$  versus  $\sim 50 \text{ US\$ / kg}$ ).<sup>43</sup> Two approaches, which can run parallel, are under study to open the III-V compound semiconductor-on-Ge PV technology to terrestrial mass-production. On one side, intense research efforts are invested in the field of engineered Si wafers to accomplish the preparation of high quality, single crystalline Ge films on the mature and cheap Si platform, aiming at replacing the use of 100% *Czochralski* (CZ) Ge wafers as Ge substrates (see next chapter). On the other side, the strategy of reducing the amount of semiconductor material per watt (W) of electricity generated leads to the concept of *concentrator*. Such a device employs mirrors or lenses to focus the sunlight onto a tiny solar cell and it is often mounted on a solar tracker in order to keep the focal point upon the cell as the Sun moves across the sky. Furthermore, it is noted that, especially for space applications, Ge-based solar cells have shown superior radiation-resistance compared to Si cells.<sup>44</sup> In conclusion, Ge is a strong player in boosting solar energy, which currently supplies less than 0.1% of the world's electricity, to become one of the primary energy sources in the future.

## 1.3 Ge substrates

### 1.3.1 Czochralski Ge crystal growth

Nowadays, the highest quality Ge single crystals are grown by the *Czochralski pulling technique*.<sup>4</sup> The growth process is sketched in Fig. 1.9.

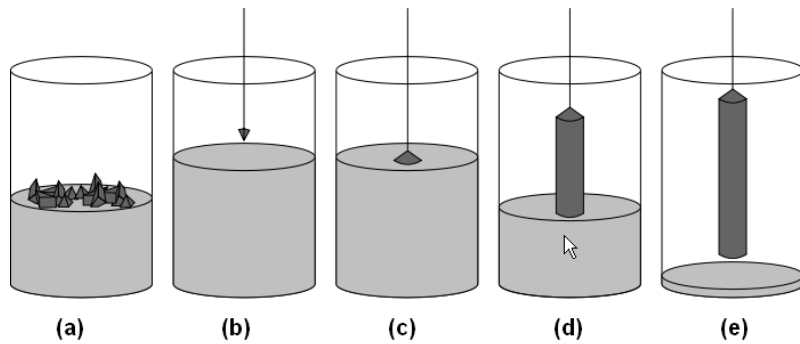


**Fig. 1.9: The Czochralski growth process. (a) Melting of the starting material; (b) introduction of the seed crystal; (c) beginning of the crystal growth; (d) crystal pulling; (e) formed crystal with a residue of melting material.**

The starting material has to be pure, particularly with respect to electrically active impurities. The requested degree of purity depends on the application. For instance, the concentration of electrically active impurities in the starting material must not exceed  $10^{13} \text{ cm}^{-3}$  for the growth of infrared grade and electronic grade germanium single crystals, and  $10^{11} \text{ cm}^{-3}$  for  $\gamma$ -ray detector applications. The starting material is melted down in a crucible, which is usually made of graphite (Fig. 1.9(a)). Dopant impurity atoms can be added to the molten intrinsic Ge in precise amounts, either in elemental form or in solid solution in Ge. A seed crystal, mounted on a rod, is lowered down close to the melt surface and allowed to get in thermal equilibrium with the melt, while rotating (Fig. 1.9(b)). The seed is usually a small cylinder cut from a single crystal of Ge, the cylinder axis being along the crystallographic direction of the crystal to be pulled. The seed is then dipped into the melt (Fig. 1.9(c)) and finally pulled upwards, always under rotation (Fig. 1.9(d)). By precisely controlling the temperature gradients, rate of pulling and speed of rotation, it is possible to extract a large, single-crystal, cylindrical ingot from the melt (Fig. 1.9(e) and Fig. 1.10). The pulling ambient can be any inert gas, or  $\text{H}_2$ , or vacuum. Pulling under vacuum is not suitable for large diameter crystals, given the large amount of latent heat of fusion to be removed ( $0.0025 \text{ J / kg}$  for Ge) and the relatively low thermal conduction in the solid Ge (only  $25.14 \text{ W / m}\cdot\text{K}$ , compared to  $147 \text{ W / m}\cdot\text{K}$  for  $\text{Si}$ ).

m·K for Si). Typically two pressure ranges can be applied, first slightly above atmospheric pressure and secondly 10 - 30 mbar.

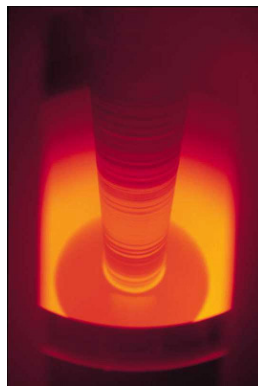


**Fig. 1.10: View of the growing Ge crystal inside the furnace. One can discern the relatively bright (yellow) meniscus ring at the lower end of the crystal cylinder.<sup>4</sup>**

Beside electrically active impurities, another critical issue is dislocations. When the seed crystal is dipped into the melt, dislocations are generated because of the high thermal stresses induced by the temperature shock. Due to the high stress and temperature in the crystal, the dislocations receive enough energy to spread into adjacent glide planes by cross slip, climb and multiplication processes. Since in diamond structure crystals the {111} planes are the main glide planes, which are oblique to the axis of a crystal pulled in a <100> or <111> direction, dislocations will glide out and terminate at the crystal surface, provided that the seed crystal is reduced in diameter and fast pulled for a few centimeters. This principle was originally observed by *Dash*,<sup>45,46</sup> after whom such dislocation annihilation approach was named *Dash necking*. Moreover, at the end of the pulling process, when the crystal has to be withdrawn from the residual melt, the thermal shock at this separation can lead to stress-generated dislocations running back up into the solid all over the still plastic temperature range (above 500°C), and consequently to yield losses. To avoid this, the end of the crystal is grown tapered in a cone to a very small or point contact diameter withdrawal. Compared to Si, Ge crystals have larger weight, lower mechanical strength, lower thermal conductivity and diffusivity and higher thermal expansion. All this imposes the use of larger seed and neck diameters for similar crystal lengths and increase the generation of thermal stresses in the material during the crystal growth process. However, by optimizing the necking process, the cone growth stage and other growth parameters, dislocation-free Ge single crystals up to 300 mm in diameter can be produced.<sup>47</sup> The process of transforming an as-grown crystal into thin wafers with damage-free, mirror-like, clean surfaces typically requires a combination of purely mechanical machining steps, like cutting and grinding, chemical steps (wet etching,

cleaning), and mixed process steps such as *chemical-mechanical polishing* (CMP) where an interplay between chemical and mechanical removal mechanisms exists (Fig. 1.11 and 1.12).

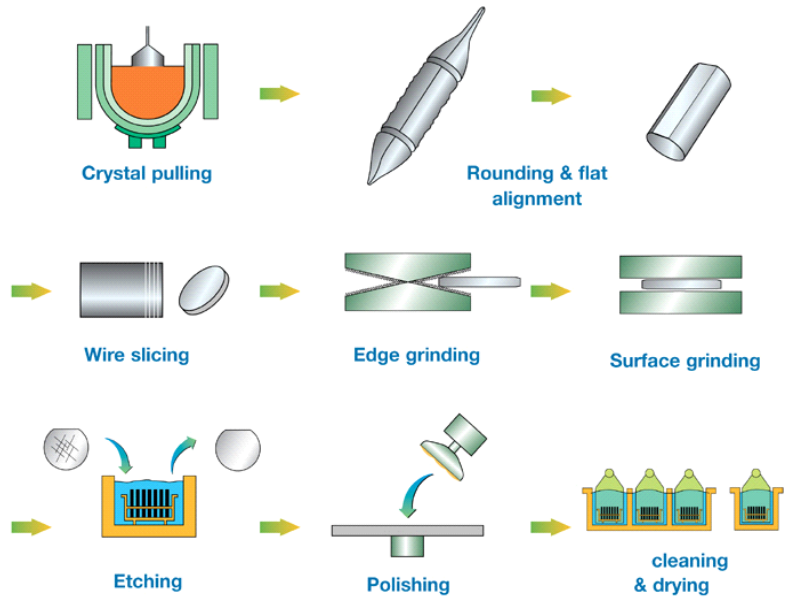
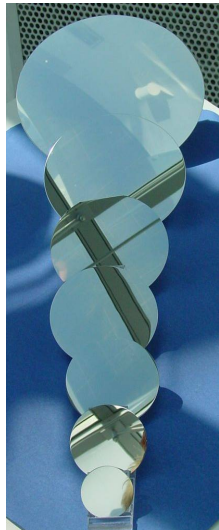


Fig. 1.11: Schematic flow of the Ge wafer production process.<sup>4</sup>

The majority of dislocation-free Ge crystals produced today are highly-doped 4 inch (100 mm) diameter wafers, used as substrates in high-efficiency GaAs solar cells for space telecommunications. No mass-market applications are targeted yet, as Ge substrates are still too expensive. The high costs reside not only on the large price of electronic grade Ge compared to Si, but also on the extremely poor production yield. Indeed, the Ge wafer fabrication techniques were originally developed for Si, without considering that Ge has a much lower tensile strength than Si (40-95 mPa versus 700-7000 mPa) and is therefore much more prone to subsurface damage as a result of mechanical stresses occurring during abrasive machining. This causes a noticeable amount of wafers to break during handling, sawing, and heating. Very recently, University of Utah engineers devised a new way to cut thin wafers of Ge, known as *wire electrical discharge machining* (WEDM).<sup>43,48</sup> The new slicing method is expected to reduce production costs of more than 10%, according to the germanium wafer-maker *Sylarus Technologies*,<sup>49</sup> but this is not yet sufficient to open the way to employment of Ge CZ substrates for terrestrial PV applications.

Therefore, alternative solutions are under study. A cost-effective approach to the fabrication of Ge substrates is represented by the preparation of high quality, single crystalline Ge thin films on the cheap canonical Si platform via wafer engineering, as described in the following paragraph.



**Fig. 1.12: Photograph of dislocation-free Ge wafers with diameters ranging from 2 in (50 mm) to 12 in (300 mm).<sup>4</sup>**

### 1.3.2 Thin film Ge substrates

**Ge films directly on Si:** A viable means to the integration of Ge on Si, on a global scale over the whole wafer or on a local scale over the area of the future device, is heteroepitaxy. Flat Ge layers deposited directly on Si have been achieved by using low growth temperatures ( $\sim 350^{\circ}\text{C}$ ). In this way, 3D island nucleation, resulting from the large lattice mismatch of 4.2% between Ge and Si, is inhibited.<sup>50-55</sup> Then, deposition can be continued at higher temperatures ( $\sim 750^{\circ}\text{C}$ ) in order to reduce the overall deposition time, as shown by Hartmann et al.<sup>56</sup> Yet, *post-deposition annealings* (PDAs) in the range  $(750\text{-}890)^{\circ}\text{C}$  are necessary to reduce the *threading dislocation density* (TDD). TDD values of  $\sim 10^7 \text{ cm}^{-2}$ ,  $8\cdot 10^8 \text{ cm}^{-2}$ , and  $2\cdot 10^9 \text{ cm}^{-2}$  were found at the surface of  $\sim 2.5 \mu\text{m}$ - thick Ge films on Si(001), Si(011), and Si(111) substrates, respectively. Similar results were achieved by Choi et al. (Ref. <sup>57</sup>) and Luan et al. (Ref. <sup>58</sup>) by cycling low and high temperature deposition steps and annealing. However, if PDAs are effective in lowering the TDD, as a drawback they induce Si diffusion from the Si substrate into the Ge film, mining the purity of the Ge epi-layer.<sup>32,56,59</sup> This could represent a problem, especially for technologies demanding ultra-thin and ultra-pure Ge layers.

**Compositionally graded SiGe graded buffer:** Lower TDDs can be obtained by growing Ge on a SiGe graded buffer. The principle of relaxed graded buffer is to introduce the 4.2% lattice mismatch between Si and Ge gradually, resulting in a disperse, three-dimensional

misfit dislocation network. Strain-relieving glide of threading dislocations is facilitated, preventing the accumulation of mismatch strain. Because threading dislocations present in the initial layers can also be used to relieve strain in subsequent layers, the nucleation of additional dislocations is suppressed as the graded layer growth progresses.<sup>60</sup> By repeating the low-mismatched layer sequence many times, a graded composition layer is achieved in which relaxation to high levels of mismatch can be accomplished with the retention of low TDD. However, a complication arises during thick grades to high Ge concentrations. The characteristic crosshatch surface roughness and the underlying strain fields of the misfit array can overlap, blocking threading dislocation glide and leading to dislocation pile-ups.<sup>61</sup> The formation of these pile-ups necessitates the nucleation of additional threading dislocations, as the trapped threading dislocations can no longer contribute to strain relief (Fig. 1.13).

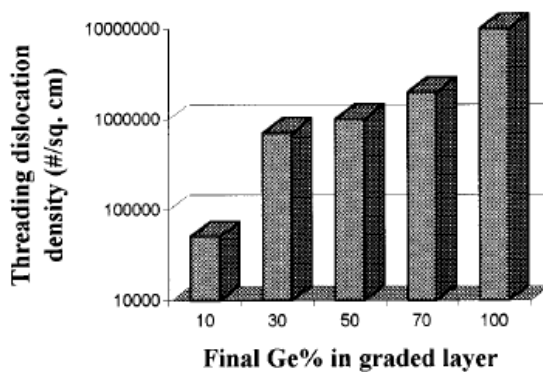


**Fig. 1.13:** Threading dislocation density versus increasing final [Ge] in the graded layer.<sup>61</sup>

It was shown that the incorporation of a CMP step in the middle of the growth allows the realization of a relaxed graded buffer to 100% Ge at 10% Ge  $\mu\text{m}^{-1}$  with a final TDD of  $\sim 10^6$   $\text{cm}^{-2}$  (Fig. 1.14).<sup>62</sup> Thickness of the SiGe buffer is typically in the range of several  $\mu\text{m}$ .

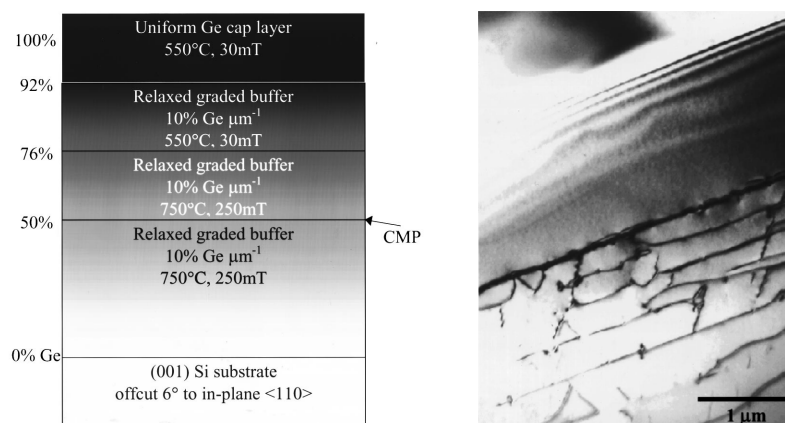


**Fig. 1.14:** (Left) Schematic of the structure and growth conditions of a 100% Ge / SiGe / Si heterostructure; (right) cross-sectional TEM image of the upper graded region and uniform Ge cap.<sup>62</sup>

**Selective epitaxy:** However, for greater ease of integration with Si-CMOS, a defect reduction solution involving minimal epi thickness (to minimize thermal expansion mismatch stress as well as to meet planarity requirements for Si processing) and minimal thermal budget (to allow addition of Ge at any point in the process without degrading the MOS transistor elements) is highly desirable. Researchers have shown that these requirements may be met by selective growth of Ge in small *vias* (diameter  $\leq 200$  nm) through a dielectric mask. One such approach is the so-called *Aspect Ratio Trapping* (ART). Ge layers as thin as 450 nm are deposited by *chemical vapor deposition* (CVD) in  $\text{SiO}_2$  trenches having *aspect ratio* ( $\text{AR} = \text{trench height} / \text{width}$ )  $> 1$ . Trenches are fabricated by conventional photolithography and *reactive ion etching* (RIE) techniques. As seen in Fig. 1.15, threading dislocations are trapped by a  $<100>$ -oriented sidewall, leading to a defect-free top epilayer on Si.<sup>63</sup> One shortcoming of ART is that it has been proven to be effective only for narrow strips with dimensions less than 1  $\mu\text{m}$ . However, ART combined with *epitaxial lateral overgrowth* (ELO)<sup>64</sup> was demonstrated to create large areas of low-defect-density Ge on Si (Fig. 1.16). Dislocations were trapped inside oxide trenches, after which Ge was grown laterally to form very long, 20  $\mu\text{m}$  wide strips. Finally, Ge CMP was used to flatten the  $\{113\}$ -faceted strips to make the film suitable for device application. Non-coalesced Ge strips showed a defect density as low as  $1.6 \cdot 10^6 \text{ cm}^{-2}$ .<sup>65</sup>

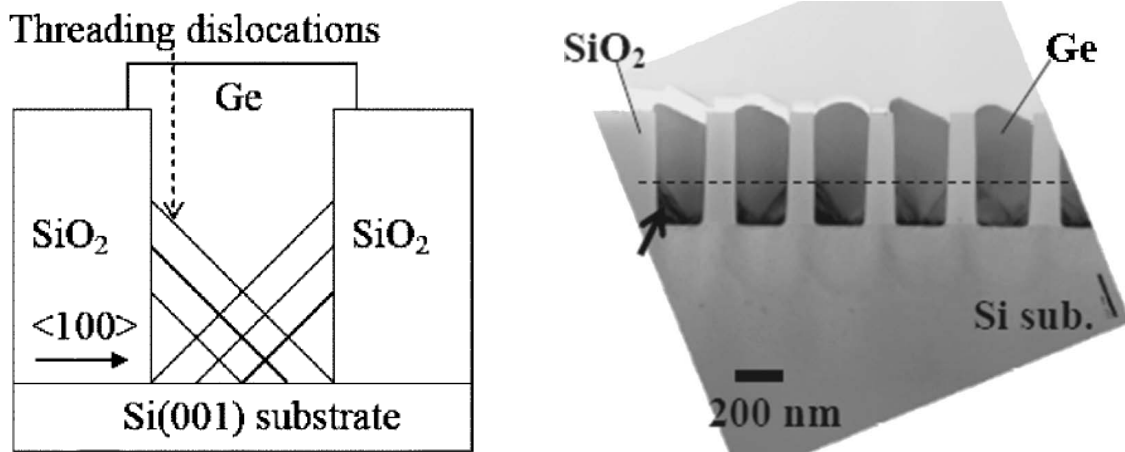


**Fig. 1.15:** (Left) Cross-sectional schematic illustrating the ART approach; (right) cross-sectional TEM of Ge in trenches of 200 nm width ( $\text{AR} = 2.45$ ), showing dislocations originating at the Ge / Si interface trapped by the oxide sidewall and defect-free Ge at the top of the trenches. The dashed line indicates where AR is 1. (Ref. <sup>63</sup>)

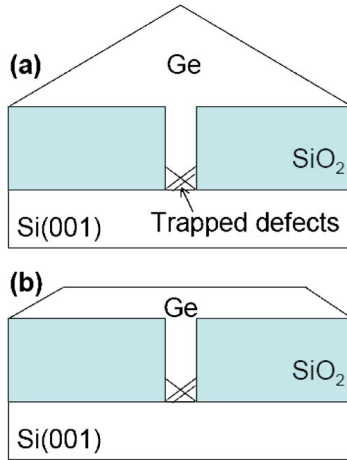
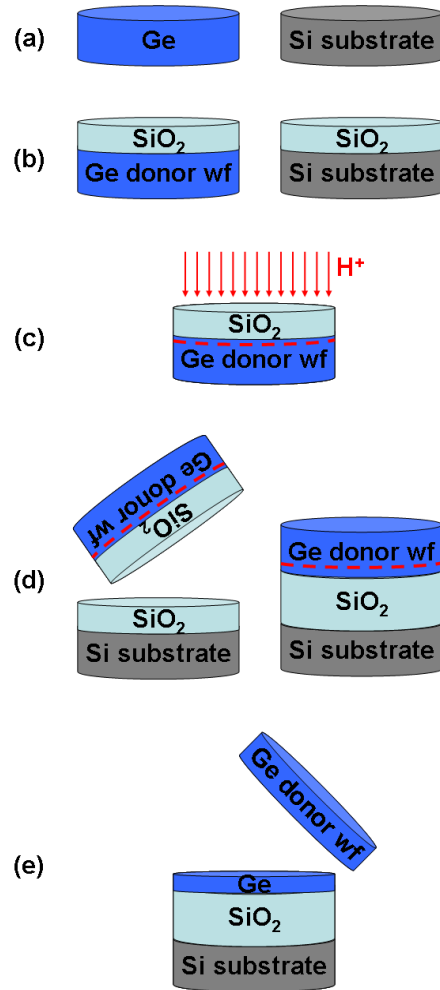


Fig. 1.16: Schematics of ELO Ge with ART after (a) Ge overgrowth and (b) Ge CMP.<sup>65</sup>

**Germanium-on-Insulator Technology:** Another way of achieving high quality, single crystalline Ge thin films on the mainstream Si platform is integrating Ge onto Si via a thin oxide layer, to build-up a GeOI heterostructure. The three main techniques to realize GeOI substrates are layer transfer, Ge condensation and Ge epitaxial overgrowth of single crystalline oxide buffers.

**Layer transfer approach:** Layer transfer allows the fabrication of a thin Ge substrate, using a small amount of Ge and a cheap Si wafer as support. The most commonly used technique in the field is the Smart Cut™ technology (Fig. 1.17), which was first developed on Si.<sup>6,31,66</sup> A Ge donor substrate (either a Ge wafer or epitaxial Ge) is subject to a HF-based cleaning, which removes particles at a high rate, maintaining the surface roughness comparable to the starting material. Then, owing to the instability of Ge oxide,<sup>67</sup> a SiO<sub>2</sub> film with a thickness of a few 100 nm is grown by *plasma enhanced chemical vapor deposition* (PECVD) on top of the Ge donor wafer and densified at 600°C. Such a layer will constitute a part of the final *buried oxide* (BOX). Afterwards, the capped germanium wafer undergoes H<sup>+</sup> implantation with doses and energies in the mid 10<sup>16</sup> at / cm<sup>2</sup> and in the 50 to 100 keV range, respectively. Ion implantation weakens the Ge crystal at the desired depth. This acts as an atomic scalpel, lifting off from the donor wafer a thin Ge layer that is “transferred” onto a thermally oxidized Si base substrate by means of room temperature hydrophilic bonding. The resulting product is a GeOI structure, whose surface is fully compatible with device processing after some post-bonding treatments, like annealing and polishing (Fig. 1.18). The main difficulty in the whole process consists in managing the splitting, due to the difference between the thermal expansion coefficients of Si and Ge.



**Fig. 1.17: Smart Cut™ approach. (a) Initial Ge donor wafer (wf) and Si substrate; (b) SiO<sub>2</sub> formation; (c) H<sup>+</sup> implantation into the Ge donor wafer; (d) bonding; (e) splitting, annealing and polishing.**

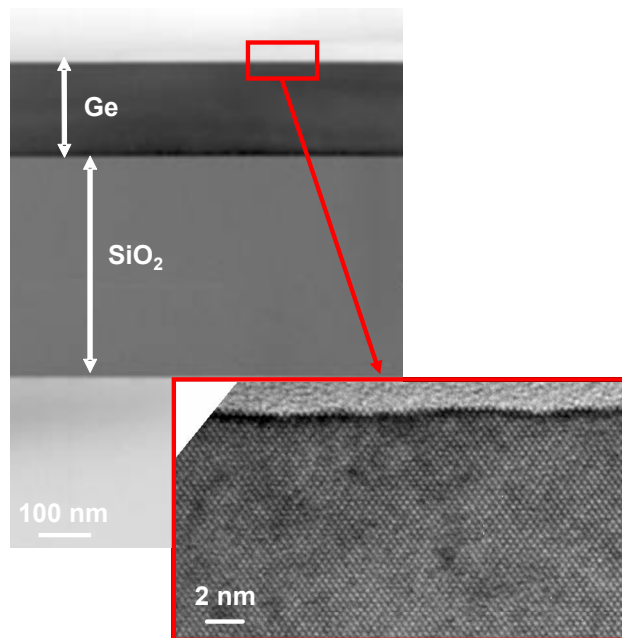


**Fig. 1.18: TEM cross-section images of a Smart-Cut™ GeOI wafer.<sup>4</sup>**

A clear advantage of this technique is the recycling of the expensive Ge donor wafer which can be used several times. Furthermore, GeOI substrates can be handled like a silicon wafer in microelectronics production lines, allowing high-volume throughput, process reproducibility, and consistent quality. GeOI substrates from 100 mm up to 200 mm in diameter and with a top Ge layer thickness ranging from 40 nm up to 200 nm depending on targeted applications have been realized. GeOI heterostructures obtained from bulk Ge donor wafers present no significant strain and defect densities as low as  $10^5 \text{ cm}^{-2}$ . Electrical characterization shows interface state densities at the Ge /  $\text{SiO}_2$  interface around  $5 \cdot 10^{12} \text{ eV}^{-1} \cdot \text{cm}^{-2}$ , hole and electron mobility up to 350 and  $300 \text{ cm}^2 \cdot \text{V}^{-1} \cdot \text{s}^{-1}$ , respectively.<sup>68</sup> Finally, it must be mentioned that the Smart Cut<sup>TM</sup> technology is not the only layer transfer approach. Hydrophobic direct-wafer bonding, along with H-induced layer splitting of Ge, was successfully employed to transfer 700 nm-thick, single crystal Ge(001) films to Si(001) substrates without using a metallic bonding layer. The metal-free nature of the bond makes the bonded wafers suitable for subsequent epitaxial growth of triple-junction GaInP / GaAs / Ge solar cell structures at high temperatures, without concern about metal contamination of the active region of the device. Triple-junction solar cells structures grown on such Ge / Si templates by *metal organic chemical vapor deposition* (MOCVD) exhibit comparable photoluminescence intensity and minority carrier lifetime to a control structure grown on bulk Ge.<sup>69</sup>

**Ge condensation technique:** GeOI layers can also be produced by oxidizing a low Ge-content, strained SiGe layer, previously grown epitaxially on a SOI wafer (Fig. 1.19(a)). This fabrication method is called the *Ge condensation technique*.<sup>70</sup> It exploits the instability of SiGe alloys upon oxidation at high temperatures, which leads to the formation of a mixed oxide of  $\text{SiO}_2$  and  $\text{GeO}_2$ .<sup>71</sup> At temperatures high enough (but lower than the SiGe melting point),  $\text{GeO}_2$  is constantly reduced by a steady supply of Si from the SiGe alloy, providing  $\text{SiO}_2$  and elemental Ge ( $\text{GeO}_2 + \text{Si} \rightarrow \text{SiO}_2 + \text{Ge}$ ).<sup>72</sup> The expelled Ge piles up at the oxidation front. As time progresses during the oxidation process, the expelled Ge diffuses into the underlying SiGe, thereby increasing the Ge content of the layer, as illustrated in Fig. 1.19(b). If oxidation is continued until all Si atoms in the SiGe layer are oxidized, an ultrathin GeOI substrate is obtained (Fig. 1.19(c)-(d)).

With respect to the Smart Cut<sup>TM</sup> approach, this technique has the advantage that only simple and conventional processes, like SiGe epitaxy and thermal oxidation, are used, and that single crystal of Ge with smooth Ge /  $\text{SiO}_2$  interfaces can be obtained on a wafer scale as well as locally, permitting the fabrication of hybrid GeOI p-MOSFETs and strained SOI n-MOSFETs on the same substrate. However, TDDs for such structures are suspected to be significant

( $\geq 10^7 \text{ cm}^{-2}$ ), proving that the buried oxide is not a completely *compliant layer* and that relaxation partially occurs via the nucleation of dislocations.<sup>73</sup> A solution to the suppression of threading dislocations, which has been so far proved for SiGe with [Ge] = 15 at %, could be the utilization of the Ge condensation technique in micro-sized *mesa structures*.<sup>74</sup> This would however impose restrictions to the size of the device active areas.

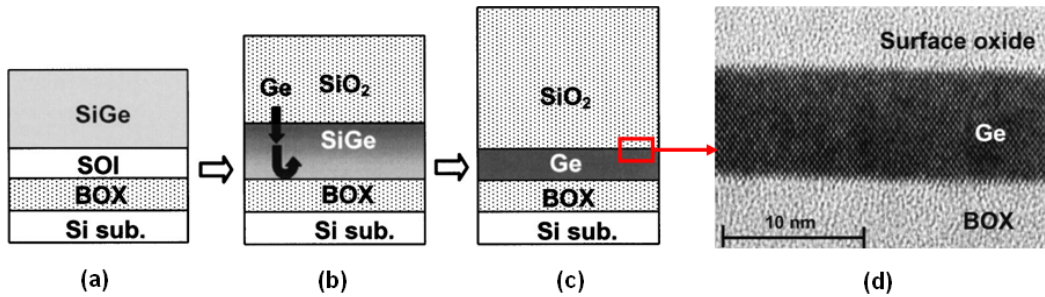


**Fig. 1.19:** GeOI fabrication process by the Ge condensation technique. (a) A SiGe layer is grown epitaxially on an SOI wafer; (b) SiGe is oxidized; (c) Ge is condensed completely; (d) cross-sectional TEM of a  $\sim 7\text{nm}$  Ge film obtained by Ge condensation.<sup>75</sup>

**Heteroepitaxial oxide buffers:** More recently, single crystalline dielectrics have been studied as potential epitaxial templates for Ge epitaxy. Oxide buffers indeed require a thickness only in the nm scale, making them much more suitable for integration with Si CMOS processes with respect, for instance, to  $\mu\text{m}$ -thick SiGe graded buffers. Examples are GeOI heterostructures realized on Si(001) by MBE, using SrHf<sub>x</sub>Ti<sub>1-x</sub>O<sub>3</sub> and SrHfO<sub>3</sub> perovskite oxides as insulating templates,<sup>76</sup> and on Si(111) by *solid-phase heteroepitaxy* (SPHE), adopting epitaxial (La<sub>x</sub>Y<sub>1-x</sub>)<sub>2</sub>O<sub>3</sub> buffers (see Fig. 1.20).<sup>77</sup>

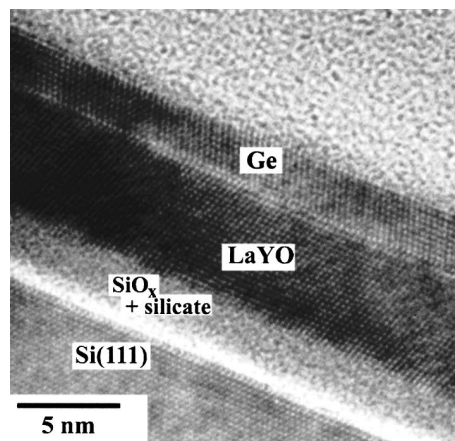


**Fig. 1.20:** TEM cross-section of an epitaxial Ge / LaYO / Si(111) substrate heterostructure. Note the deliberate formation of an amorphous silicon oxide layer at the Si / LaYO interface by exposure of the structure to an oxygen beam following growth.<sup>77</sup>

GeOI represents a potential substrate of choice for CMOS microelectronics beyond the 32 nm technology node, combining the superior mobility properties of Ge with the “*On Insulator*” advantages (e.g., less short channel effects, reduced junction capacitances and lower substrate coupling in radio frequency). Another prospective application of GeOI is given by GaAs-based HBTs. Indeed, InGaP / GaAs / Ge structures grown on Smart Cut™ GeOI show, performance being equal, lower self-heating effect than devices built up on GaAs and Ge substrates. This is owed to the better heat dissipation by the Si substrate ( $1.5 \text{ W}\cdot\text{cm}^{-1}\cdot\text{K}^{-1}$ ), despite the presence of the BOX between Ge and Si, than by the GaAs and Ge substrates ( $0.46$  and  $0.60 \text{ W}\cdot\text{cm}^{-1}\cdot\text{K}^{-1}$ , respectively).<sup>78</sup> Concerning optoelectronics, the insulated Ge layer in the GeOI system prevents the inter-diffusivity of Ge and Si as well as the collection of parasitic slow carriers generated in the Si substrate. High efficiency PIN photodiodes on GeOI were realized at high-speed operation at 850 nm wavelength up to 20 GHz bandwidth.<sup>79</sup> As another interesting outlook, GeOI wafers are envisaged as common platform for the integration of functional electronic devices / ICs and photovoltaic power generators.<sup>80</sup>

## 1.4 Aim of this thesis

Owing to the GeOI promising properties outlined above, it was decided to opt for the investigation of Ge thin films grown on ultra-thin single crystalline oxide buffer on Si wafers. The growth technique of choice was MBE, as it offers the chance for both global and local integration and it is ideal for “proof-of-principle” basic research studies.

In the coming pages, the growth by MBE of Ge thin films on single crystalline, cubic praseodymium (Pr) oxide on Si(111) substrates for engineered Si wafer applications is presented.

Chapter 2 motivates the choice of the buffer oxide and reports the up-to-date knowledge of the oxide properties.

Chapter 3 presents the experimental instrumentations utilized to deposit and characterize the GeOI heterostructures, with a brief discussion of the science basics of each employed technique.

Chapter 4 describes the initial growth stages of Ge thin layers on cubic Pr oxide by means of in-situ surface analysis techniques.

Chapter 5 reports about the structural, morphological and compositional properties of the GeOI heterostructure.

Chapter 6 deals with the characterization of the defect structure of the GeOI system.

Chapter 7 summarizes the results obtained during the PhD thesis on the Ge / cubic Pr oxide / Si(111) heterostructure and poses an outlook for future experiments and analyses.

## **2 Oxide heterostructures as buffers for the integration of alternative semiconductors on the Si platform**

### **2.1 The oxide buffer approach**

A more recent approach in the field of integration of alternative semiconductors on Si is the use of complex single crystalline oxide heterostructures grown on Si wafers.<sup>81</sup> As mentioned in the introduction, well ascertained and / or potential advantages of this technology are:

- the high flexibility of the oxide buffer in tailoring the epitaxial growth, i.e., solid solutions of isomorphic oxide structures can be employed and different oxide phases can be suitably selected (polymorphism);
- the insulating function of the dielectric buffer, of special importance in microelectronics for semiconductor-on insulator applications;
- the very thin thickness (in the nm range) required for the oxide template, functional for both the planar integration onto ICs and the conductance of heat during device operation;
- the role of compliance of the buffer, that is to say the capability of the buffer to elastically accommodate the misfit strain and absorb threading dislocations originated from the growth of the top semiconductor;<sup>82,83</sup>
- the role of barrier of the buffer against Si diffusion from the substrate into the active areas of the integrated semiconductor;
- the flexibility to integrate the alternative semiconductor onto the Si wafer either on a local or on a global scale.

## 2.2 Examples of single crystalline oxide buffers on Si(111)

Fig. 2.1 presents an overview of the oxide crystal structures reported to grow single crystalline on the Si diamond structure (Fig. 2.1(a)).

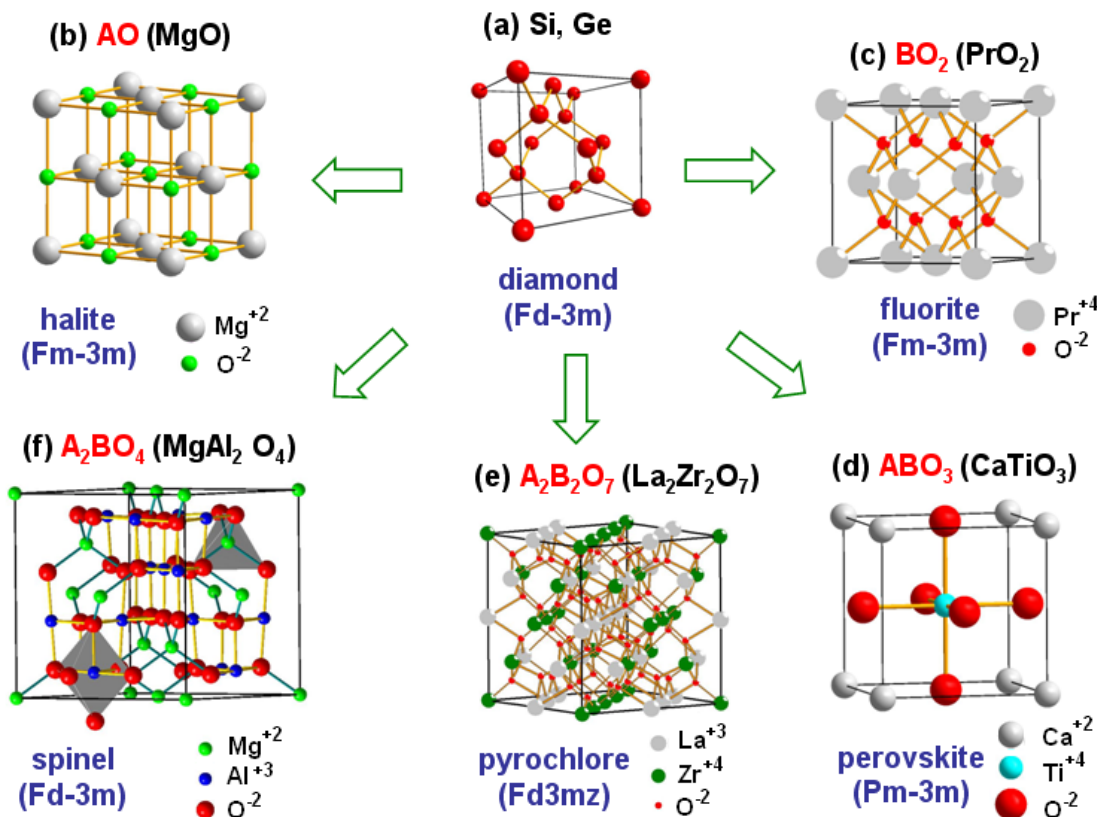
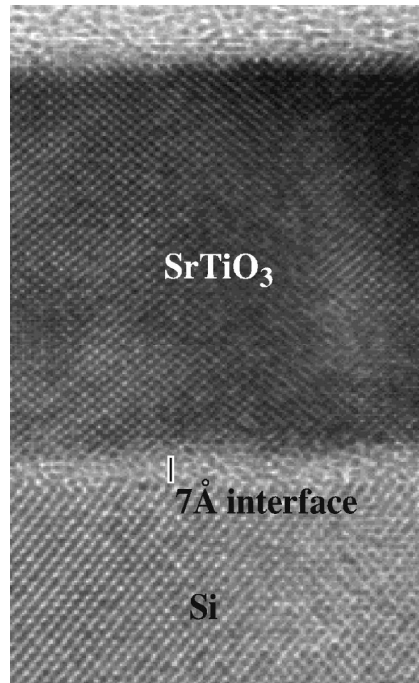


Fig. 2.1: Structural relationships of epitaxial oxides on Si.

A first class of epitaxial monocrystalline films on Si is provided by oxides of the AO type presenting the *halite* structure of NaCl (Fig. 2.1(b)), e.g.,  $\text{MgO}$ .<sup>84-87</sup> However, the prototype oxide structure with the greatest similarity to Si is the *fluorite* lattice ( $\text{CaF}_2$ ), that can be viewed as a  $\text{Ca}^{2+}$  *face centred cubic* (fcc) structure in which all tetrahedral voids are filled by  $\text{F}^-$  (Fig. 2.1(c)). Such a material has been widely investigated as buffer for the integration of functional semiconductors on Si, e.g., epi-Si, Ge and GaAs.<sup>88-98</sup> The  $\text{BO}_2$  crystal structure is found in the rare earth (RE) dioxides  $\text{REO}_2$ , e.g.,  $\text{CeO}_2$  (Refs. <sup>99,100</sup>) and  $\text{PrO}_2$  (Refs. <sup>101-103</sup>), whose thin films were proven to grow single crystalline on Si. It is noteworthy that RE oxides crystallize also in the form of sesquioxides  $\text{RE}_2\text{O}_3$  in the *bixbyite* structure. The bixbyite structure can be described as a vacancy-ordered fluorite with two oxygen vacancies per fluorite unit cell, causing the bixbyite unit cell parameter to be twice that of fluorite in all three dimensions.<sup>104</sup> Interestingly, the single crystalline growth of various bixbyite

oxides on Si was achieved in the past, e.g.,  $\text{Y}_2\text{O}_3$  (Refs. <sup>105-112</sup>),  $\text{Pr}_2\text{O}_3$  (Refs. <sup>113-122</sup>),  $\text{Er}_2\text{O}_3$  (Ref. <sup>123</sup>),  $\text{Sc}_2\text{O}_3$  (Refs. <sup>100,124</sup>), and  $\text{Gd}_2\text{O}_3$  (Refs. <sup>125-127</sup>). Adding the AO and  $\text{BO}_2$  formula units, the stoichiometry of the ternary  $\text{ABO}_3$  *perovskite* structure is obtained (Fig. 2.1(d)). Here, single crystalline  $\text{SrTiO}_3$  (Refs. <sup>128-130</sup>; see also Fig. 2.2),  $\text{SrHf}_x\text{Ti}_{x-1}\text{O}_3$  and  $\text{SrHfO}_3$  layers (Ref. <sup>76</sup>) on Si are intensively studied. Another class of ternary single crystalline oxide heterostructures on Si is given by the *pyrochlores*, e.g.,  $\text{La}_2\text{Zr}_2\text{O}_7$  (Ref. <sup>131</sup>), whose stoichiometry  $\text{A}_2\text{B}_2\text{O}_7$  results when the  $\text{A}_2\text{O}_3$  formula unit is added to two  $\text{BO}_2$  formula units (Fig. 2.1(e)). Finally, summing the  $\text{ABO}_2$  formula up with the  $\text{BO}_2$  one leads to the formation of the  $\text{AB}_2\text{O}_4$  *spinel* structure (Fig. 2.1(f)), which is found, for example, in  $\text{MgAl}_2\text{O}_4$ . Such an oxide grows single crystalline on Si, and, in turn, single crystalline epitaxial Si films of high quality can be grown on top, to realize SOI heterostructure.<sup>132,133</sup> Yet, it must be pointed out that the list of oxides which can be grown single crystalline on Si far exceeds the here presented examples, and that even other oxide crystal structure can be successfully integrated epitaxially on Si, despite their rather limited lattice relationship with Si, e.g.,  $\gamma\text{-Al}_2\text{O}_3$ .<sup>134-136</sup>



**Fig. 2.2: Example of single crystalline epitaxial oxide on Si: high resolution TEM image of epitaxial  $\text{SrTiO}_3$  on Si(001). An amorphous interface layer of about 7 Å is present between the two single crystal layers.<sup>129</sup>**

## 2.3 Oxide buffer flexibility: isomorphism and polymorphism

As mentioned at the beginning of the chapter, the principle advantage of oxide heterostructures as buffers is the high flexibility to tailor epitaxy parameters, i.e., the lattice constant, by exploiting isomorphism and polymorphism.

**Isomorphism:** Solid solutions of mixed isomorphic oxides can be easily formed, allowing for an extremely rich variety of lattice parameters in between the ones of the single oxides.  $\text{Pr}_2\text{O}_3$  and  $\text{Y}_2\text{O}_3$ , for example, both have the bixbyite structure and, being the former 2.7% bigger and the latter 2.4% smaller than twice the Si unit cell, can be mixed for the integration of lattice-matched as well as -mismatched SiGe systems. Fig. 2.3 shows the lattice window accessible by the  $(\text{Pr}_2\text{O}_3)_{1-x}(\text{Y}_2\text{O}_3)_x$  ( $x = 0-1$ ) mixed oxide buffer system. The red and green lines highlight two possible lattice-matched integrated systems, namely Si and  $\text{Si}_{0.2}\text{Ge}_{0.8}$  by adopting  $(\text{Pr}_2\text{O}_3)_{0.5}(\text{Y}_2\text{O}_3)_{0.5}$  and cub- $\text{Pr}_2\text{O}_3$  as buffers, respectively. Certainly, a huge variety of options exists to engineer the strain in the SiGe films via lattice-mismatched mixed oxide templates.<sup>81</sup>

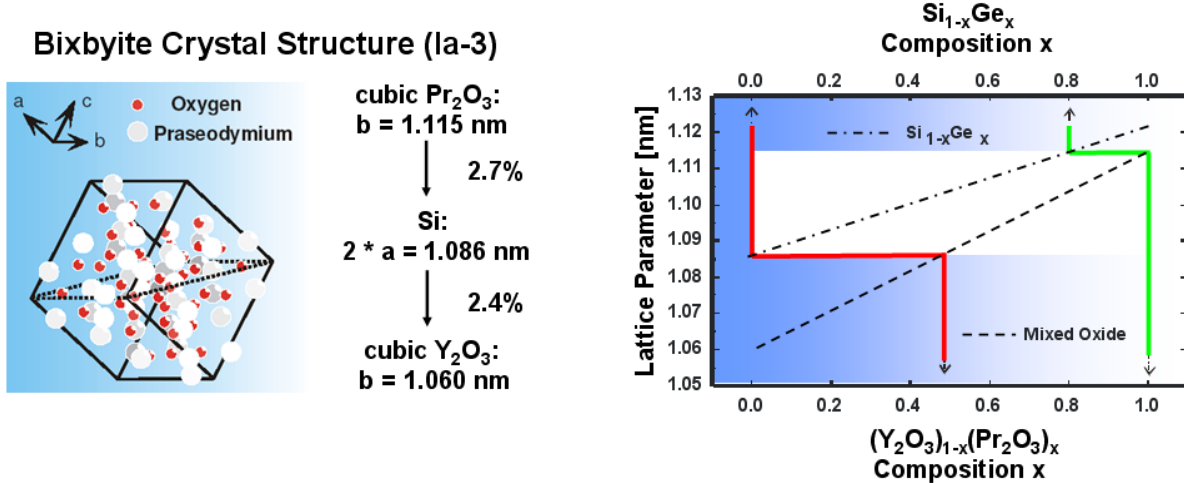
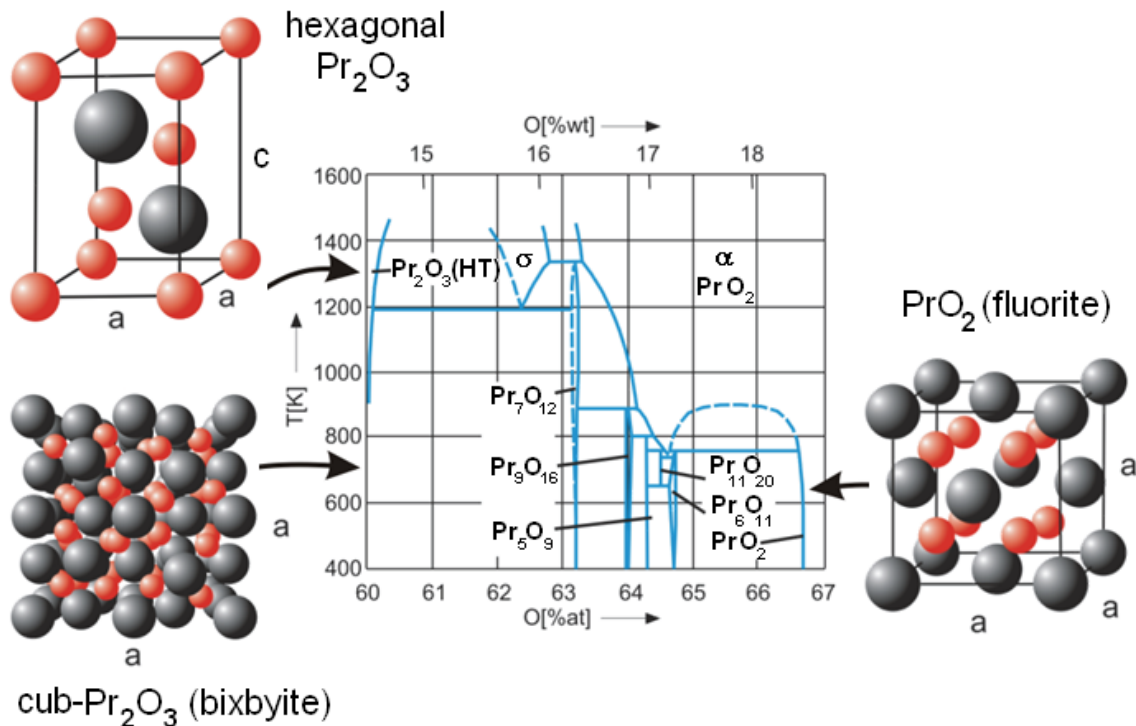


Fig. 2.3: (Left) atomic sketch of the bixbyite structure; (right) lattice window of the  $(\text{Pr}_2\text{O}_3)_{1-x}(\text{Y}_2\text{O}_3)_x$  ( $x = 0-1$ ) mixed oxide buffer for the integration of SiGe systems, e.g.,  $(\text{Pr}_2\text{O}_3)_{0.5}(\text{Y}_2\text{O}_3)_{0.5}$  for epi-Si (red line) and cubic  $\text{Pr}_2\text{O}_3$  for  $\text{Si}_{0.2}\text{Ge}_{0.8}$  (green line).

**Polymorphism:** Many complex oxide phase diagrams offer polymorphic structures for the same stoichiometric compound with different crystal lattice symmetries and parameters. One such example is  $\text{Pr}_2\text{O}_3$ , which exists in the *hexagonal* (hex, or *hcp* staying for *hexagonal close-packed*) as well as in the *cubic* (cub) phase, as can be seen from Fig. 2.4. Moreover, it is

noted that intermediate phases of non-stoichiometric oxide can exist, as between  $\text{Pr}_2\text{O}_3$  and  $\text{PrO}_2$ ,<sup>137-140</sup> and that, for a given phase, even the amount of oxygen vacancies in the oxide results in lattice parameter variations, as it was proven for instance in case of  $\text{PrO}_2$ .<sup>101</sup>



**Fig. 2.4: Complex Pr-O phase diagram and atomic sketches of the main Pr-O crystal structures, namely, hex- $\text{Pr}_2\text{O}_3$ , cub- $\text{Pr}_2\text{O}_3$ , and  $\text{PrO}_2$ .**

## 2.4 The choice of praseodymium oxide as buffer on Si(111)

Praseodymium oxide was chosen as template for the integration of Ge on Si(111) for the following reasons. First of all, its polymorphism was exploited. Films deposited on Si(111) by MBE from purified  $\text{Pr}_6\text{O}_{11}$  material grow in the hex- $\text{Pr}_2\text{O}_3$  phase with (0001)-orientation.<sup>115,116</sup> The formation of the sesquioxide is consistent with the oxygen deficient stoichiometry of the starting material and the absence of a reactive oxygen flux during growth. The preference of the high temperature hex- $\text{Pr}_2\text{O}_3$  phase with respect to the room temperature cub- $\text{Pr}_2\text{O}_3$  phase (Fig. 2.4) can be attributed to an epitaxial stabilization given by the far better lattice matching. Indeed, the epitaxial alignment of the close-packed Si(111) plane with the hex- $\text{Pr}_2\text{O}_3$  basal plane ( $d_{11-20}(\text{hex-}\text{Pr}_2\text{O}_3) = 0.192885 \text{ nm}$  and  $d_{220}(\text{Si}) = 0.191979 \text{ nm}$ ) leads to a linear misfit of only  $\sim + 0.5\%$ , in contrast to the larger in-plane mismatch of  $+ 2.7\%$  associated with the growth of the (111)-oriented cub- $\text{Pr}_2\text{O}_3$  phase. Thus,

both chemical and epitaxial considerations appear to favor the formation of the nearly lattice matched hex- $\text{Pr}_2\text{O}_3$  structure on Si(111).

**The stacking problem:** A fcc-related crystal structure, like the diamond one of Si and Ge, is also a closed-packed arrangement of atoms, like the hcp structure. Indeed, as can be seen from Fig. 2.5, the atoms on the (111) planes of the fcc structure are arranged in a hexagonal pattern just like the atoms on the (0001) planes of the hcp structure. The only difference stays in the way such hexagonal sheets of atoms sit on top of each other. Whereas in hcp structures the atoms in the second layer are above the hollows in the first layer and the atoms in the third layer are above the atoms in the first layer, so that the layer stacking sequence can be summarized as ABAB..., in fcc structures the first two atom layers are put down in the same way, but the atoms of the third layer are so placed in the hollows of the second layer that not until the fourth layer does a position repeat. The fcc stacking has therefore the sequence ABCABC...

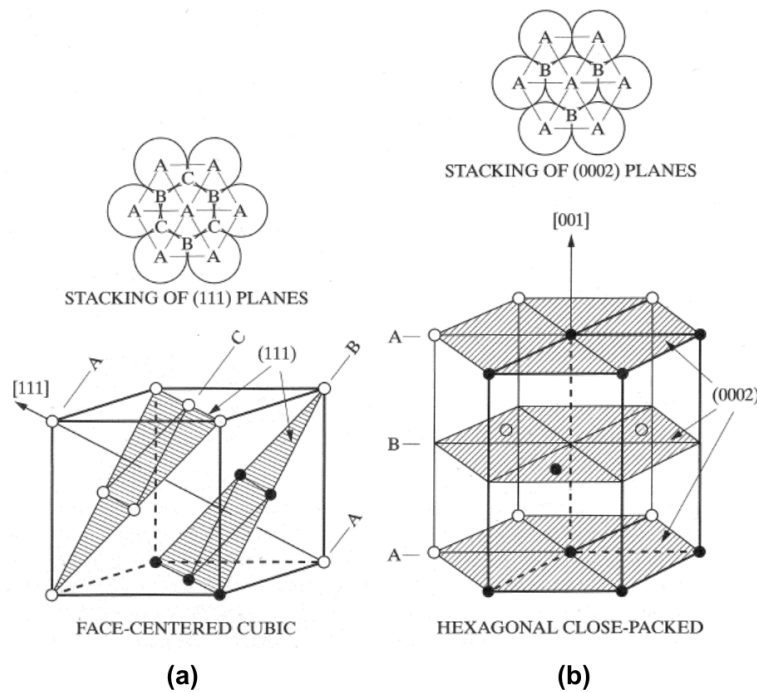


**Fig. 2.5: Comparison of the fcc (a) and hcp (b) structures, showing the ABCABC...stacking of the (111) planes in the former, and the ABAB...stacking sequence along [001] in the latter.<sup>141</sup>**

If the hex- $\text{Pr}_2\text{O}_3$  buffer were used for the integration of Ge on Si(111), the following problem would occur. The ABCABC... stacking information from the fcc Si(111) substrate (Fig. 2.6(a)) would be suppressed by the ABAB... stacking sequence of the (0001)-oriented hexagonal template (Fig. 2.6(b)) and, hence, would not be transferred in a unambiguous way

to the fcc Ge(111) epilayer (Fig. 2.6(c)). In fact, the Ge(111) film would grow with two equivalently possible stacking configuration of the (111) planes: half of the Ge matrix would have the stacking vector  $1/6<11-2>$  (bold red arrows in Fig. 2.6) oriented like in the Si(111) substrate and half of the Ge matrix would have the stacking vector rotated by  $180^\circ$  around the Si[111] surface normal with respect to the Si(111) substrate. A grain growing according to the latter configuration is called a *rotational twin*.<sup>141</sup> An example of 50%-twinned film is given by epi-Si(111) grown by MBE on hex-Pr<sub>2</sub>O<sub>3</sub>(0001) / Si(111)-substrate heterostructures, of which TEM photos are shown in Fig. 2.7.<sup>142</sup> It is noted that an analogous result was achieved for the same heterostack in case of *pulsed layer deposition* (PLD).<sup>113</sup>

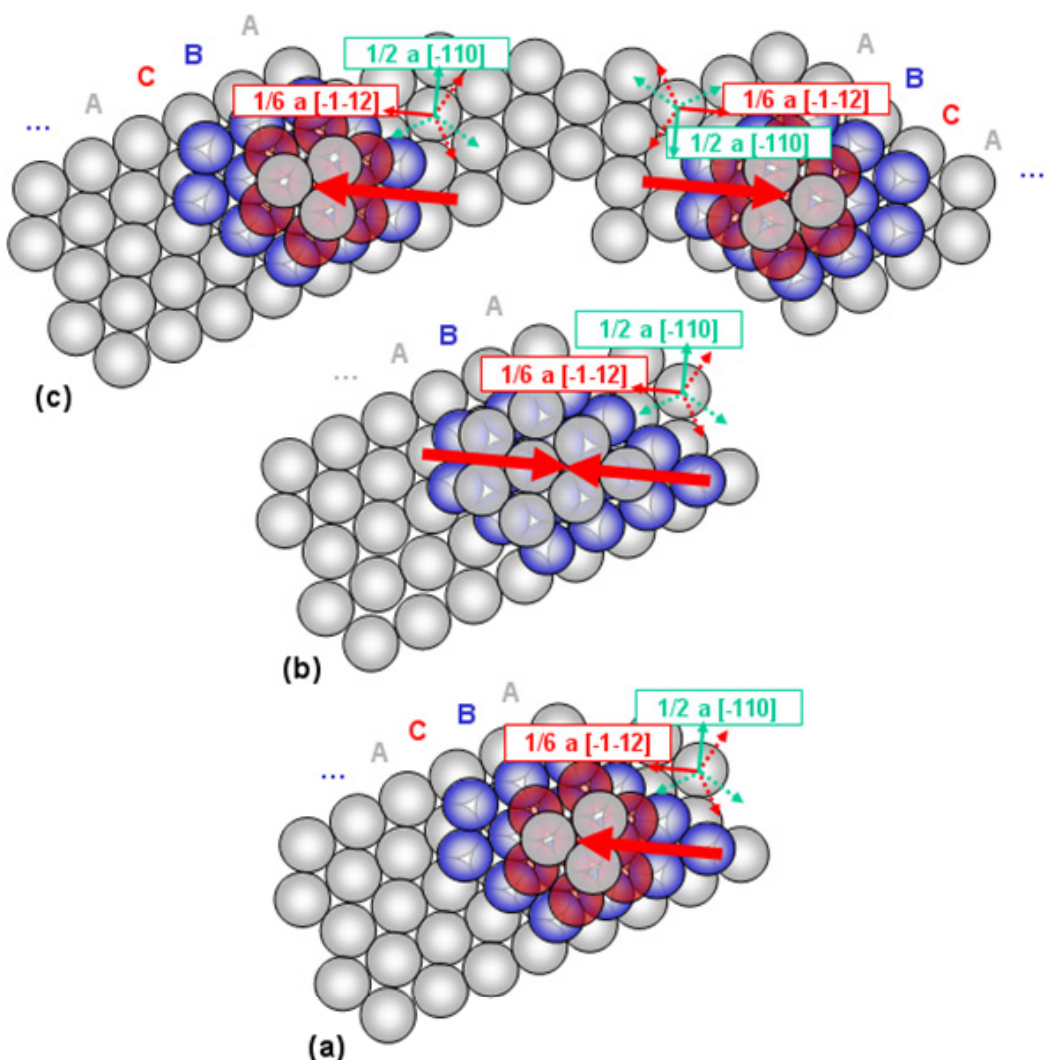


**Fig. 2.6:** Closed-packed sphere model illustrating (a) the ABCABC... stacking of the (111) planes in a fcc structure; the ABAB...stacking of the (0001) planes in a hcp lattice; the two possible stacking configurations of the (111) planes in a fcc lattice grown on top of a hcp template. On the left a grain with the stacking vector oriented like in (a); on the right a grain with the stacking vector rotated by  $180^\circ$  around [111] with respect to (a).

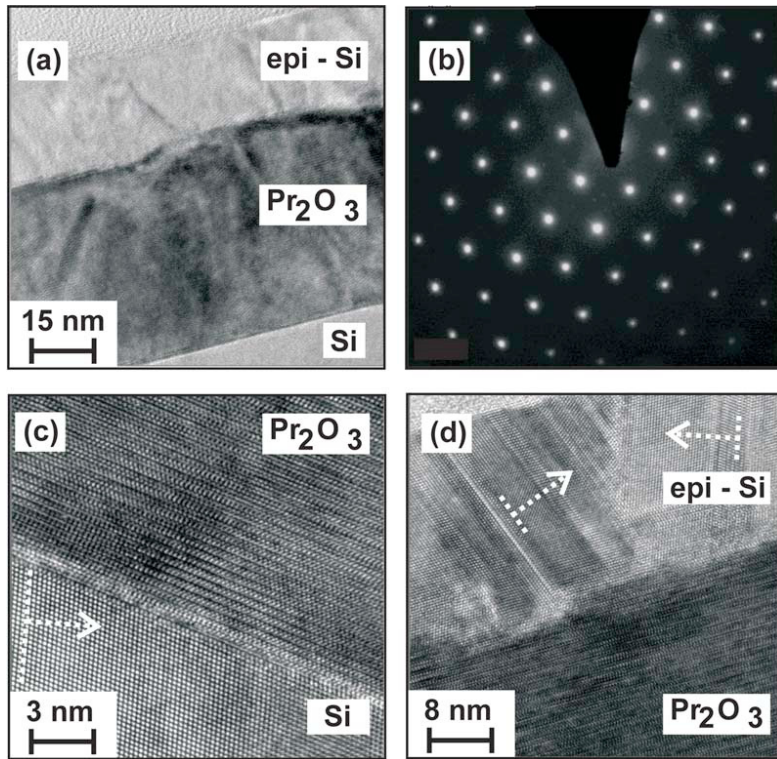


**Fig. 2.7: TEM Study of a MBE epi-Si(111) / hex- $\text{Pr}_2\text{O}_3$ (0001) / Si(111)-substrate heterostructure.** (a) Overview cross-section; (b) electron-diffraction pattern on a plane-view sample mounted with the incident electron beam parallel to Si[111]. The exhibited hexagonal symmetry can be understood as a (1x1) superstructure created by the superposition of the spots from the 0001 pole of the hex- $\text{Pr}_2\text{O}_3$  layer to those of the 111 pole of the Si substrate; (c) hex- $\text{Pr}_2\text{O}_3$ (0001) / Si(111)-substrate interface; epi-Si(111) / hex- $\text{Pr}_2\text{O}_3$ (0001) boundary, showing rotational twins in the epi-Si top layer.<sup>142</sup>

At this point, it is worthwhile to introduce the nomenclature usually employed for (111)-oriented epitaxial growth of fcc heterostructures. The epitaxial relation in which crystallographic orientation of the grown film and the substrate are the same is referred to as *type-A*, whereas *type-B* denotes the case in which the (111) plane stacking of the growing film is rotated by 180° around the (111) surface normal with respect to the substrate, that is to say, the rotational twin. If the lattice in Fig. 2.6(a) is thought of as the substrate, then, in the just given notation, the lattice on the left of Fig. 2.6(c) can be defined as type-A, whereas the one on the right of Fig. 2.6(c) as type-B. Fig. 2.8 exemplifies these definitions in case of the  $\text{CaF}_2$  / Si(111) system, for which such a nomenclature was coined. Fig. 2.8(a) sketches type-A oriented  $\text{CaF}_2$ , which is reported to grow on Si(111) above 400°C, whereas Fig. 2.8(b) depicts the type-B growth occurring below such temperature.<sup>88,143</sup> It is noted that the type-A orientation is preferable to the type-B one, as the latter introduces defects in the epitaxial film at steps on the substrate (Fig. 2.8(b)). Coexistence of both epitaxial relationships in the

epitaxial film often occurs and is undesired.<sup>144</sup> Indeed such a layer is bi-crystalline and defects decorate the boundaries between the twins.

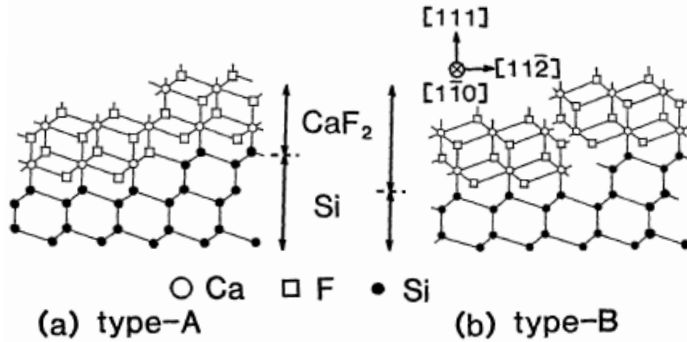


**Fig. 2.8:** Atomic arrangements of (a) type-A and (b) type-B at  $\text{CaF}_2$  /  $\text{Si}(111)$  interface.<sup>88</sup>

**The solution to the stacking problem:** The formation of rotational twins can be inhibited by using a suitable fcc buffer, which preserves the ABCABC... stacking input from the  $\text{Si}(111)$  substrate. This was demonstrated for epi-Si grown on a  $\text{Si}(111)$  wafer via either a  $\text{Y}_2\text{O}_3(111)$  / cub- $\text{Pr}_2\text{O}_3(111)$  bi-layer buffer (Ref. <sup>145</sup>) or a single  $\text{Y}_2\text{O}_3(111)$  template (Ref. <sup>112</sup>) (Figs. 2.9(a) and 2.9(b), respectively). In both systems, which employ fcc-related oxides, it was proven by X-ray diffraction experiments that the fraction of epi-Si matrix affected by twins is less than 1% (compared to the type-B-to-type-A ratio of 1 for growth on hex- $\text{Pr}_2\text{O}_3(0001)$  /  $\text{Si}(111)$  heterostructures).

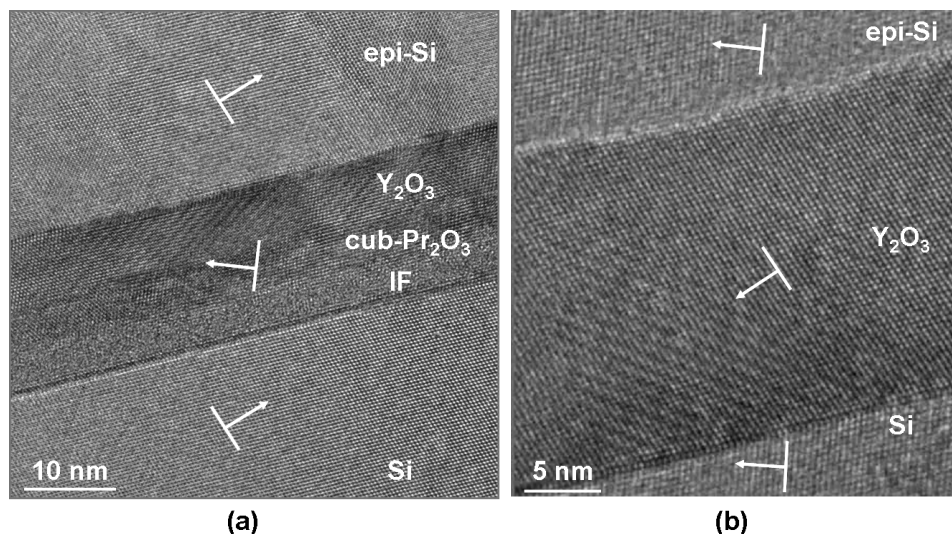


**Fig. 2.9:** TEM cross-section along  $<1-10>$  of (a) an epi-Si(111) / cub- $\text{Pr}_2\text{O}_3(111)$  /  $\text{Y}_2\text{O}_3(111)$  /  $\text{Si}(111)$  substrate heterostructure. *IF* denotes an interfacial layer;<sup>145</sup> (b) an epi-Si(111) /  $\text{Y}_2\text{O}_3(111)$  /  $\text{Si}(111)$  substrate system.<sup>112</sup> Arrows indicate normal directions to  $\{11-1\}$  planes in the different layers.

In the case of Ge integration on Si via praseodymium oxide, a requirement to avoid the formation of rotation twins is therefore the conversion of the buffer from the as-deposited hexagonal phase into the cubic one. Such a phase transformation can be realized by annealing the as-grown film at 600°C in 1 bar N<sub>2</sub> (Ref. 28) or in 10<sup>-5</sup> mbar O<sub>2</sub> (Ref. <sup>119</sup>). The annealed layer is a single crystalline, (111)-oriented cub-Pr<sub>2</sub>O<sub>3</sub> film with an exclusive type-B stacking. The 180° rotation of the cubic oxide lattice with respect to the Si substrate results from a stacking fault<sup>141,146</sup> at the oxide / substrate boundary and is attributable to electrostatic interaction effects across the ionic oxide / covalent Si interface, as addressed by theoretical *ab initio* calculations.<sup>145</sup> Interestingly, a TEM cross-section investigation shows that the phase transition is accompanied by an interface reaction at the oxide / Si(111) boundary, namely, the formation of an amorphous Pr silicate interface, which is absent in the as-grown hex-Pr<sub>2</sub>O<sub>3</sub> (compare Fig. 2.9(a) and Fig. 2.7(c)). The mechanism of the phase transformation, including the formation of the interfacial layer, is not fully understood so far and currently subject of investigation by Weisemöller et al.<sup>101,102,147,148</sup>

**The “antiphase boundary” problem:** There is a disadvantage in using a bixbyite oxide, like cub-Pr<sub>2</sub>O<sub>3</sub>, as buffer on Si(111). Due to the presence of ordered oxygen vacancies and the (4x4) coincidence lattice of cub-Pr<sub>2</sub>O<sub>3</sub>(111) on Si(111), *antiphase boundaries* (APBs) may form. These are planar lattice defects frequently observed in ionic crystals, which may concern both the *cation* and / or the *anion sub-lattices*. For instance, *cation anti-phase boundaries* (CAPBs) have been detected in Fe<sub>3</sub>O<sub>4</sub> single crystalline films grown on MgO substrates.<sup>149</sup> Both Fe<sub>3</sub>O<sub>4</sub> and MgO crystallize with the O atoms in an approximately fcc lattice and similar anion *d-spacings* (mismatch ~ 0.3%). However, the Fe<sub>3</sub>O<sub>4</sub> unit cell (*lattice parameter*  $a = 0.83967$  nm) is nearly twice the size of the MgO unit cell ( $a = 0.4213$  nm), owing to the more complicated cation arrangement in the former. Consequently, the first sublayer of Fe<sub>3</sub>O<sub>4</sub> islands which nucleate epitaxially on MgO can coalesce with improper stacking in the cation lattice, as illustrated in Fig. 2.10. Analogously, APBs can occur with regard to the anion sub-lattice, as in the case of epitaxial Sc<sub>2</sub>O<sub>3</sub> films grown on Si(111).<sup>100</sup> Sc<sub>2</sub>O<sub>3</sub> has the cubic bixbyite structure and its lattice mismatch with Si is ~ 10% ( $a(\text{Sc}_2\text{O}_3) = 0.9845$  nm and  $a(\text{Si}) = 0.5431$  nm). Since the bixbyite unit cell parameter is twice that of Si, when Sc<sub>2</sub>O<sub>3</sub> islands nucleate on Si, they have inherently no unique or energetically preferred arrangement of the ordered oxygen vacancies relative to the Si surface. As islands coalesce, APBs form between islands that have their oxygen vacancy sub-lattices shifted relative to each other. Interestingly, the displacement vectors across these APBs are of type

$$m/4[1-10] + n/4[-101] + p/4[01-1]$$

where m, n, and p are integers between 0 and 3. Antiphase domains are hence transformed into each other by translational operations that are present in the parent Si structure, but are absent in the oxide crystal structures.

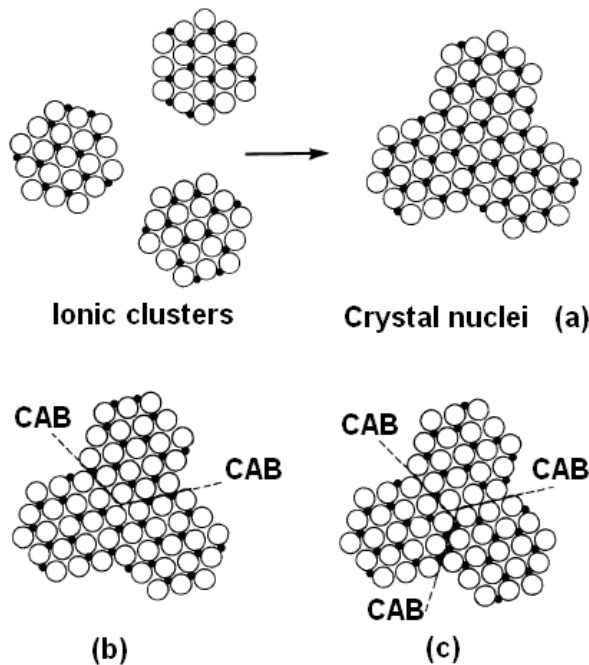


**Fig. 2.10: Schematic of nucleation process with or without the formation of CAPBs. (a) A nucleus with perfect cation arrangement; (b) and (c) nuclei containing incoherent cation arrangement. Open circle represent the closed packed anions, solid circles the cations.<sup>150</sup>**

The cub-Pr<sub>2</sub>O<sub>3</sub> buffer is ideal for the integration of Ge onto Si. Indeed, being its unit cell  $\sim 2.7\%$  bigger than two times the Si unit cell and  $\sim 1.4\%$  smaller than two times the Ge unit cell, it reduces the lattice mismatch of  $\sim +4.2\%$  between Ge and Si. Yet, as described above, APBs are expected to generate when cub-Pr<sub>2</sub>O<sub>3</sub> is grown on Si(111), due to the (2x2) coincidence lattice of the oxide on the substrate (Fig. 2.11(a)). These defects could be replicated in the over-growing Ge layer and must therefore be avoided.

**The solution to the “antiphase boundary” problem:** A way out is represented by the achievement of PrO<sub>2</sub>, in which APBs cannot form, because its fluorite lattice grows (1x1) on Si(111), as schematized in Fig. 2.11(b), and has all tetrahedral voids filled by oxygen. PrO<sub>2</sub>(111) films with exclusive type-B stacking are obtainable by post-deposition annealing of the as-deposited hex-Pr<sub>2</sub>O<sub>3</sub>(0001) / Si(111) systems in 1 bar O<sub>2</sub> at temperatures ranging from 400°C to 600°C.<sup>101,102,147</sup> The drawback is that PrO<sub>2</sub> has a lattice constant of 0.53920 nm,

which is very close to the one of Si ( $\sim -0.7\%$ ), but also  $\sim 4.7\%$  smaller than the one of Ge, hence increasing the lattice mismatch between Si and Ge. However, as described in chapter 4 of this thesis, the APB-free  $\text{PrO}_2(111)$  buffer is thermodynamically unstable in contact with Ge and gets chemically reduced to cub- $\text{Pr}_2\text{O}_3(111)$  in the early stages of Ge deposition, providing a lattice-matched buffer unaffected by APBs for the integration of Ge on the Si(111) platform.

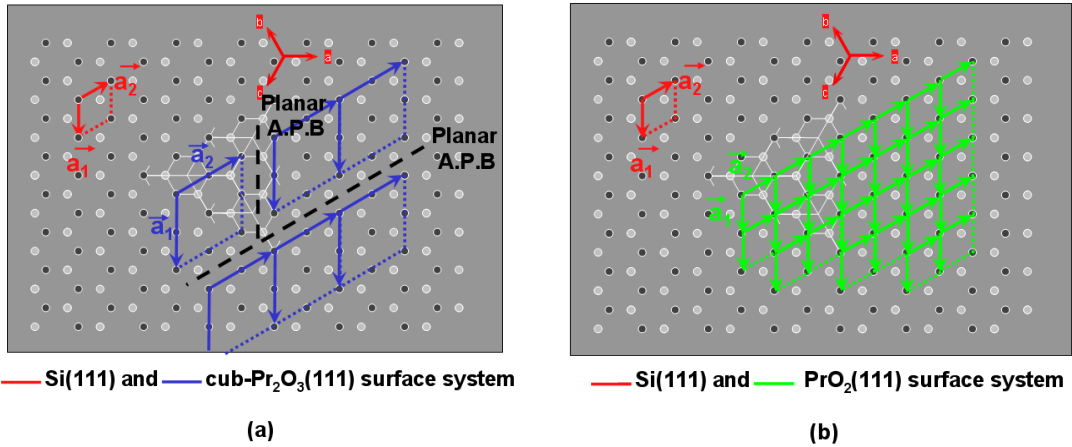


**Fig. 2.11:** Si(111) surface and related surface coordinate system (red) and (a) cub- $\text{Pr}_2\text{O}_3$  ( $2\times 2$ ) coincidence lattice, causing APB formation; (b)  $\text{PrO}_2$  ( $1\times 1$ ) coincidence lattice, without APB formation.

## 2.5 The heteroepitaxial over-growth of the buffer oxide

The *vision* is to create a Ge epilayer free of defects on the buffer oxide. Yet, in reality three main critical issues are to be faced, as sketched in Fig. 2.12:

- 1) Thermal and lattice mismatch between film and support system may generate a high number of structural defects in the growing overlayer, making it unsuitable for any device application (Fig. 2.12(a));
  - 2) The film does not always grow on the support system in a layer-by-layer (2D or Frank-van der Merwe) fashion. Due to lattice and surface energy considerations, either Stranski-Krastanow or Volmer-Weber growth often occur. In the former case, the layer wets the substrate and grows in a 2D way up to a certain *critical thickness*, beyond which islands form. In the latter mode, instead, islands form at the very beginning of the deposition (Fig. 2.12(b)). Of course, a non-2D growth results, after island coalescence, in very defective and rough films (for more details about growth modes Ref. <sup>151</sup> can be consulted).

3) The as-grown heterostructure has typically to undergo high temperature post-deposition thermal budget during device processing / operation. In case of thermodynamical instability of the heterostructure, unwanted phenomena, like layer inter-diffusion and surface morphology deterioration (Fig. 2.12(c)), could take place and mine the functioning of the device.

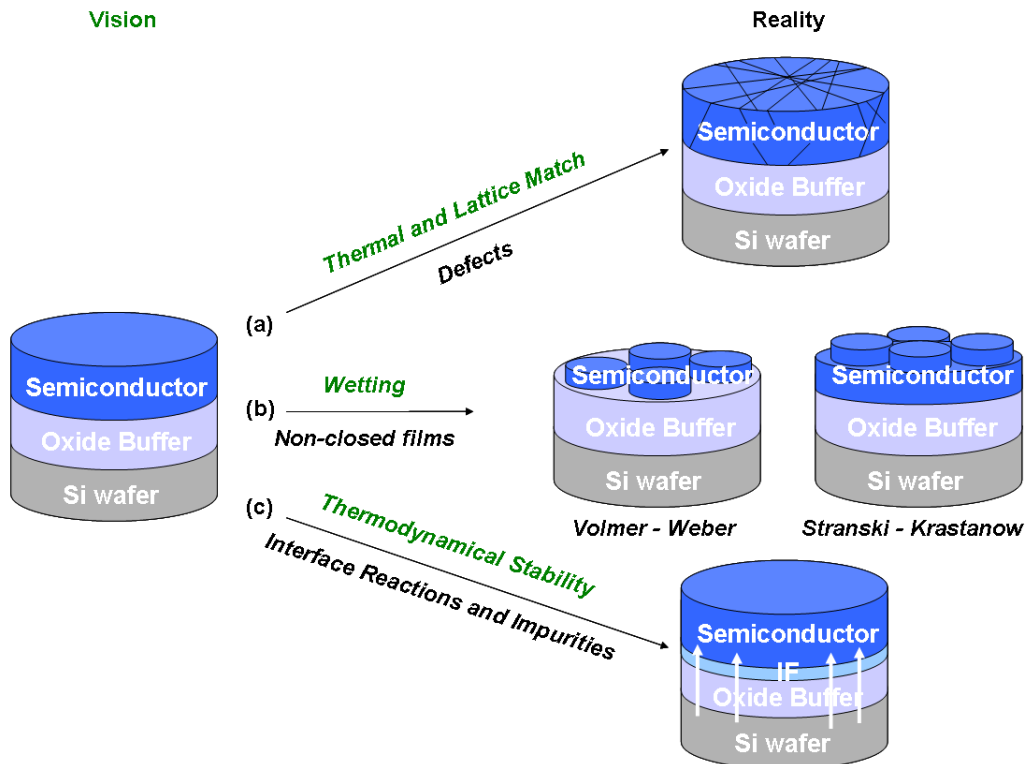


**Fig. 2.12:** (Left) Ideal engineered wafer; (right) issues to be faced during heteroepitaxial growth. Text in green describes the “vision”, text in black the “reality”. “IF” denotes an interfacial layer.

These three points will be dealt with in the coming chapters. In particular, the growth mode of the Ge deposit on the buffer oxide is illustrated in chapter 4. The issue of thermodynamical stability of the heterostructure is discussed in chapter 5, whereas an extended analysis of the Ge epilayer defect structure is presented in chapter 6.

### 3 Experimental background

The chapter consists of two main sections. The first one deals with methods and procedures employed to grow the Ge(111) / cub-Pr<sub>2</sub>O<sub>3</sub>(111) / Si(111) heterostructures; the second part describes the techniques used to analyze the deposited samples, and is in turn divided into two sub-sections, principal (x-ray diffraction and reflectivity) and additional (reflection high energy electron diffraction, photoelectron spectroscopy, secondary ion mass spectroscopy, scanning electron microscopy, and transmission electron microscopy) characterization techniques.

#### 3.1 Sample growth

##### 3.1.1 Substrate

4 in., boron-doped, on-oriented ( $\pm 0.4^\circ$ ) Si(111) wafers with resistivity in the range 5-15  $\Omega\cdot\text{cm}$  and thickness 525  $\mu\text{m}$  were used as substrates (supplier: Siltronic AG). Prior to Pr oxide deposition, wafers were cleaned according to the following procedure:<sup>152</sup>

- 1) 10 min rinse in de-ionized water.
- 2) 10 min *Piranha etch*, that is to say a mixture of 95-97%-concentrated sulphuric acid (H<sub>2</sub>SO<sub>4</sub>) and 30% hydrogen peroxide (H<sub>2</sub>O<sub>2</sub>) with a volume ratio of 4:1. Being the mixing process exothermic, the temperature of the solution is about 80°C. H<sub>2</sub>SO<sub>4</sub> is used to convert the organic contaminants on the wafer surface to carbon. Carbon reacts with the atomic oxygen present, owing to the dissociation of H<sub>2</sub>O<sub>2</sub>, to form CO<sub>2</sub>, a gas phase product which readily escapes the process tank. Piranha etch chemistry is highly effective at removing organic contaminants; however, it does not remove inorganic contaminants such as metals.
- 3) 1 min rinse in de-ionized water, in order to remove from the wafer surface the very viscous liquid remained after the Piranha solution.
- 4) 1 min *HF-last*, that is to say 50% fluoridric acid (HF) in de-ionized water with a volume ratio of 1:20, aiming at etching the silicon oxide on the wafer surface, which remains H-passivated.

- 5) 10 min rinse in de-ionized water.
- 6) 30 min 40% ammonium fluoride ( $\text{NH}_4\text{F}$ ), in order to further reduce surface roughness, resulting in a very smooth H-terminated Si(111) surface.
- 7) 5 min rinse in de-ionized water.

### 3.1.2 Molecular Beam Epitaxy

Molecular beam epitaxy (MBE) is a material deposition technique capable of reproducibly yielding films with impurity levels below ten parts per billion, with extremely precise control over composition and doping. Nowadays, MBE is employed to grow group IV, III-V and II-VI semiconductors, metals, magnetic materials, nitrides, oxides and fluorides by means of solid, gaseous as well as metal-organic sources. Although CVD is the deposition technique of choice in microelectronics, as it allows for mass production, MBE continues to be a reference tool to carry out proof-of-principle studies. Its success derives from its simplicity and versatility: in *ultra high vacuum* (UHV), beams of atoms or molecules are directed onto a heated crystal substrate, at whose surface they interact and form an ordered overlayer (epitaxy); monitoring techniques, like reflection high energy electron diffraction (RHEED), are made possible by the UHV environment and can be utilized to follow in-situ the film deposition. Fig. 3.1 shows a schematic of a typical MBE apparatus.

The MBE system used in this thesis is a *DCA 600* (Fig. 3.2) and handles 4 in. wafers. It consists of a load-lock, where the samples are pumped down by a membrane pump to the  $10^{-6}$  mbar range and degassed at  $\sim 200^\circ\text{C}$  for 20 min before being introduced into the UHV environment, a buffer line for wafer transfer, and three growth chambers, one for oxides, one for Si-Ge and one for III-V materials. The reason why more chambers were installed is to avoid cross contamination, i.e., metal impurities from metal oxide materials into Si-Ge films. Stoichiometric  $\text{Pr}_6\text{O}_{11}$  and Ge powder material are evaporated from pyrolytic graphite crucibles (covered with Si as shielding liner) by electron beam evaporators, whose principle of functioning is shown in Fig. 3.3. The flux of the sublimated atoms or molecules determines the number of atoms or molecules per time that arrive onto the sample surface and is therefore a key growth parameter, together with the substrate temperature that influences the kinetics of the impacted particles. Base pressure is  $\sim 10^{-10}$  mbar, and pressure during oxide and Ge deposition is in the  $10^{-6}\text{-}10^{-7}$  and  $10^{-8}\text{-}10^{-9}$  mbar range, respectively.

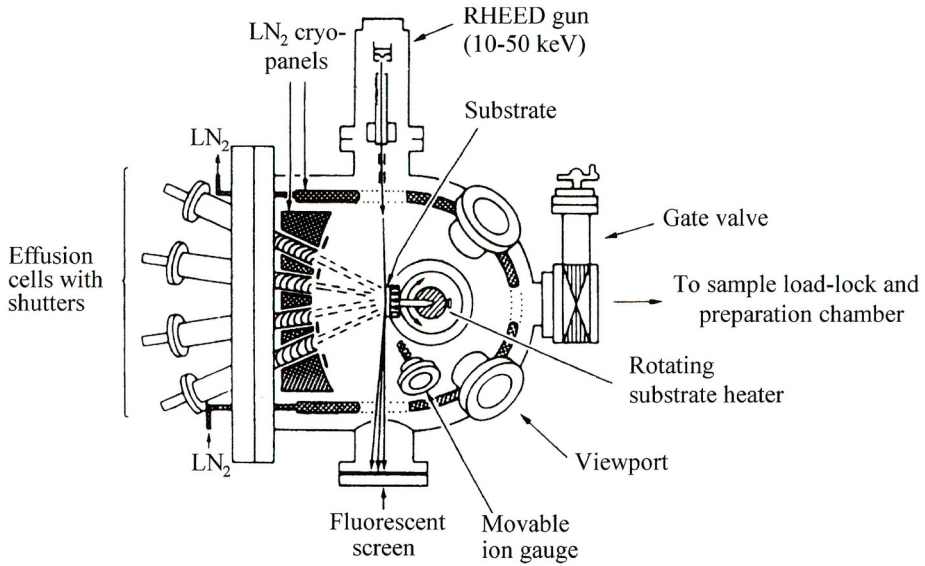


**Fig. 3.1: Basics of a MBE equipment.** The sample is introduced through the load-lock into the growth chamber, where it is placed on the holder and taken at the desired temperature (controlled by a thermocouple). Sample rotation assures uniform deposition over the entire surface. UHV is realized by means of rough / turbo pumps and liquid nitrogen cryopanels, which provide very large pumping speeds for condensable gases, particularly H<sub>2</sub>O and heavier hydrocarbons, and also, though less effectively, for CO<sub>2</sub>. Either effusion cells (sketched here) or electron beam evaporators are employed to evaporate the desired material from the crucible onto the substrate. Molecular and atomic beams can be switched on and off by shutters in front of the sources, which are actuated by computer-controlled motors. The film growth is monitored real-time by RHEED. Pressure is measured by means of an ion gauge.

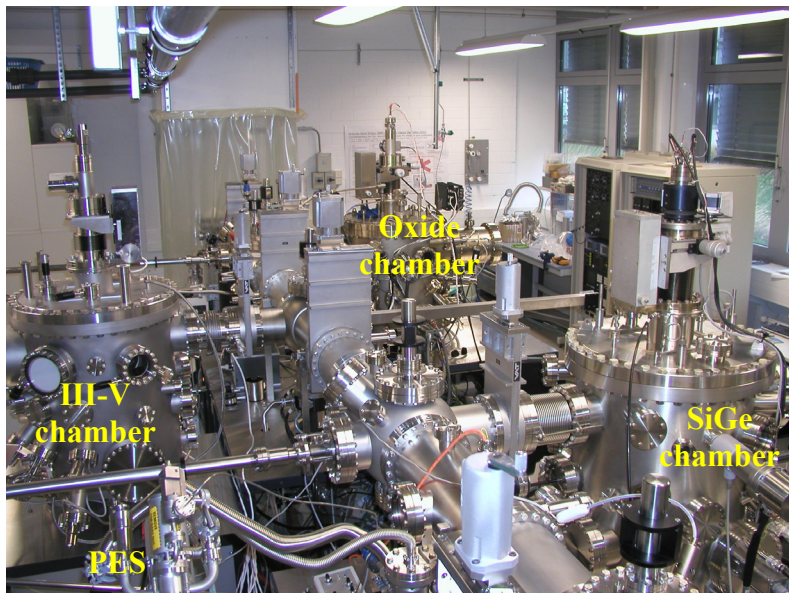


**Fig. 3.2: Photograph of the DCA 600 MBE apparatus.** Three growth chambers are visible: the oxide chamber on the bottom, the III-V compound semiconductor one on the left, and the Si-Ge chamber on the right. The PES instrument is also highlighted (see Fig. 3.23).

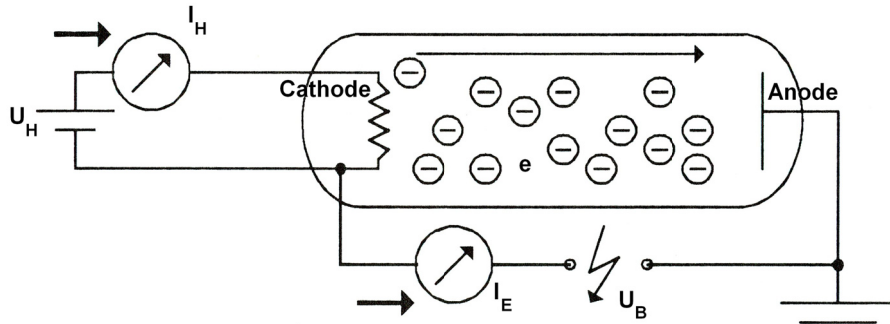


**Fig. 3.3:** Schematic of electron-beam generation in an electron-beam evaporator. The electron beam is created in an evacuated space by applying a potential difference  $U$  between a cathode, heated by passing through it a current with intensity  $I_H \sim 10$  A and voltage  $U_H \sim 10$  V, and an unheated anode. The electron beam or emission current  $I_E$  is measured with an ammeter located in the high-voltage lead.  $I_E$  in the range (64-90) mA was used throughout the experiments presented in this thesis. The electrons emerging from the cathode are made cross a cylinder (Wehnelt cylinder) having the same negative bias as the cathode, resulting in a focusing of the electron beam (not sketched). The focused electron beam is then accelerated by a voltage  $U_B = 10$  kV towards the source material to be evaporated. An electromagnetic field is applied to scan the beam over the crucible for homogenous heating. The kinetic energy of the impinging electrons causes the selected material to become heated to incandescence and sublime.

### 3.1.3 Preparation of the oxide buffer

Once transferred from the load-lock onto the sample holder of the dedicated oxide chamber, the Si(111) substrate was annealed in UHV at 700°C for 5 min to achieve the (7x7) surface reconstruction. It is noted that the deposition of the oxide must occur within a short time from the wafer wet cleaning procedure outlined above. Otherwise, a native silicon oxide layer will reform on the surface, mining the epitaxy of Pr<sub>2</sub>O<sub>3</sub>. As already described in detail in Ch. 2.4, the evaporation of highly purified Pr<sub>6</sub>O<sub>11</sub> material onto the Si(111) substrate, kept at a temperature of 625°C, leads to the formation of hex-Pr<sub>2</sub>O<sub>3</sub> with (0001) orientation. It is reminded that, though cub-Pr<sub>2</sub>O<sub>3</sub> is the thermodynamically predicted stable phase at such a temperature (see Fig. 2.4), hex-Pr<sub>2</sub>O<sub>3</sub> with a very sharp interface grows, owing to the better lattice match with the Si(111) substrate.<sup>116</sup> However, since a cubic buffer with (1x1) coincidence lattice on Si(111) is needed for the overgrowth of high quality Ge, the hex buffer was converted into PrO<sub>2</sub>(111) via an ex-situ annealing in 1 bar O<sub>2</sub> at 400°C for 30 min.<sup>101,102,147</sup> A conventional horizontal furnace (model PEO 601), capable of hosting up to 25 wafers with a diameter of 4 in., was used for the phase transformation. The sample was then re-introduced into the load-lock of the MBE system, where the atmospheric contamination

caused by the vacuum break was outgassed, and from there into UHV in the SiGe chamber for the following deposition of Ge.

### 3.1.4 Deposition of the Ge epilayer

Ge was evaporated on  $\text{PrO}_2$  in two steps, a first one at  $\sim 550^\circ\text{C}$  for 100 sec and a second one at  $\sim 300^\circ\text{C}$  with duration proportional to the targeted final thickness of the epilayer. A Volmer-Weber growth mode was observed and it is described in detail in Ch. 4. In the initial deposition stages, a high temperature of the substrate is needed so that the Ge islands grow single crystalline and type-A oriented. The Ge seeds were then overgrown at  $300^\circ\text{C}$ , allowing for a smoothening of the Ge growth front, as shown in Fig 3.4. Ge deposition rates in the range (0.01-0.15) nm / sec, corresponding to electron beam current intensities  $I_E$  in the range (64-90) mA (see Fig. 3.3), were tested, the lowest flux in the window of the accessible parameters providing the flattest Ge epifilms.

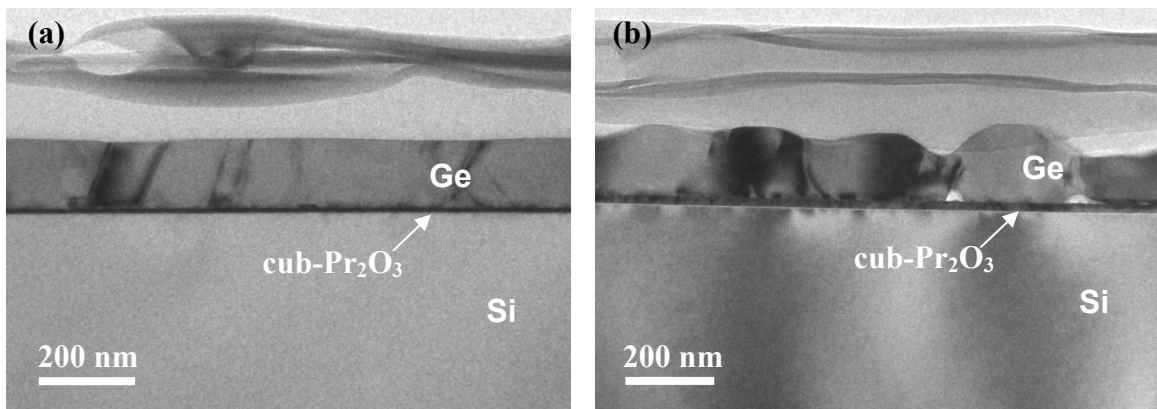


**Fig. 3.4:** TEM images of (a) a Ge layer deposited in the double step mode (first step at  $600^\circ\text{C}$ , second step at  $300^\circ\text{C}$ ); (b) a Ge film entirely grown at  $600^\circ\text{C}$ .

## 3.2 Sample characterization

### 3.2.1 Main methods

#### 3.2.1.1 X-ray Diffraction

**X-ray diffraction theory:** X-ray diffraction (XRD) is a non-destructive analytical technique, which reveals information about the crystallographic structure of materials. It is based on the elastic scattering of x-rays from the periodic electron density distribution of the sample under investigation, an effect named *Thomson scattering*. In this process, electrons oscillate like a Hertz dipole at the frequency of the incoming x-ray beam and become themselves source of electromagnetic dipole radiation. The wavelength  $\lambda$  of the x-rays is conserved for Thomson scattering, in contrast to inelastic scattering processes, e.g., Compton scattering. Owing to the similar scale of the x-ray wavelengths and the interatomic distances in crystals ( $\sim 0.15\text{-}0.4$  nm), constructive and destructive interference of the scattered beams occur when crystalline materials are exposed to x-rays under specific geometric conditions, giving rise to diffraction. In particular, it can be shown that the intensity of an unpolarized monochromatic x-ray beam, of intensity  $I_0$  and wavelength  $\lambda$ , scattered from a small crystal, having the shape of a parallelepiped with edges  $N_1\mathbf{a}_1$ ,  $N_2\mathbf{a}_2$ ,  $N_3\mathbf{a}_3$  parallel to the crystal axes  $\mathbf{a}_1$ ,  $\mathbf{a}_2$ , and  $\mathbf{a}_3$ , is (Ref. <sup>153</sup>)

$$I = I_e \cdot F^2 \cdot G^2 \quad (3.1)$$

where

$$I_e = I_0 \cdot \frac{e^4}{m^2 c^4 R^2} \cdot \left( \frac{1 + \cos^2 2\theta}{2} \right) \quad (3.2)$$

$$F = \sum_n f_n \cdot \exp \left[ i(\mathbf{K} - \mathbf{K}_0) \cdot \mathbf{r}_n \right] \quad (3.3)$$

$$G^2 = \frac{\sin^2 [(\mathbf{K} - \mathbf{K}_0) \cdot N_1 \mathbf{a}_1 / 2]}{\sin^2 [(\mathbf{K} - \mathbf{K}_0) \cdot \mathbf{a}_1 / 2]} \cdot \frac{\sin^2 [(\mathbf{K} - \mathbf{K}_0) \cdot N_2 \mathbf{a}_2 / 2]}{\sin^2 [(\mathbf{K} - \mathbf{K}_0) \cdot \mathbf{a}_2 / 2]} \cdot \frac{\sin^2 [(\mathbf{K} - \mathbf{K}_0) \cdot N_3 \mathbf{a}_3 / 2]}{\sin^2 [(\mathbf{K} - \mathbf{K}_0) \cdot \mathbf{a}_3 / 2]} \quad (3.4)$$

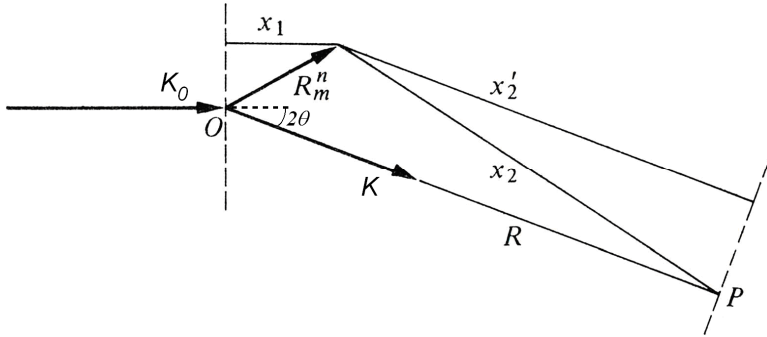


**Fig. 3.5: Diffraction of a parallel primary beam by a small crystal.** O denotes the crystal origin;  $\mathbf{R}_m^n = m_1 \mathbf{a}_1 + m_2 \mathbf{a}_2 + m_3 \mathbf{a}_3 + \mathbf{r}_n$  gives the position of the atom of type n in unit cell  $m_1m_2m_3$ ;  $\mathbf{K}_0$  indicates the incoming wave vector,  $\mathbf{K}$  the scattered wave vector detected by the observer in P at a distance  $R$  from the crystal;  $2\theta$  is the scattering angle. Relative to the distance from the x-ray source and the distance  $R$  from the point of observation, the crystal is small enough that both the primary and the scattered beam can be treated by the plane-wave approximation, due to which  $(x_1 + x'_2) \rightarrow (x_1 + x'_2)$  (Fig. adapted from Ref. <sup>153</sup>)

Eq. (3.2) is the x-ray intensity scattered from a single electron (*Thomson equation*), containing the electron charge  $e$  and mass  $m$ , the speed of light  $c$ , and the distance  $R$  of the observer from the origin  $O$  at which the small crystal is centered (Fig. 3.5), and the polarization factor  $(1+\cos^2 2\theta)/2$ . It is noteworthy that the ratio  $e^4/m^2c^4$  is  $\sim 10^{-26} \text{ cm}^2$ , so that the intensity of x-ray scattering from one electron tends to zero, and a x-ray signal is recorded only when the number of scattering objects is of the same order of magnitude as the *Loschmidt's number* ( $\sim 2.7 \cdot 10^{19} \text{ cm}^{-3}$ ) or, in case ultra-thin films and nanostructures are to be studied, only when high-brilliance synchrotron radiation sources are employed (see page 50). It also becomes evident from this equation why the scattering from atomic nuclei can be neglected. The mass of a nucleus is indeed at least 1836 times bigger than the electron mass, yielding a less than  $10^{-6}$  smaller intensity in the scattering process than an electron.

In eq. (3.3),  $F$  is the so-called *structure factor*.  $f_n$  is the atomic scattering factor for the atom  $n$ ;  $\mathbf{K}_0$  is the incident wave vector and  $\mathbf{K}$  the scattered wave vector detected by the observer at a distance  $R$  from the crystal; the  $\mathbf{r}_n$  vectors give the positions of the different atoms in the unit cell, and the summation over  $n$  varies from crystal structure to another. The structure factor plays a very important role in determining crystal structures, since it is the only term in which the atomic positions in the unit cell appear. Eq. (3.4) is the *lattice factor*, which includes the spatial dimensions of the unit cell. Constructive interference occurs only if the three quotients in eq. (3.4) are simultaneously close to their maximum values, conditions whose fulfilling leads to the formulation of the *Laue equations*, which are analogous to the Bragg law.

These formulas are valid in the approximation of the kinematical theory, which assumes that (a) multiple scattering processes do not take place; (b) absorption can be neglected; (c) refraction does not play a role in the intensity of the diffracted wave. This is true when imperfect crystals consisting of very small mosaic blocks are considered (otherwise, for the highly perfect type of crystal, it is necessary to use the more rigorous and complex principles of dynamical scattering<sup>153</sup>).

For details on the theory of x-ray diffraction, Refs. <sup>153</sup> and <sup>154</sup> can be consulted.

**Employed XRD tools and x-ray sources** XRD analyses were carried out with three XRD instruments, a Rigaku DMAX 1500 and a Rigaku SmartLab operated at the IHP laboratories, both equipped with a rotating anode emitting Cu K<sub>α</sub> radiation ( $\lambda = 0.154$  nm), (Figs. 3.11 and 3.12), and the diffractometer of the insertion device (ID) 32 beamline of the European Synchrotron Radiation Facility (ESRF) in Grenoble (France), using  $\lambda = 0.1169$  nm (Figs. 3.7-3.9). As an example of XRD hardware, optics and diffractometer setups of the synchrotron beamline are presented in detail below.

**The ESRF ID32 beamline** X-ray sources did not considerably improve from Coolidge's development of the x-ray tube in 1913 to the mid 1970s.<sup>155</sup> It was then realized that the synchrotron radiation emitted from charged particles circulating in storage rings constructed for high energy physics experiments was potentially a much more intense and versatile source of x-rays. To date, so called third generation synchrotron sources are in use, which are  $\sim 10^{12}$  times brighter than the early laboratory-based ones (Fig. 3.6). The high brilliance is a tremendously important parameter when analyzing thin films, as already mentioned at page 49 with regard to Eq. (3.1). Of course, high photon flux also permits for much faster measurements, compared to analyses run in a laboratory. The other big advantage provided by synchrotron radiation is given by the fact that the beam energy can be tuned according to the experimentalist's need.

The ID32 beamline of the ESRF was utilized to characterize the Ge(111) / cub-Pr<sub>2</sub>O<sub>3</sub>(111) / Si(111) heterostructure. A schematic setup of the beamline optics for diffraction experiments is illustrated in Fig. 3.7.

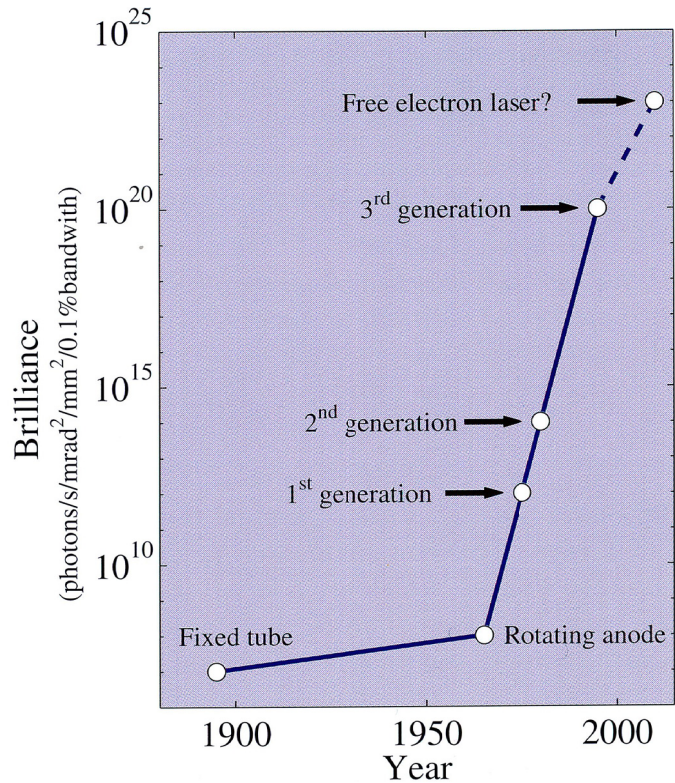


**Fig. 3.6: The brilliance of x-ray sources as a function of time.<sup>155</sup>**

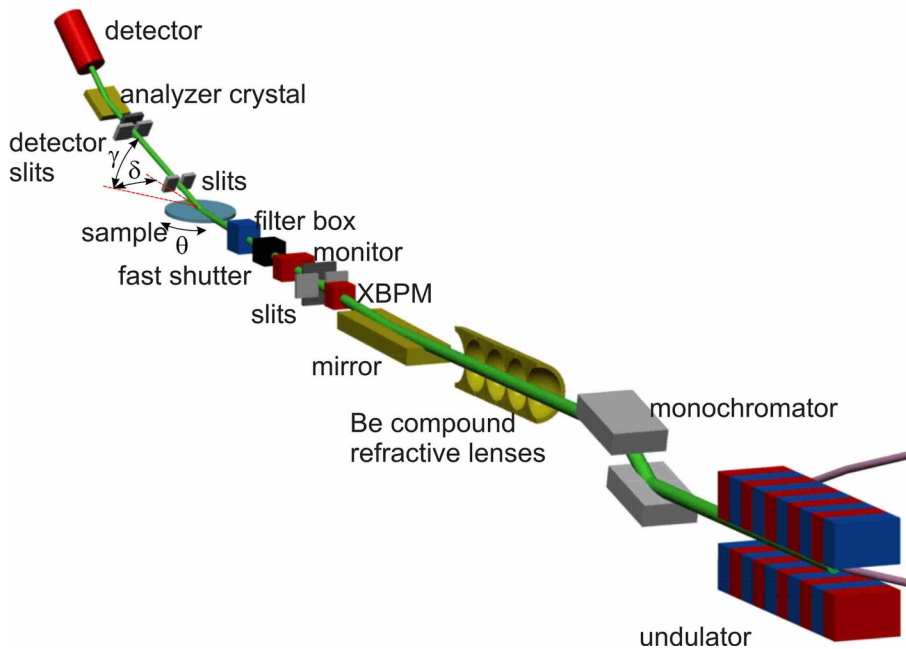


**Fig. 3.7: Optics setup used at ID32 for diffraction experiments.**

X-rays are produced by an *undulator*. Such a device is inserted in any of the straight sections, followed by circular arc segments, present in the storage ring. It consists of an array of magnets generating a field that alternates from up to down along the path of the electrons,

forcing them to execute oscillations in the horizontal plane as they traverse through the section (Figs. 3.7 and 3.8). The undulator is built so that the radiation of each emitting electron is coherent from period to period. In this way, the amplitudes of the radiated waves are first added, and then the sum is squared to obtain the resulting intensity.<sup>155</sup> The undulator radiation is first monochromatized by a pair of Si(111) crystals, kept at liquid nitrogen temperature due to the heat load of the white beam,<sup>156</sup> and then focused by up to fifteen bi-dimensional Be compound refractive lenses.

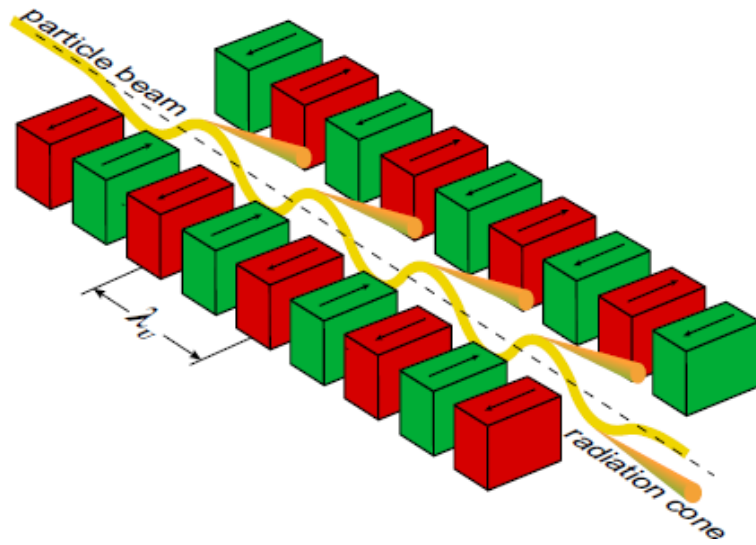


**Fig. 3.8: Schematic of an undulator. Periodically ordered magnets force the traversing electrons to oscillate and radiate.  $\lambda_u$  is the undulator spatial period.**

Next, the focused beam is reflected by a x-ray mirror, made of  $\text{SiO}_2$  or either Ni or Pd coated stripes depending on the beam energy, in order to suppress the higher order harmonics generated by the undulator and transmitted by the higher order reflections of the Si(111) double crystal monochromator. The final beam size, typically  $15 \text{ (vertical)} \cdot 500 \text{ (horizontal)} \mu\text{m}^2$ , is defined by an entrance slit 70 cm before the sample. An ionization chamber filled with argon is placed behind the slit for monitoring the incident beam intensity. In case of specimens for which radiation damage is expected to occur, a fast shutter can be activated to prevent the beam from impinging on the sample all the time when not needed, e.g., while adjusting the sample position. A filter box is also available to reduce the x-ray intensity during alignment procedures, avoiding saturation of the detector. The angle of incidence of the x-rays onto the specimen surface was varied between  $0.1^\circ$  and  $0.6^\circ$ , selecting in this way the information depth achievable during the analysis. In fact, at the employed beam energy of  $\sim 10.6 \text{ keV}$  ( $\lambda = 0.1169 \text{ nm}$ ), the critical angles  $\alpha_{\text{l},c}$  for total reflection from a Ge and a  $\text{Pr}_2\text{O}_3$  surface are  $0.23^\circ$  and  $0.26^\circ$ , respectively. The beam diffracted from the specimen passes

through a graphite analyzer crystal, reducing its divergence, and is finally collected by a NaI scintillator from *Cyberstar*. On the detector arm, a fixed aperture of  $6 \text{ (vertical)} \cdot 3 \text{ (horizontal)} \text{ mm}^2$  is placed to select the sample surface area contributing to the signal. A second aperture, typically  $3 \cdot 3$  or  $2 \cdot 2 \text{ mm}^2$  in size, is inserted  $\sim 95 \text{ cm}$  after the sample to define the in-plane and out-of-plane angular resolutions in the reciprocal space. Sample and detector movements are operated by means of a “3S+2D” diffractometer with “Huber tower” (Fig. 3.9): it consists of a three-circle goniometer for the sample-orienting degrees of freedom  $\theta$ ,  $\phi$  and  $\chi$  (3S), and an independent two-circle goniometer on the  $2\theta$  arm for the  $\delta$  and  $\gamma$  motions of detector and crystal analyzer (2D).<sup>6</sup>

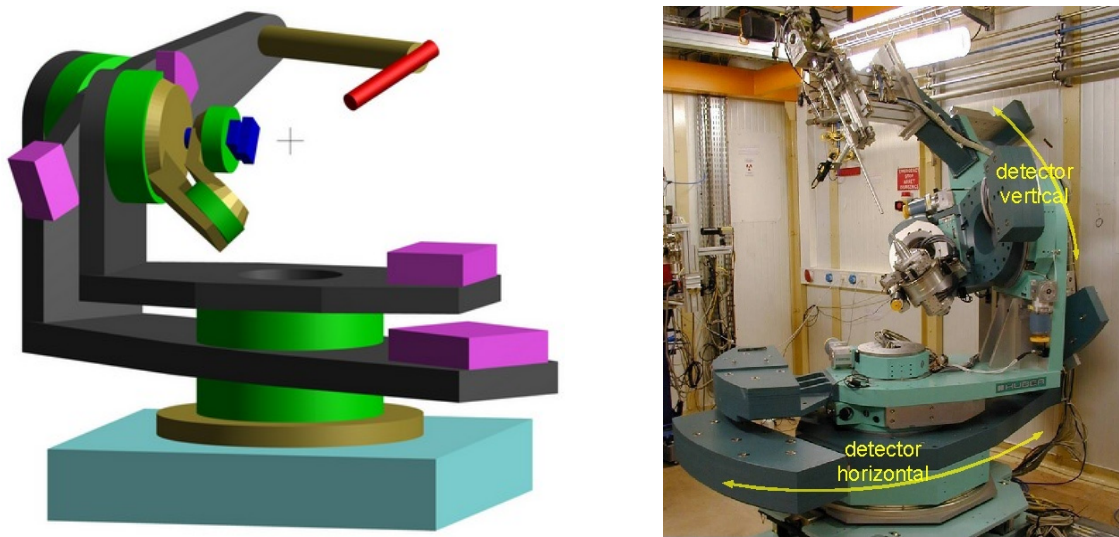


**Fig. 3.9: Schematic and photograph of the diffractometer at the ESRF ID32 beamline.**

### Employed XRD techniques

The different types of XRD experiments performed in this thesis, namely specular  $\theta / 2\theta$  scans, grazing-incident (GI) in-plane and off-plane measurements, pole figures and  $\beta$ -scans,  $\omega$ -scans and reciprocal space maps (RSMs), are illustrated in the following (Tab. 3.1 associates to each technique the utilized XRD equipment).

<b>XRD technique</b>	<b>Employed XRD apparatus</b>
<i>Specular <math>\theta / 2\theta</math> scans</i>	Rigaku DMAX 1500 and Rigaku SmartLab
<i>GI in-plane scans</i>	Rigaku SmartLab and ESRF ID32 diffractometer
<i>GI off-plane scans</i>	ESRF ID32 diffractometer
<i>Pole figures</i>	Rigaku SmartLab
<i><math>\beta</math>-scans</i>	Rigaku SmartLab and ESRF ID32 diffractometer
<i><math>\omega</math>-scans</i>	Rigaku DMAX 1500 and Rigaku SmartLab
<i>RSMs</i>	Rigaku SmartLab

**Tab. 3.1: XRD instruments used for each measurement technique.**

### Specular $\theta / 2\theta$

The  $\theta / 2\theta$  measurement geometry is depicted in Fig. 3.10. Angle of both incoming and exiting beam with respect to the sample surface is  $\theta$ . The incoming beam has a wave vector  $\mathbf{K}_0$  and the scattered beam a wave vector  $\mathbf{K}$ , with  $\mathbf{K}_0 = \mathbf{K}$ . For the occurrence of diffraction, constructive interference of the scattered x-rays must take place, as mentioned above. This is realized when the scattering vector  $\mathbf{Q}$ , defined as the difference between the outgoing  $\mathbf{K}$  and the incoming  $\mathbf{K}_0$  x-ray wave vector,  $\mathbf{Q} = \mathbf{K} - \mathbf{K}_0$  (Fig. 3.10(a)), is a reciprocal lattice vector. The diffraction spectrum is collected by varying the incidence of the primary beam by  $\theta$  and the scattering angle by  $2\theta$ , while recording the diffracted intensity as a function of  $2\theta$ . This is achieved by keeping the sample fixed while rotating both the x-ray source and the detector by  $\theta$  simultaneously, but clockwise and anticlockwise, respectively (this is true for the Rigaku SmartLab; see Fig. 3.11 for further details). Rotations are performed by the so-called *goniometer*, which is the central part of the diffractometer. It consists of two circles or axes of rotation. The sample is placed on the rotational axis, whereas x-ray source and detector move along the periphery around the same rotation axis (Fig. 3.10(b)).

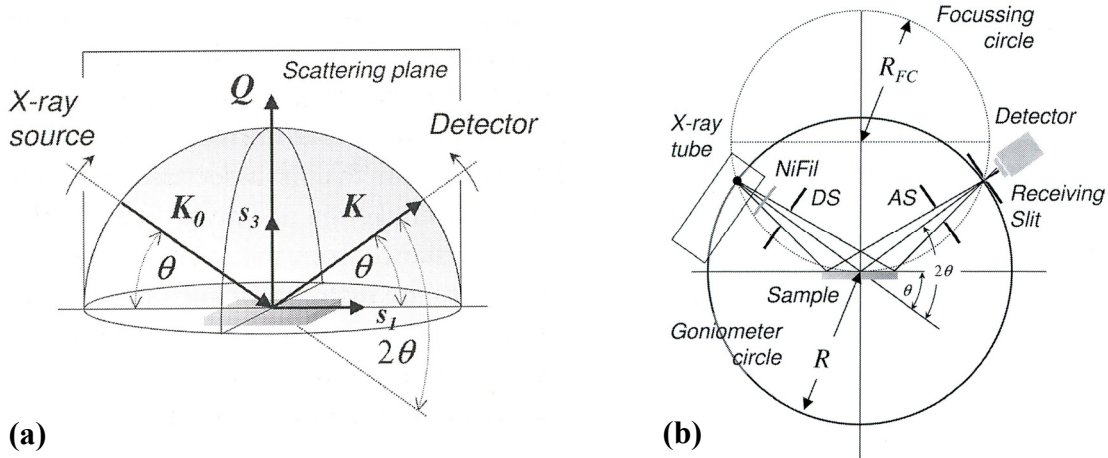


**Fig. 3.10:** Schematic representation of (a) a  $\theta / 2\theta$  scan from the viewpoint of the sample reference frame  $\{s_i\}_{i=1,2,3}$ ; (b)  $\theta / 2\theta$  diffraction in Bragg-Brentano geometry.<sup>154</sup>

The goniometer radius  $R$ , which is the sample-to-detector distance, is  $\sim 18$  cm. The beam conditioning is worked out by means of slits and apertures. The diffractometer operates in the so-called Bragg-Brentano or *parafocusing* mode. In such a configuration, a focusing circle is defined tangentially to the specimen surface. Focusing is obtained when source and detector are positioned at the two intersection points of the focusing circle of radius  $R_{FC}$  with the goniometer circle (Fig. 3.10(b)). Since true focusing is achieved only for a sample that is bent to  $R_{FC}$  and  $R_{FC}$  varies with  $\theta$ , the arrangement is termed parafocusing geometry. In a specular  $\theta / 2\theta$  scan the scattering vector  $Q$  is always parallel to the specimen surface normal ([111] in case of Si(111) substrates, Fig. 3.10(a)). In front of the detector, a graphite monochromator is placed, in order to eliminate the  $K_\beta$  component of the diffracted beam from the desired  $K_\alpha$  line and reduce the background. However, reminding that  $K_\alpha$  is composed of two lines  $K_{\alpha,1}$  and  $K_{\alpha,2}$  separated in  $\lambda$  by less than  $4 \cdot 10^{-4}$  nm, it must be pointed out that, by this setup, the  $K_{\alpha,1}$  and  $K_{\alpha,2}$  cannot be distinguished, and therefore the XRD scans exhibit a double peak structure. Moreover, it is noted that such a method is bulk sensitive, since penetration and, consequently, information depth of the x-rays follows the *Lambert-Beer* law of absorption and is in the range of  $0.1\text{-}10$   $\mu\text{m}$  at normal incidence, whereas the probed area of the sample surface commonly extends to some  $\text{cm}^2$  (Ref. <sup>154</sup>). It must however be pointed out that, in special setups, XRD can be surface sensitive (using grazing incidence of the x-rays onto the sample - see below) and focal sizes down to the sub-100 nm range can be achieved (Refs. <sup>157</sup>-<sup>159</sup>). Both the Rigaku DMAX 1500 and the Rigaku SmartLab were used for specular  $\theta / 2\theta$  studies (Fig. 3.11).

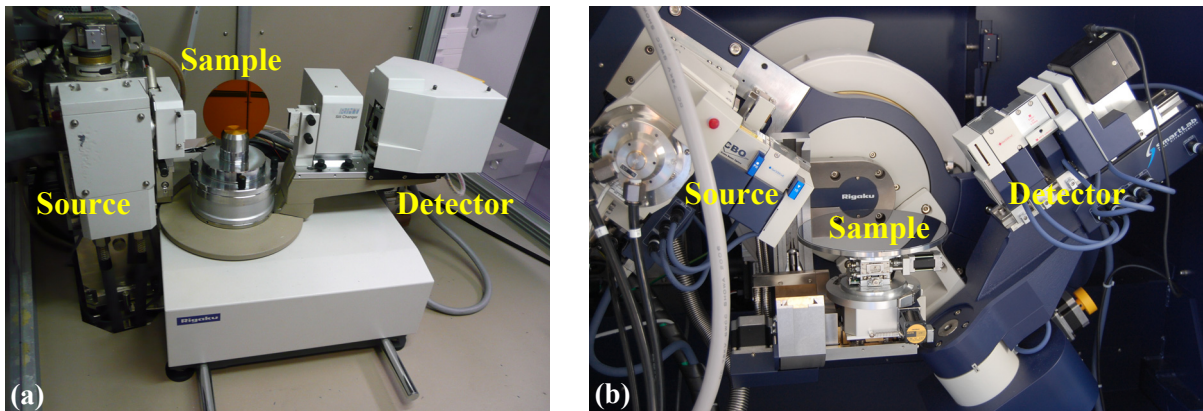


**Fig. 3.11: Bragg-Brentano configuration for specular  $\theta$  /  $2\theta$  analysis. (a) Rigaku DMAX 1500:** X-ray source is fixed; specimen, mounted vertically, and detector are rotated by  $\theta$  and  $2\theta$ , respectively. **(b) Rigaku SmartLab:** sample is mounted horizontally and kept fixed; both x-ray source and detector are rotated by  $\theta$  simultaneously, but clockwise and anticlockwise, respectively.

#### GI in-plane analysis

In-plane scans are performed keeping the scattering vector  $\mathbf{Q}$  in the plane parallel to the wafer surface (Fig. 3.12). The x-rays impinge onto the specimen under grazing incident conditions with an angle  $\alpha_i$ . The diffraction pattern is obtained by rotating the sample by  $\theta$  around its surface normal ([111] in case of Si(111) substrates), while the detector, lying just some tenths of degree ( $\alpha_f$ ) off the plane of the specimen, simultaneously rotates by  $2\theta$ . Since the sample structure is always probed along  $\mathbf{Q}$  in diffraction experiments, an in-plane scan probes the interplanar spacing of lattice planes perpendicular to the wafer surface. The film azimuthal orientation can thus be determined. Contrarily to the specular  $\theta$  /  $2\theta$  configuration, the in-plane one is non-coplanar, because the scattering plane does not contain the specimen surface normal  $\mathbf{s}_3$ . Furthermore, being  $\alpha_i$  fixed, the setup is asymmetric and, therefore, does not obey the conditions of the parafocusing geometry. In fact, the measuring circle and the focusing circle do not intersect throughout the whole scan, but only for a single point. In this circumstance, the divergent beam produced by the x-ray source and scattered by the specimen would enter the detector completely unfocused. That is why the instrument is run in the *parallel beam mode*. In such a configuration, before impinging on the sample, the x-rays are first reflected by a mirror, which reduces the beam divergence in the direction orthogonal to the scattering plane, and then pass through Soller slits, which limit the beam divergence in the scattering plane.

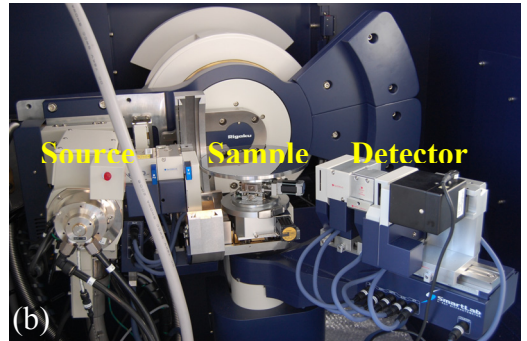
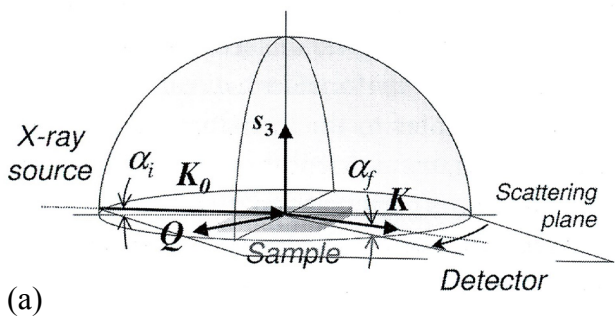


**Fig. 3.12: Measurement setup for GI-XRD in-plane analysis.** (a) Schematic representation and (b) photograph of the Rigaku SmartLab.<sup>154</sup> It is noted from (a) that a certain tiny angle  $\alpha_f$  between detector and sample surface exists. Technically, indeed, no scattered intensity would be collected if the detector were exactly in-plane.

The angle  $\alpha_i$  of incidence of the x-rays on the sample determines the information depth reached during the measurement. For instance, in case of the Ge / cub-Pr<sub>2</sub>O<sub>3</sub> / Si heterostructure, an in-plane measurement run at  $\alpha_i = 0.60^\circ$  ( $\lambda = 0.154$  nm) is bulk-sensitive, that is to say, the whole heterostack is analyzed. At glancing angles below the critical angle  $\alpha_{i,c}$  for total reflection, reflectivity is almost 100% and x-rays only penetrate into the material as an evanescent wave with a typical penetration depth of  $\sim 1$  nm.<sup>155</sup> Reminding that  $\alpha_{i,c}$  of Ge and Pr<sub>2</sub>O<sub>3</sub> at  $\lambda = 0.154$  nm are  $0.31^\circ$  and  $0.34^\circ$ , respectively,<sup>160</sup> for  $0.31^\circ < \alpha_i < 0.34^\circ$  only the Ge / cub-Pr<sub>2</sub>O<sub>3</sub> epilayers will be probed without contributions from the Si substrate, whereas for  $\alpha_i < 0.31^\circ$  just the top Ge film will be investigated (it is noted that this is rigorously true only whenever film thicknesses are higher than the penetration of the x-ray evanescent wave<sup>155</sup>). Thus, varying  $\alpha_i$  turns XRD into a surface-sensitive technique denoted GI-XRD and allows for a depth profile of the heterostructure in a very simple way, which does not require sample preparation and is non-destructive.

**GI *l*-rod scan** Here the measurement configuration is schematized using the reciprocal lattice space as reference frame, with base vectors  $\mathbf{h}$ ,  $\mathbf{k}$  and  $\mathbf{l}$  (Fig. 3.13). As for the previously described in-plane analysis,  $\alpha_i$  is grazing and kept constant. A *l*-rod in the reciprocal lattice is a line featured by a constant  $(h, k)$  pair. A *l*-rod scan is accomplished by keeping the scattering vector  $\mathbf{Q}$  in-plane components  $Q_h$  and  $Q_k$  constant, while changing the out-of-plane one  $Q_l$ , typically from 0.05 to 2 reciprocal lattice units (r. l. u.). In order to follow the scan of  $\mathbf{Q}$ , the detector is moved in-plane by  $\delta$  and in the vertical direction by  $\alpha_f$ . Bragg peaks are observed whenever  $\mathbf{Q}$  coincides with a vector of the reciprocal lattice. Off-plane analyses are decisive for assessing the stacking configuration, type-A or B, of the grown

(111)-oriented heterostructures, as shown in detail by Schroeder et al. for the cub- $\text{Pr}_2\text{O}_3$ (111) / Si(111) system.<sup>119</sup> Of course, for l-rod scans different  $\alpha_i$  can be selected to change the information depth.

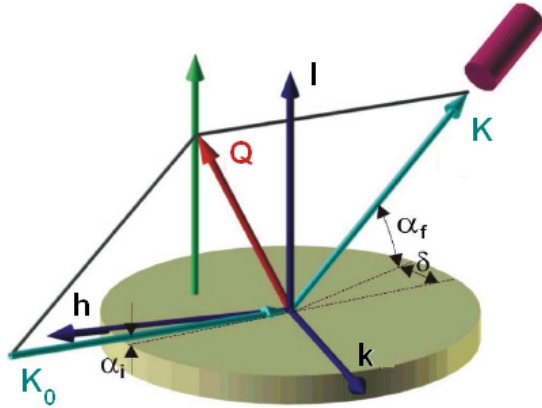


**Fig. 3.13: Sketch of GI l-rod scan.**  $\mathbf{h}$ ,  $\mathbf{k}$  and  $\mathbf{l}$  are the reciprocal space base vectors;  $\mathbf{Q}$  the scattering vector;  $\mathbf{K}_0$  and  $\mathbf{K}$  the incoming and exiting wave vectors, respectively;  $\alpha_i$  the x-ray incident angle;  $\alpha_f$  and  $\delta$  the angles the detector moves by in-plane and out-of-plane, respectively, to accomplish the l-rod scan (adapted from Ref. <sup>161</sup>).

**Pole figures and  $\beta$ -scans** In a conventional specular  $\theta / 2\theta$  diffractogram the lattice planes contributing to a Bragg reflection are all oriented parallel to sample surface. In case of a polycrystalline specimen or a monocrystalline specimen with extended planar defects, only a subset of grains would then be monitored. If the orientation distribution of a family of netplanes is to be fully determined, the corresponding source and detector  $\theta / 2\theta$  configuration, and therefore the scattering vector  $\mathbf{Q}$ , can be fixed, and additional degrees of freedom can be exploited, namely, the tilt angle  $\alpha$  (Fig. 3.14) and the rotation angle  $\beta$  (Fig. 3.15). This is achieved by means of a second goniometer stacked on the  $2\theta$  circle, a so-called Euler cradle (more precisely, a  $\frac{1}{4}$  circle cradle, being the maximum sample tilt limited to  $90^\circ$ ).<sup>154</sup> The tilt angle  $\alpha$  quantifies the extent of inclination of the sample surface with respect to the scattering vector  $\mathbf{Q}$  or with respect to the scattering plane. It can be tuned between  $0^\circ$  ( $\mathbf{Q}$  parallel to the wafer surface  $\rightarrow$  in-plane  $\theta / 2\theta$  scan) and  $90^\circ$  ( $\mathbf{Q} \parallel \mathbf{s}_3 \rightarrow$  specular  $\theta / 2\theta$  analysis), by tilting the specimen around  $\mathbf{s}_1$ , which coincides with the x-ray beam projection onto the wafer and a specific in-plane crystallographic direction in the sample, e.g., Si[11-2] in case of a Si(111) substrate.  $\mathbf{s}_1$  can be adjusted by changing the rotation angle  $\beta$ , which measures the azimuth of the sample in the surface plane and can be varied between  $0^\circ$  and  $360^\circ$ . The pole figure of a family of netplanes is realized by measuring the diffracted intensity

for a fixed  $\theta / 2\theta$  setup at all  $(\alpha, \beta)$  pairs allowed by the Euler cradle, namely  $0^\circ < \alpha < 90^\circ$  and  $0^\circ < \beta < 360^\circ$  (Fig. 3.15). It is remarked that the angular scan performed by keeping  $\alpha$  fixed and varying  $\beta$  by  $360^\circ$  around the sample surface normal is often called an off-plane  $\beta$ -scan (or  $\phi$ -scan in case the rotation angle is defined as  $\phi$ ). Pole figures were performed with the Rigaku SmartLab in parallel beam mode.

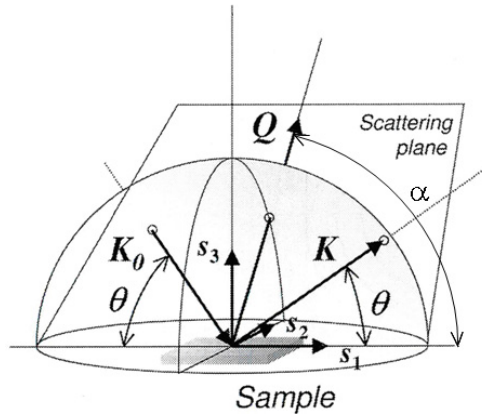


**Fig. 3.14:**  $\alpha$  tilt from the viewpoint of the sample reference frame. The scattering vector and plane are tilted away from the specimen surface towards the  $s_2$  axis. Fig. adapted from Ref<sup>154</sup>.

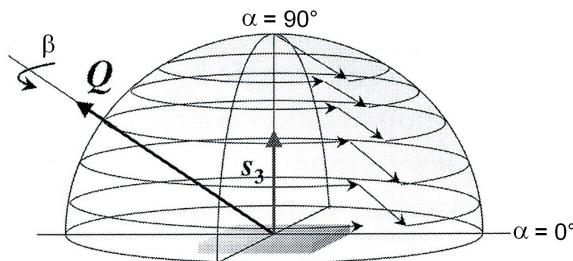


**Fig. 3.15:** Course of the scattering vector  $Q$  during a pole figure measurement (adapted from Ref<sup>154</sup>).

**Reciprocal space maps** In order to understand the concept of RSM, it is useful to introduce the so called *rocking curve* or  $\omega$ -*scan* technique, depicted in Fig. 3.16. The rocking curve is carried out by fixing the detector on the  $2\theta$  circle to the centroid position  $2\theta_0$  of the Bragg peak under investigation, whereas the specimen is *rocked* on the  $\theta$  circle in the vicinity of the Bragg angle  $\theta_0$ . When varied independently of  $2\theta$ , the  $\theta$  angle is called  $\omega$  and it is defined as the deviation from half the scattering angle of the symmetric position,  $\omega = \theta - 2\theta_0 / 2$ . For fixed  $2\theta_0$ , the scan angle  $\omega$  is restricted to the range between  $-\theta_0$  and  $+\theta_0$  (out of these limits the incoming / exiting beam would decline beneath the specimen surface with no scattering information from the thin film collectable). A rocking curve provides information about the film texture. For instance, in case of a Ge(111) epilayer the rocking curve of the

(111) lattice planes allows for the determination of the amount of (111) planes tilted with respect to the Ge(111) film surface, and the extent of the tilt. This method does not require a Euler cradle (decoupled  $\theta$  and  $2\theta$  circles are sufficient) and can therefore also be performed with the Rigaku DMAX 1500, as far as Bragg peaks of planes parallel to the wafer surface are rocked.

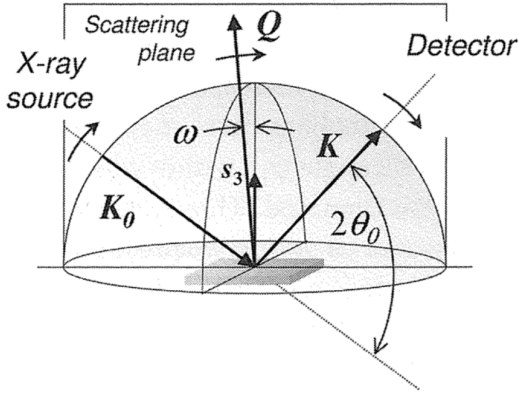


**Fig. 3.16:** Rocking curve measurement from the point of view of the sample reference frame. The scattering angle is fixed to the centroid of the reflection,  $2\theta_0$ , whereas the rocking angle  $\omega$  is tilted around  $\theta_0$ .<sup>154</sup>

A RSM is performed such that the Bragg reflection under investigation is fully mapped in a confined area in  $\mathbf{Q}$  space. This means that the reflection is not monitored only by one rocking curve crossing it, but the whole area in its vicinity is included in the measurement. One way of mapping consists in performing subsequent rocking curves with increasing scattering angle  $2\theta$  in a range centered around  $2\theta_0$ . The  $\theta / 2\theta$  scan will proceed along the ordinate, which is the out-of-plane component  $Q_z$ ,  $Q_z = K \cdot [\cos(\theta-\omega)-\cos(\theta+\omega)]$ , being  $K = 2\pi/\lambda$  the magnitude of the x-ray wave vector. This is visualized in Fig. 3.17(a), where the different configurations during the  $\theta / 2\theta$  scan are symbolized by changing gray scales of the vectors involved. The rocking curve along  $Q_x$ ,  $Q_x = K \cdot [\sin(\theta-\omega)+\sin(\theta+\omega)]$ , transforms from a horizontal line to a circular one, as shown by the fact that the magnitude of the momentum transfer  $\mathbf{Q}$  remains constant (Fig. 3.17(b)). RSMs around the Ge(111) Bragg peak were performed with the Rigaku SmartLab tool, run in parallel beam mode with a mirror and a Ge(400) twofold channel-cut on the primary side of the diffractometer, in order to reduce the beam divergence in the direction perpendicular to the sample surface.

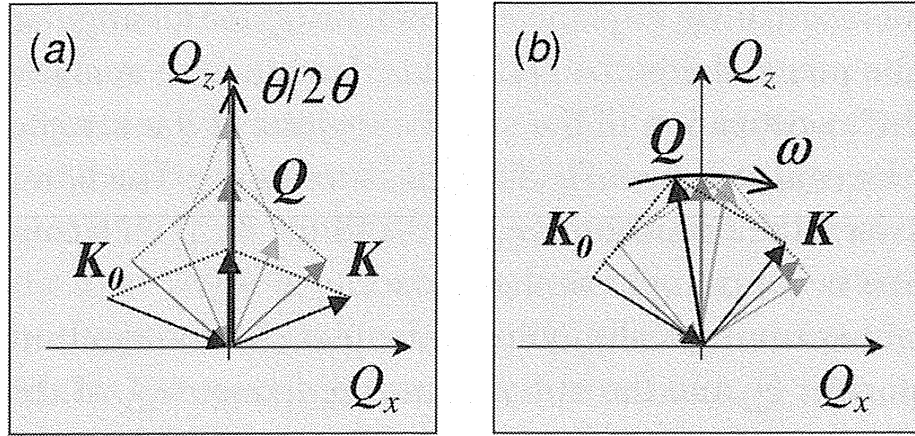


**Fig. 3.17: Comparison between (a) symmetric  $\theta / 2\theta$  scan and (b) a rocking curve scan.**<sup>154</sup>

### The hex-Si(111) surface coordinate system

At this point, it is worthwhile to introduce the Si(111) hex-like surface coordinate system. The transformation from cub-bulk coordinates into Si(111) surface ones can be derived from the real space surface unit cell, spanned by the lattice vectors

$$\mathbf{a}_1^S = \frac{1}{2} \cdot \begin{bmatrix} 1 \\ \mathbf{0} \\ -1 \end{bmatrix} \cdot \mathbf{a}^B \quad \mathbf{a}_2^S = \frac{1}{2} \cdot \begin{bmatrix} 1 \\ 1 \\ 0 \end{bmatrix} \cdot \mathbf{a}^B \quad \mathbf{a}_3^S = \frac{1}{3} \cdot \begin{bmatrix} 1 \\ 1 \\ 1 \end{bmatrix} \cdot \mathbf{a}^B \quad (3.5)$$

where  $\mathbf{a}^B$  is the base vector in the cub-system. Hence, the matrix realizing the conversion reciprocal hex surface coordinates-to-reciprocal cubic bulk coordinates is

$$\begin{bmatrix} h \\ k \\ l \end{bmatrix}^B = \frac{1}{6} \cdot \begin{bmatrix} 4 & \bar{4} & 6 \\ 4 & 8 & 6 \\ \bar{8} & \bar{4} & 6 \end{bmatrix} \cdot \begin{bmatrix} h \\ k \\ l \end{bmatrix}^S \quad (3.6)$$

Now the convenience of such a coordinate system change becomes evident. For instance, the  $[h00]^S$  direction is parallel to  $[11-2]^B$  (also  $[11-2]$  without apex hereafter) and the  $[hk0]^S$  to  $[1-10]$ , so that scans along  $[11-2]$  and  $[1-10]$  are normally called  $h^S$  and  $h^S=k^S$  scans, respectively (Fig. 3.18). This is of course valid also for Ge, whose (111) surface is hex-like. For cub- $\text{Pr}_2\text{O}_3$ , the fact that its bixbyite structure has a lattice constant twice that of Si and that the film grows with a type-B orientation on the Si(111) substrate must be considered, and the correct transformation matrix results in

$$\begin{bmatrix} h \\ k \\ l \end{bmatrix}^B = \frac{1}{3} \cdot \begin{bmatrix} \bar{4} & 4 & 6 \\ \bar{4} & \bar{8} & 6 \\ 8 & 4 & 6 \end{bmatrix} \cdot \begin{bmatrix} h \\ k \\ l \end{bmatrix}^S \quad (3.7)$$

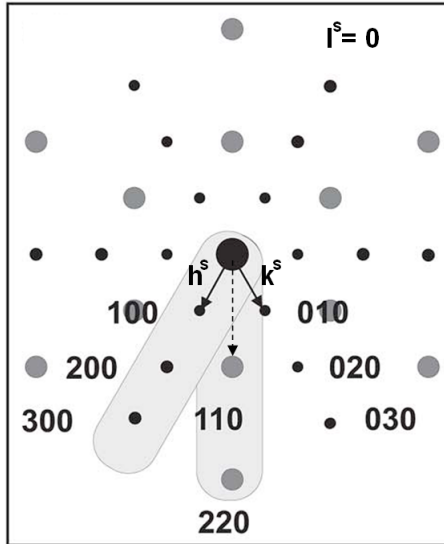


**Fig. 3.18:** Schematic of the Si(111) surface and hex-coordinate system ( $l^S = 0$ ). Solid arrows define the  $h^S$  and  $k^S$  directions, the dashed arrow the  $h^S = k^S$  direction.

### 3.2.1.2 X-ray Reflectivity

X-ray reflectivity or reflectometry (XRR) allows for the determination of refractive index, thickness, and surface and interface roughness of a thin film or multilayer. In this method the diffractometer is operated in the symmetric  $\theta / 2\theta$  configuration, but with much smaller  $\theta$  angles than those in  $\theta / 2\theta$  diffraction (typically in the range  $0^\circ - 8^\circ$ ). In case of the Rigaku DMAX 1500, the Bragg-Brentano configuration is used, with the smallest divergence slit available ( $0.05^\circ$ ). For the Rigaku SmartLab operating in parallel beam mode, a beam divergence in the scattering plane as low as  $0.025^\circ$  can be achieved by employing, in sequence on the primary side of the diffractometer, a mirror, a crystal collimator (Ge(400) two-fold channel-cut) and the smallest divergence slit usable.

A reflectogram is generally presented as an intensity plot versus scattering angle  $2\theta$ , with the ordinate given on a logarithmic scale to cover the many orders of magnitude by which the reflected intensity can vary. As an example, Fig. 3.19 depicts the simulated XRR patterns from a quartz glass substrate of various surface *root mean square roughness* values  $\sigma$ .

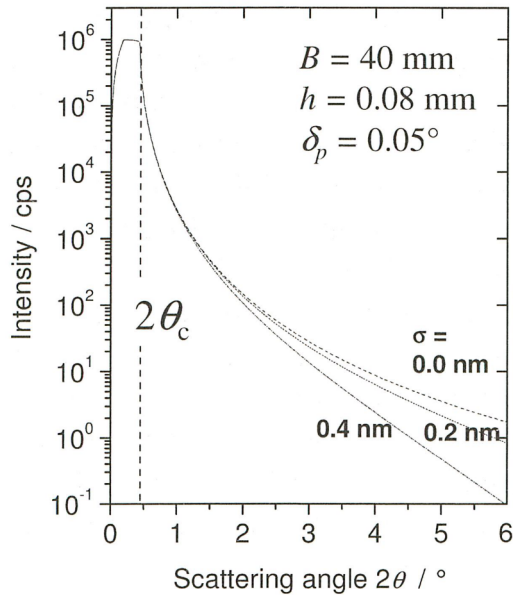


**Fig. 3.19:** Simulated Cu K $\alpha$  radiation XRR scans from a quartz glass substrate with different surface roughness values  $\sigma$ .  $B$  and  $h$  denote the substrate length and thickness, respectively;  $\delta_p$  indicates the beam divergence.<sup>154</sup>

First of all, it is noted that the curve is dividable into three different regions: a first one of increasing intensity, then an intensity plateau and finally a region of steeply decreasing intensity over several orders of magnitude. The region of increasing intensity goes from an angle of incidence of almost  $0^\circ$ , configuration in which part of the beam is cut by the sample, to  $\sim 0.2^\circ$ , at which the whole photon flux impinge on the specimen. Then, a plateau is recorded for scattering angles up to the critical angle  $\theta_c$ , which depends on the material, and is caused by the total reflection of the primary beam. Since in this region almost all the photons emitted by the x-ray source would be reflected into the detector, a beam attenuator is inserted into the beam path, reducing the beam intensity by  $\sim 420$  times and avoiding any beam-damage. At the critical angle  $\theta_c$ , a transition occurs to the so called *Porod* regime, in which the intensity drops with the inverse fourth power of the wave vector transfer  $\mathbf{Q}$ , namely  $1/\mathbf{Q}^4 = (4\pi\lambda/\sin\theta)^4$ . Recalling that the refractive index  $n$  can be written as  $n = 1 - \delta - i\beta$  and that  $\theta_c = (2\delta)^{1/2}$ , the XRR spectrum of Fig. 3.19 can be fitted making use of the ratio of the reflected intensity  $I_R$  to the incident intensity  $I_0$

$$\frac{I_R}{I_0} = \left| \frac{\theta - \sqrt{\theta^2 - \theta_c^2 - 2i\beta}}{\theta + \sqrt{\theta^2 - \theta_c^2 - 2i\beta}} \right|^2 \quad (3.8)$$

which can be derived by considering the continuity of the tangential electric field component of the incident, refracted and exiting beam.<sup>154</sup> In this way,  $\delta$  and  $\beta$  can be estimated and, from those, the electron density and attenuation length of the material, respectively. Concerning the Porod regime, it is experimentally found that the strong signal decrement is accentuated by surface roughness and that the slope can be fitted by multiplying Eq. (3.8) with a *Debye-Waller factor*-like term  $\exp(-\sigma^2 Q^2)$ .

Fig. 3.20 shows the XRR scan of a 25 nm-thick Ta<sub>2</sub>O<sub>5</sub> film on a quartz glass substrate, in case of ideal surface / interface smoothness (black curve) and some surface / interface roughness (grey plot).

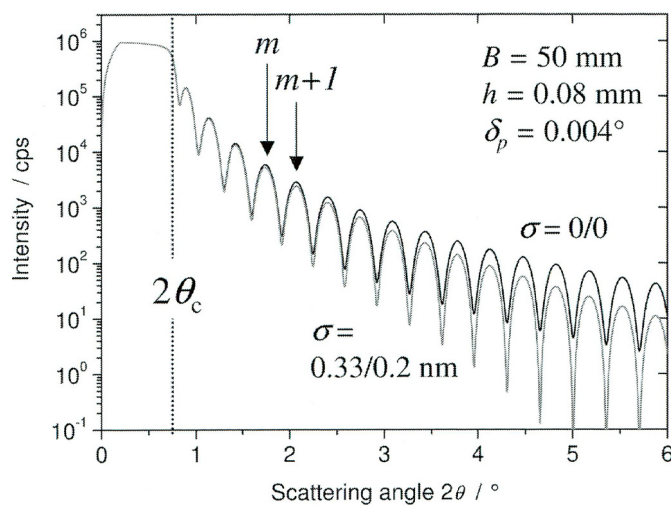


**Fig. 3.20: XRR simulation of a 25 nm-thick Ta<sub>2</sub>O<sub>5</sub> film on a quartz glass substrate for Cu K $\alpha$  radiation. Upper (black) curve for smooth surface; lower (grey) curve for 0.2 nm interface roughness and 0.33 nm surface roughness.<sup>154</sup>**

The most remarkable difference with respect to Fig. 3.19 is the appearance of oscillations in the region of steeply decreasing intensity, the so called *Kiessig* fringes, whose maxima are observed whenever the phase difference  $\Delta$  between the reflected and refracted beam,  $\Delta = (AB + BC)n - AD$ , is a multiple of a wavelength  $\lambda$  (Fig. 3.21). A closer inspection of Fig. 3.21 reveals that  $\Delta = 2t \sin \theta_t$ , where  $t$  is the layer thickness and  $\theta_t$  is the angle the transmitted wave forms with respect to the surface. Interestingly, the phase shift relation resembles the Bragg equation, with the film thickness replacing the interplanar distance  $d$ . Assigned an index  $m$  to each oscillation, it can be demonstrated that the distance between two adjacent fringes significantly above  $\theta_c$  scales like  $2\theta_{m+1} - 2\theta_m \sim \lambda/t$  and is thus proportional to  $1/t$ . Although the oscillation separation increases for higher orders  $m$ , it is noted that the maximum thickness of a thin film measurable by XRR is limited by the beam divergence. With the high-

resolution setup of the Rigaku SmartLab (mirror, channel-cut and smallest divergence slit), layers up to  $\sim 500$  nm can be investigated. Fitting of the curves in Fig. 3.20 requires a more complex formalism than Eq. 3.8, which is valid only in case of an ideally smooth substrate material (consult for instance Ref.<sup>154</sup>). Typically, the determination of refractive index, film thickness and surface roughness is achieved by means of reflectometry computer programs.<sup>162</sup> It is noted that the concepts discussed in this chapter for a substrate material or a single thin film / substrate system can be easily extended to multilayer structures.<sup>154</sup>

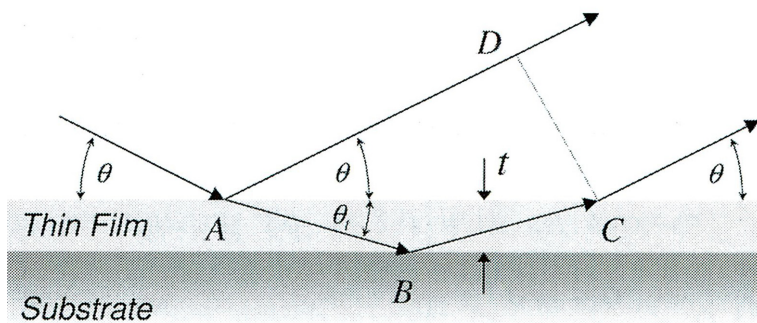


**Fig. 3.21:** Sketch of reflected and refracted beams for the derivation of their phase difference  $\Delta$ .<sup>154</sup>

## 3.2.2 Additional methods

### 3.2.2.1 Reflection High Energy Electron Diffraction

An *EK 35 RHEED* apparatus from *STAIB Instruments* is mounted on each deposition chamber of the MBE tool to in-situ follow the film growth. It basically consists of an electron gun and a screen on two diametrically opposite sides of the chamber. The electron gun produces an electron beam with small angular divergence, which is sent onto the specimen with a grazing incident angle  $\theta$  of  $\sim 2^\circ$  by means of an electromagnetic deflector. The beam energy is set to 15.8 kV. The beam diffracted from the sample surface form a pattern on a fluorescent screen. Different azimuths of the specimen can be studied by rotating the wafer around its surface normal.

The Bragg peak intensity distribution in a RHEED pattern can be understood considering the kinematical scattering theory. The two conditions for diffraction to occur, namely, energy conservation  $\mathbf{K} = \mathbf{K}_0$  and momentum conservation  $\mathbf{K} - \mathbf{K}_0 = \mathbf{Q}$  with the scattering vector  $\mathbf{Q}$  equal to a vector  $\mathbf{G}$  of the reciprocal lattice, can be cast into the geometrical construction of the *Ewald sphere* (Fig. 3.22).  $\mathbf{K}_0$ , which indicates the direction of the impinging electron beam, is defined so that its tip ends on the origin of the reciprocal lattice. The Ewald sphere is then built up with center on the origin of  $\mathbf{K}_0$  and radius equal to  $K_0$ . Reflections occur only for wave vectors  $\mathbf{K}$  connecting the origin of the sphere with a reciprocal lattice point lying on the sphere. It is noted that, for a beam energy of 15.8 KeV,  $K_0$  is  $\sim 620 \text{ nm}^{-1}$ , which is some tens of times larger than a typical reciprocal lattice unit. Consequently, the Ewald sphere produces an almost planar cut through the first few Brillouin zones of the reciprocal lattice. The electrons, arriving on the sample with a grazing angle  $\theta$  of  $\sim 2^\circ$ , have a penetration depth reduced to the very surface, so that the periodic structure of the crystal beneath the surface can be neglected. Thus the probed volume can be approximated by a two-dimensional layer, and the reciprocal lattice degenerates into a set of one-dimensional rods along the  $z$  direction perpendicular to the surface (Fig. 3.22). The rod on which the arrow of  $\mathbf{K}_0$  terminates is the (00) rod, that is to say, the origin of the reciprocal lattice. Since the reciprocal lattice consists of continuous rods, every rod produces a reflection in the diffraction pattern. The reflections occur on so-called *Laue circles* of radius  $L_n$  centered at  $H$ , the projection of  $(\mathbf{K}_0)_\parallel$  onto the screen (Fig. 3.22).  $S$  is named *specular reflection* or *spot*, because the angle of incidence equals the angle of reflection. It is located at the intersection of the zeroth-order Laue circle

with the (00) rod. In this case, the scattering vector  $\mathbf{Q}$  is perpendicular to the sample surface, as in XRD specular  $\theta$ - $2\theta$  scans.  $I$  is the projection of the origin of the reciprocal lattice (000) onto the screen and it is not visible, as it is intercepted by the sample (except in case, for special sample geometries, part of the incident beam misses the specimen).

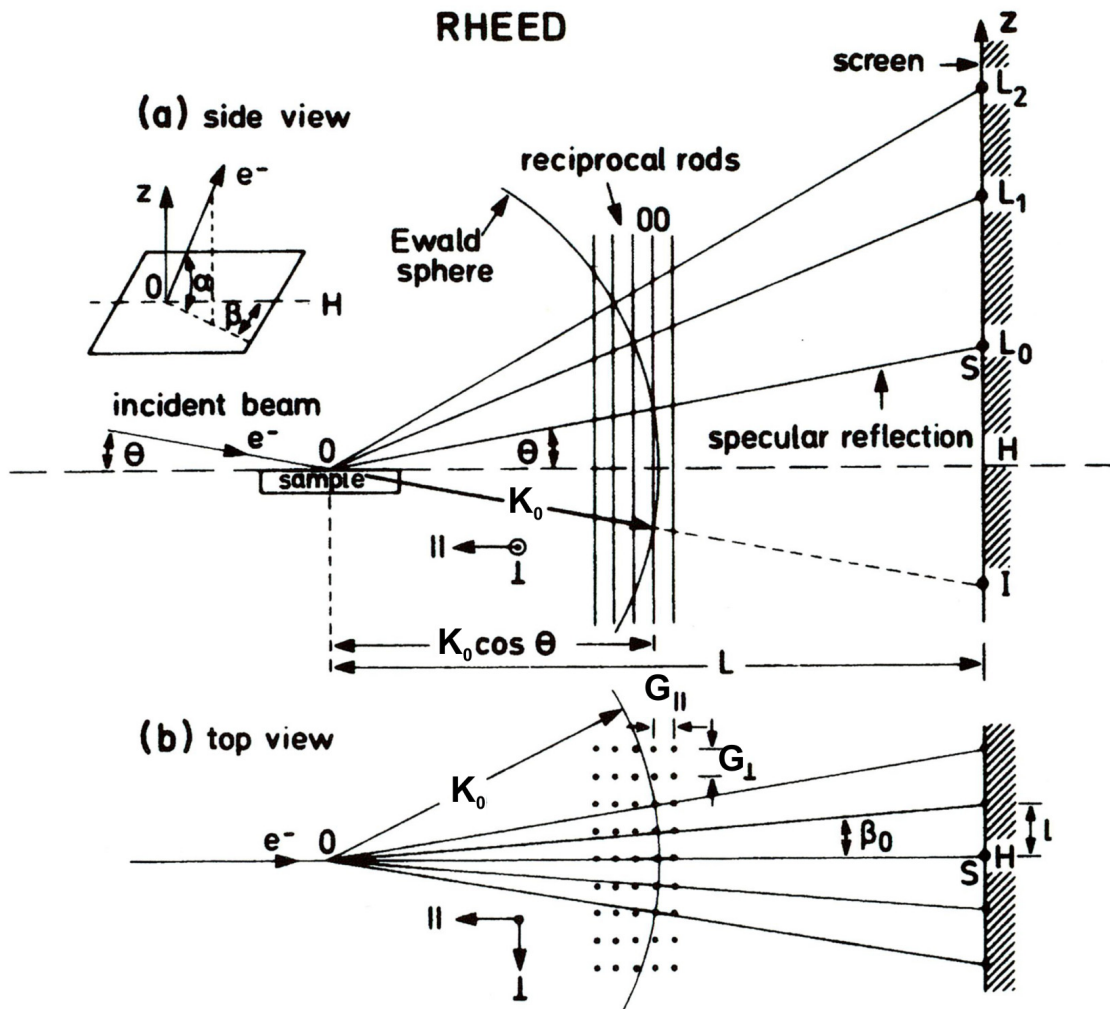


**Fig. 3.22: (a) Side view; (b) top view of Ewald sphere construction and RHEED diffraction geometry. Intensity maxima on the screen correspond to projected intersections of the Ewald sphere with the reciprocal lattice. Adapted from Ref. <sup>163</sup>.**

It can be easily demonstrated that the reciprocal lattice rod separations parallel ( $nG_{\parallel}$ ) and orthogonal ( $nG_{\perp}$ ) to the beam direction are

$$nG_{\parallel} = K_0 \left[ \cos \theta - \frac{1}{\sqrt{(L_n/L)^2 + 1}} \right] \quad (3.9)$$

$$nG_{\perp} = \frac{K_0}{\sqrt{(L/nl)^2 + 1}} \quad (3.10)$$

where both  $nG_{\parallel}$  and  $nG_{\perp}$  are measured from the central (00) rod. From these parameters the arrangement of the atoms on the surface can be gathered.

For electron diffraction, a surface is regarded as flat when terrace widths are larger than the distance over which electron interfere coherently, which is typically of the order of  $1\mu\text{m}$ .<sup>164</sup> In this case, the RHEED pattern consists of concentric semicircles of point-like spots at the Laue-Ewald conditions. This occurs, for instance, for a Si(111) (7x7)-reconstructed surface from a Si substrate. However, when the surface of an epitaxially grown film is analyzed, streaks are generally observed, owing to the limited long-order range of the surface periodic structure. As an example, a 2D-array of lattice points with finite size  $L_1$  and  $L_2$ , perpendicular and parallel to the incident electron beam direction, respectively, is sketched in Fig. 3.23(a). It can be seen that the corresponding RHEED image does not consist of sharp spots as in the case of an ideal surface, but of streaks with width inversely proportional to  $L_1$  and length inversely proportional to  $L_2 \cdot \tan\theta$  (Fig. 3.23(c)).

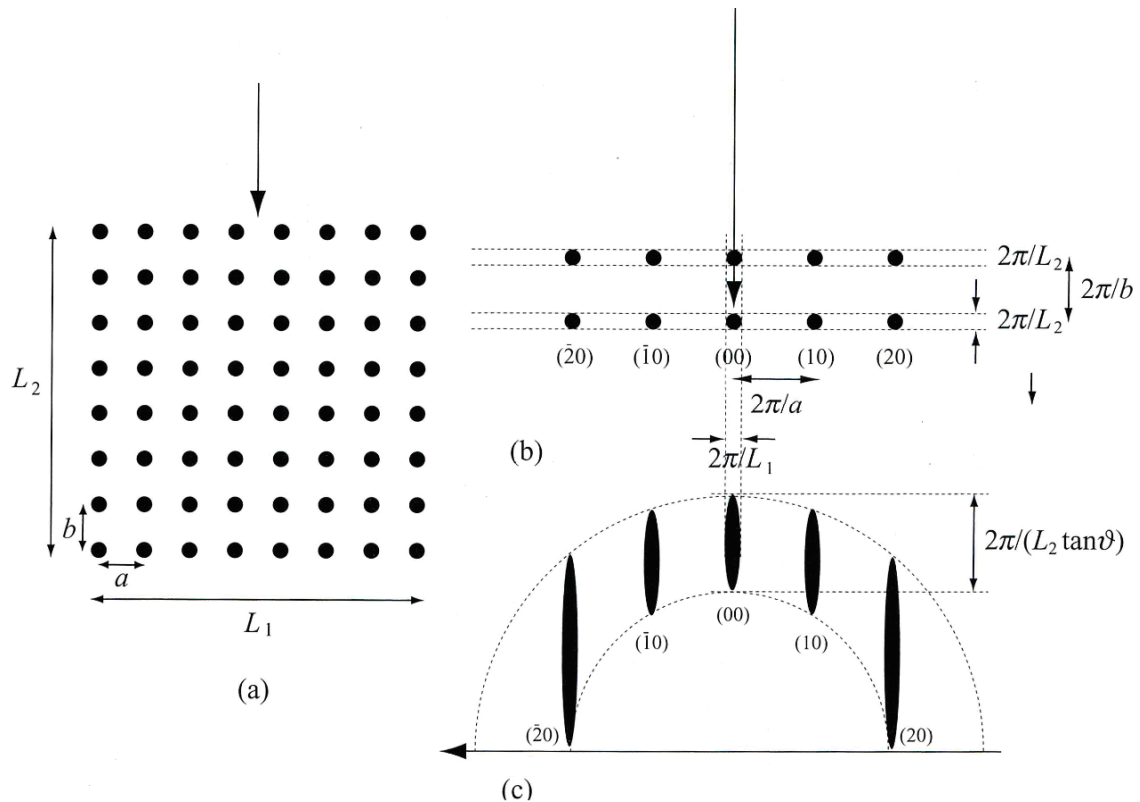


**Fig. 3.23:** (a) 2D direct lattice with finite size. Arrow indicates the electron beam direction. (b) Reciprocal lattice for (a). (c) RHEED construction for (b).<sup>164</sup>

If features with small lateral dimensions are present on the surface, e.g., islands, or simply the surface roughness is very high, the observed pattern is different from the one described above. In fact, the impinging electrons scatter from planes further inside the crystal than for a flat surface, thus probing the periodicity of the sample also in the  $z$  direction. The reciprocal lattice turns from an array of continuous rods into an array of points, each broadened due to the finite size of the scattering region. At the considered low scattering angles, the Ewald sphere can be approximated by a plane cutting a broadened 3D lattice, resulting in a spotty pattern. The more planes participate to the scattering, the weaker the signal between the diffraction spots on the screen is, so that there might be only the remnant of a streak or none at all. Finally, it is noted that another factor giving rise to broadening of the RHEED features resides in the divergence of the beam, which has been neglected so far. Due to that, the Ewald sphere is indeed a spherical shell with a finite thickness rather than a sphere, so that its intersection with the reciprocal lattice rods or spots is not ideally-sharp.

### 3.2.2.2 Photoelectron Spectroscopy

The photoelectron spectroscopy (PES) analysis chamber is integrated within the MBE complex (Fig. 3.24). This offers the advantage that growth studies can be performed without breaking UHV, just by transferring the sample in-situ from one of the growth chambers into the photoelectron spectroscopy (PES) one.

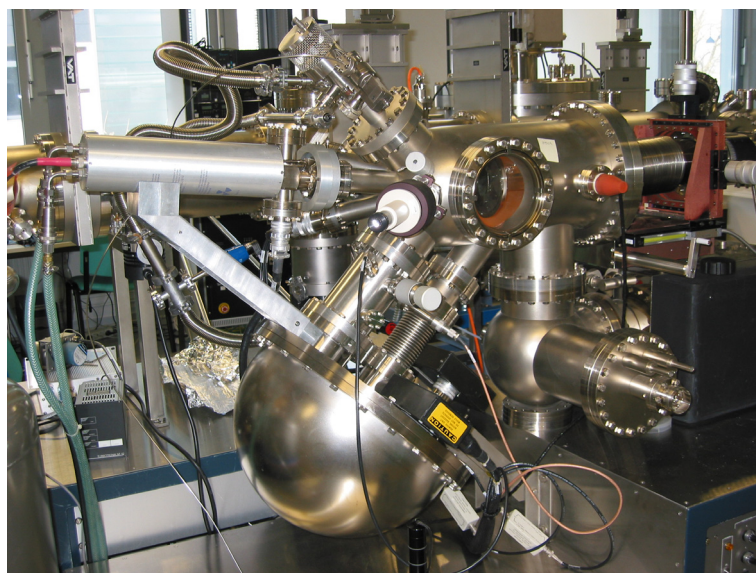


**Fig. 3.24: Photograph of the PES tool integrated into the MBE facility. The PES chamber is pumped by a dedicated ion getter pump.**

The technique is named x-ray or ultra-violet (UV) photoelectron spectroscopy (XPS or UPS, respectively), depending on which energy is chosen for the primary radiation. In the employed apparatus, non-monochromatized Al K<sub>α</sub> (1486.6 eV) or He I (21.2 eV) can be selected. In both cases, the concept is the measurement of the kinetic energy E<sub>k</sub> with which the photoelectrons are ejected from the illuminated sample (Fig. 3.25).

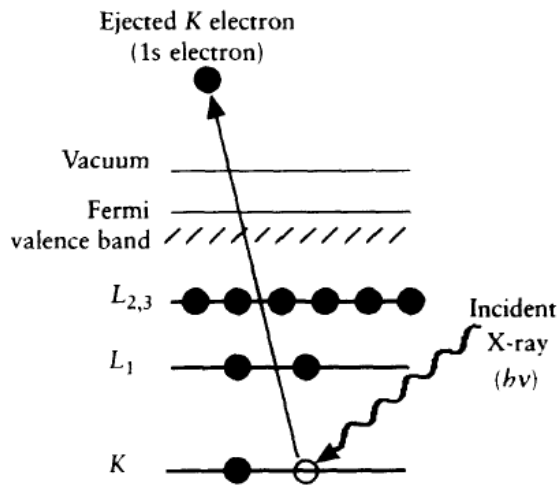


**Fig. 3.25:** Sketch of the XPS process, showing photo-ionization of an atom by the ejection of a 1s electron.<sup>165</sup>

Irradiation with x-ray allows for the study of core levels, whereas UV photons are used to characterize the specimen valence band.<sup>166</sup> The emitted photoelectrons are collected by a *Physical Electronics PHI 10 - 360* hemispherical energy analyzer, whose principle of functioning is explained in Fig. 3.26. Knowing the energy of the impinging photons (hv) and the analyzer work function  $\phi_A$ , it is immediate to calculate the *binding energy* E<sub>B</sub> of the emitted electrons from the formula  $E_B = h\nu - E_k - \phi_A$ , originally postulated by Einstein.<sup>167</sup> The PES spectrum will reproduce the electronic structure of an element quite accurately, since all the electrons with  $E_B < h\nu$  will feature in the spectrum. Thus, the chemical composition of the studied material can be identified, even in a quantitative way when the factors converting PES signal intensities into relative atomic concentrations are known for each element in the compound.<sup>168</sup> Moreover, it is interesting to note that, when different elements are brought together in a chemical compound, electrons interact and, consequently, their orbitals get altered. Valence electrons form new, combined molecular orbitals, and core electrons also change in energy because of charge transfer and screening effects of the nucleus in the new environment. Binding energy shifts hence enable the identification of the chemical state of the emitting atom.

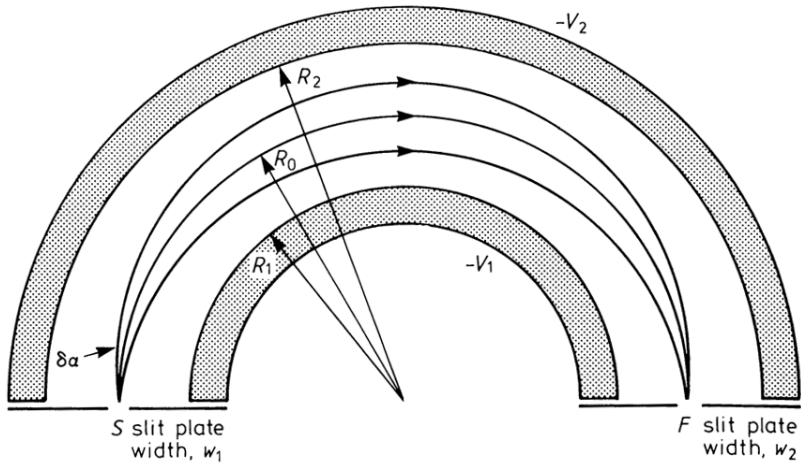


**Fig. 3.26: Schematic cross-section of a concentric hemispherical analyzer (CHA).** Two stainless steel hemispheres of radii  $R_1$  (inner) and  $R_2$  (outer) are positioned concentrically. Potentials  $-V_1$  and  $-V_2$  are applied to the inner and outer spheres, respectively, with  $V_2 > V_1$ .  $R_0$  is the radius of the median equipotential surface, with potential  $-V_0 = (V_1 R_1 + V_2 R_2) / 2R_0$ . The source S, located in the entrance slit of width  $w_1$ , and the focus F in the exit slit of width  $w_2$  are collinear with the centre of curvature. Only electrons entering the analyzer entrance slit S with a kinetic energy  $E_k = eV_0$  follow the trajectory along the median equipotential surface of radius  $R_0$  and are focused at the exit slit F ( $\delta\alpha$  denotes the electron divergence from the ideal tangential path). Scanning  $V_1$  and  $V_2$  selectively passes electrons of varying kinetic energy into the detector. Actually, in order to have the same absolute resolution at all energies in the spectrum, it is preferred to retard electrons to a fixed kinetic energy, the so called *pass energy*, before they enter the energy analyzer, instead of changing  $V_1$  and  $V_2$ . It can be easily shown that energy resolution is improved by decreasing the pass energy.<sup>169</sup>

PES is a surface sensitive method, owing to the short (at maximum few nm) *inelastic mean free path* (IMFP) of the photoelectrons.<sup>170</sup> The created photoelectrons can indeed travel a distance, characterized by the *attenuation length*  $\Lambda$  in the matrix (Fig. 3.27), of only few nm before being inelastically scattered and no longer appearing in the PES peak. It is noteworthy to point out the enormous difference in attenuation length for photons and electrons having the same energy, e.g., Al K $\alpha$  photons at normal incidence have an attenuation length of almost 8  $\mu\text{m}$  in Si, whereas electrons with the same energy (1486.6 eV) have an attenuation length of just a couple of monolayers (Fig. 3.27). The intensity  $I$  of electrons emitted from all depths greater than  $d$  at an angle  $\theta$  to the surface normal is given by the Lambert-Beer law,  $I = I_0 \exp(-d/\Lambda \cos\theta)$ , where  $I_0$  is the intensity from an infinitely thick, uniform substrate. An immediate consequence of this formula is that, by changing the tilt of the sample with respect to the detector, it is possible to vary the escape depth of the photoelectrons and therefore the information depth (always within few nm however). Thus, PES can provide a non-destructive depth profile of a specimen in case of ultra-thin films. Regions deeper than few nm from the

surface can be accessed only by removing material by mechanical, chemical or ion sputtering methods.

Details about PES can be found in Refs.<sup>165,166,169,171</sup>.

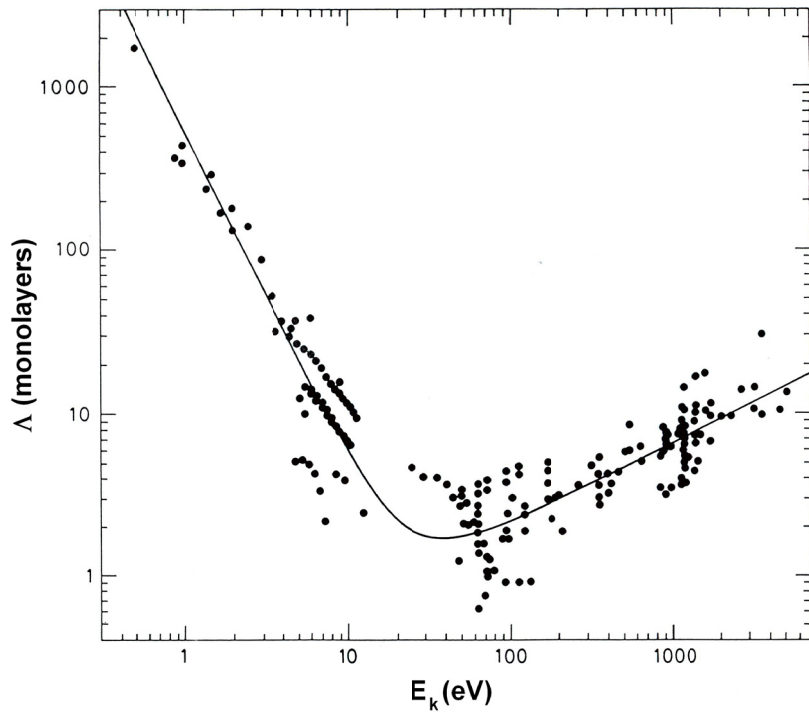


Fig. 3.27: The dependence of attenuation length on the emitted electron energy for elements.<sup>169</sup>

### 3.2.2.3 Dynamic Secondary Ion Mass Spectroscopy

When a high energy (typically between some hundreds eV and 15 keV) beam of ions bombards a surface, the energy is transferred to the atoms of the solid by a billiard-ball-type collision process, which is generally referred to as *collision cascade*. As a result, secondary particles, e.g., electrons, neutral species atoms or molecules, atomic and cluster ions, are emitted from the top layers of the solid, at points which can be up to 10 nm far away from the point of primary impact. In secondary ion mass spectrometry (SIMS), of all the ejected species the secondary ions are measured with a mass spectrometer, allowing for the determination of the elemental, isotopic, or molecular composition of the specimen surface. The SIMS instrument employed in this thesis is the *CAMECA IMS WF* dynamic SIMS (D-SIMS) available at the IHP laboratories and photographed in Fig. 3.28 (for the differences between D-SIMS and static SIMS, Refs.<sup>172,173</sup> can be consulted). D-SIMS operates in UHV and is the technique of choice whenever the depth profile of a thin film (insulators,

semiconductors, metals) is to be performed. Indeed, it provides a unique combination of extremely high sensitivity for all elements from hydrogen to uranium (detection limit down to part-per-billion level for many elements), high lateral resolution imaging (down to 40 nm), and a very low background that allows high dynamic range (more than 5 decades). The basic components of the *CAMECA IMS WF D-SIMS* are the two ion columns, one for  $O_2^+$  and one for  $Cs^+$  ions, and the mass analyzer. The reason why two primary ion beam sources are used resides on the fact that the ionization yield of most elements varies by decades depending on the chemical environment. Oxygen and caesium are capable of enhancing, respectively, positive and negative secondary ion intensity by 2 to 3 orders of magnitude compared to the use of noble gas ions.  $Cs^+$  ions, employed to study the purity of the Ge epilayer grown on top of the cub- $Pr_2O_3(111)$  / Si(111) heterostructure, are produced as follows. Caesium vapour is generated from a caesium chromate ( $Cs_2CrO_4$ ) or a caesium carbonate ( $Cs_2CO_3$ ) tablet contained in a reservoir raised to a temperature of 400°C. In the vapour state, caesium ionizes into positive ions  $Cs^+$  when it comes into contact with the surface of a tungsten plate at a temperature of 1100°C. Both reservoir and ionizer are heated independently by electric bombardment by means of two annular filaments. An extraction electrode, placed in front of the ionizer, at a potential of 0 V (ground), generates an electric field, which extracts and accelerates the  $Cs^+$  ions. An impact ion energy of 570 eV on the specimen surface was utilized throughout the experiments, in order to keep atomic mixing, due to the collision cascade, sufficiently low and achieve a depth resolution at the nm level. The secondary ions emitted from the specimen surface under irradiation with the primary beam are analyzed by means of a magnetic sector. The principle of work of such a mass analyzer is quite simple. Ions are extracted from the sample using a high extraction potential (~ 4 keV). Upon traversing a magnetic field, the charged particles experience a field force in a direction orthogonal to the direction of the magnetic flux and their original axis of travel, and thus adopt a circular path with radius directly related to their velocity. Since all ions are accelerated to a fixed potential before getting into the magnetic field, they can be separated according to their masses. The radius of curvature  $R$  for an ion of mass-to-charge ratio  $m/q$ , having been accelerated by a potential  $V$  and travelling through a magnetic field  $B$ , is given by  $R = B^{-1}(2mV/q)^{1/2}$ . The dispersion of adjacent masses, that is to say, the mass resolution, is proportional to the radius of the magnets used and degrades with increasing mass. In average, mass resolutions around  $10^4$  are achieved. For a detailed description of SIMS, Refs.<sup>172,173</sup> are recommended.



**Fig. 3.28: Photograph of the CAMECA IMS WF D-SIMS installed at the IHP laboratories.**

### 3.2.2.4 Scanning Electron Microscopy

The scanning electron microscope (SEM) is a type of electron microscope that images the sample surface by scanning it with a high-energy beam of electrons in a raster scan pattern. The instrument available at the IHP laboratories is a *Hitachi S-4500* operating in high vacuum (HV) (Fig. 3.29).

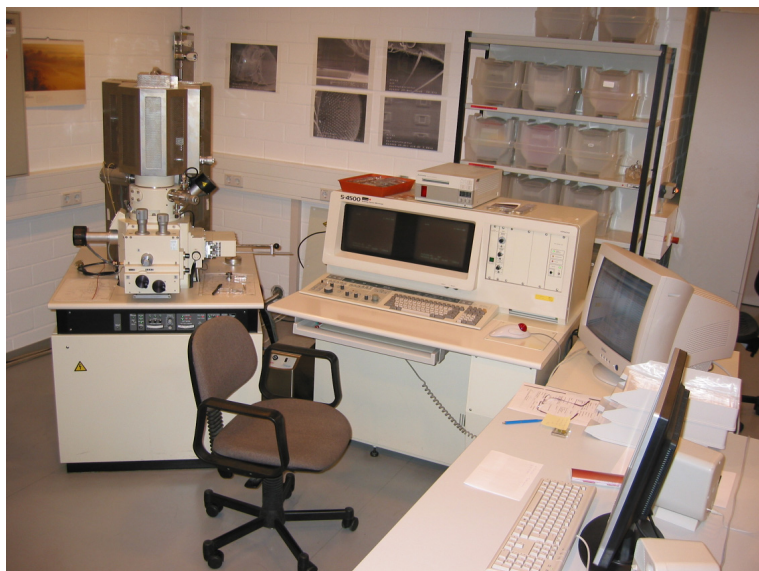


**Fig. 3.29: Photograph of the Hitachi S-4500 scanning electron microscope available at the IHP laboratories.**

In this tool, the primary electrons are generated by a *cold field emitter*, located in the upper part of the column, in a chamber pumped down to UHV by means of an ion pump. The

cathode is a tungsten wire fashioned into a sharp point of less than 100 nm in radius and supported by a tungsten hairpin. When a voltage of about 3-5 kV is applied to it, which is not heated, electrons can tunnel through the potential barrier and leave the tip. A typical cathode current density is  $10^5$  A / cm<sup>2</sup>. The emitted electrons are then conveyed onto the specimen by applying, between the tip and an anode on the way towards the sample, an accelerating voltage ranging from few hundreds of eV up to 25 keV. The beam size is determined by the optics and the beam voltage. Indeed, the higher the beam voltage, the less the electrons feel mutual repulsion along their path and therefore the narrower the beam is. The beam size determines in turn the image resolution, which is  $\sim 1.5$  nm at 15 keV with the *Hitachi S-4500*. Making use of deflector plates in the electron column, the beam can be deflected in the x and y axes so that it scans in a raster fashion over a rectangular area of the sample surface. The primary electrons lose energy by repeated random scattering and absorption within a *teardrop-shaped* volume of the specimen known as the *interaction volume*, which extends from less than 100 nm to around 5  $\mu$ m into the surface. The size of the interaction volume depends on the electron landing energy, the atomic number of the specimen and the specimen density. As a result of the electron irradiation, several phenomena occur in the sample. For instance, elastically and inelastically scattered electrons, called back-scattered electrons (BSE) and secondary electrons (SE), respectively, and x-rays are emitted from the surface and can be detected by suited detectors (Fig. 3.30).<sup>174</sup>

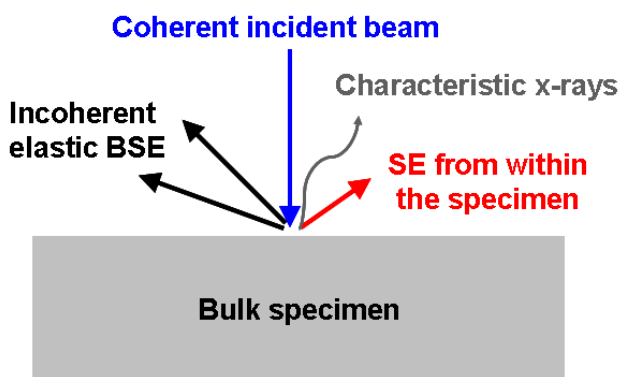


**Fig. 3.30:** Signals detected in SEM under electron irradiation of a bulk specimen. Different kinds of electrons are scattered in the back direction (angle of emission  $> 90^\circ$  with respect to the direction of the incident beam). Characteristic x-rays are also emitted. Signals not measured in SEM, like Auger electron intensities, are not sketched.

Different materials generate different SE yields and, consequently, different contrast in a SEM image. That is, for example, how the thickness of a layer stacked on top of a substrate is determined in a cross-section analysis, once the specimen has been cleaved along a high

symmetry in-plane crystallographic direction. Moreover, for a fixed material the SE yield varies also as a function of the surface morphology, so that plan or slightly tilted views of the specimen can reveal details about the presence of irregularities with size down to few nm on the surface, e.g., surface roughness, defects. Most commonly, secondary electron imaging is performed. In some cases, however, it is worth to follow the BSE, because the intensity of the BSE signal is strongly related to the atomic number ( $Z$ ) of the specimen. BSE images can hence provide the distribution of different elements in the sample. Finally, characteristic X-rays are emitted when the electron beam removes an inner shell electron from the sample, causing a higher energy electron to fill the hole and release energy. These characteristic X-rays are used to identify the composition and measure the abundance of elements in the sample down to the at % level. The technique is called energy dispersive x-ray (EDX) spectroscopy, and is integrated within the *Hitachi S-4500* instrument.

### 3.2.2.5 Transmission Electron Microscopy

For the sake of simplicity, a transmission electron microscope (TEM) can be roughly compared to a slide projector. A projector shines a beam of light through a slide: as the light passes through, it is affected by the structures and objects on the slide. This results in only certain parts of the light beam being transmitted through certain parts of the slide. The transmitted beam is projected onto the viewing screen, and an enlarged image of the slide is formed. TEM works in the same way, except that it transmits electrons through a thin specimen. The transmitted electrons are then projected onto a phosphor screen and recorded by a *charge-coupled device (CCD) camera*. The basic functions of TEM are controlled by means of magnetic lenses. The behavior of such lenses can be approximated to the action of a convex (converging) glass lens on monochromatic light (Fig. 3.31). The main difference is that, whereas glass lenses have a fixed focal length and are moved up and down in a light microscope to control light intensity, image focus and magnification, in a TEM the position of the magnetic lenses is fixed, and magnification and focus are tuned by varying the lens strength, that is to say the associated magnetic field.

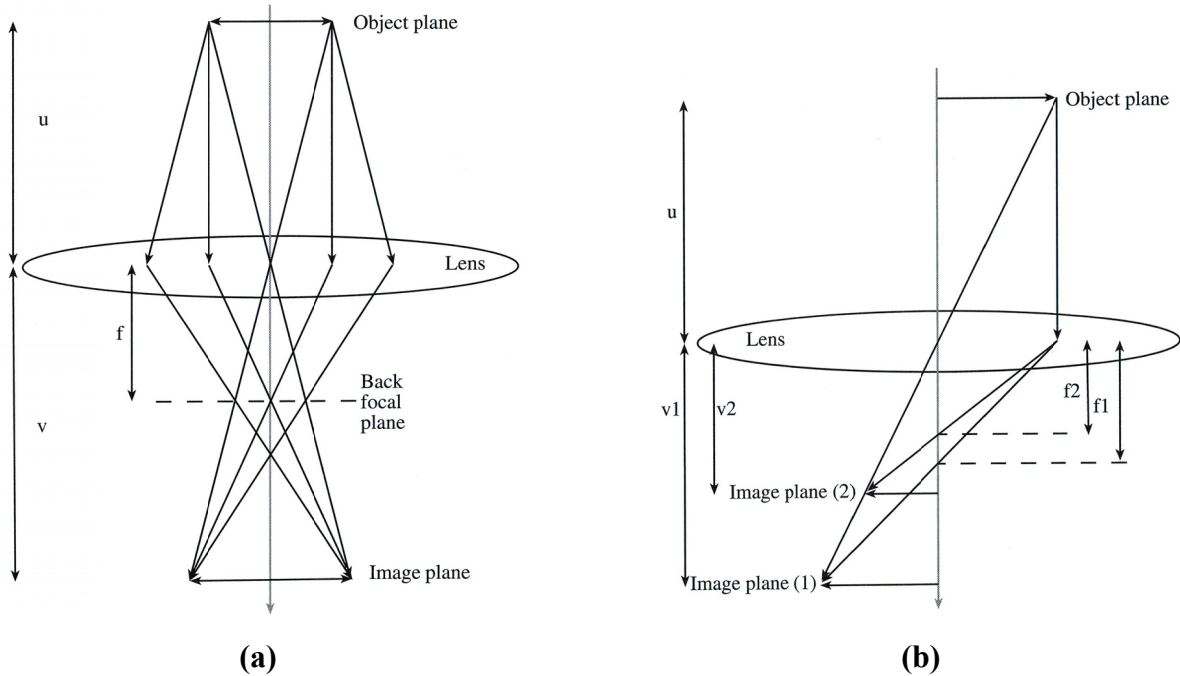


**Fig. 3.31:** (a) Ray diagram for a finite object, represented by an arrow, symmetrically positioned around the optic axis. Rays emerging from a point in the object (distance  $u$  from the lens) are collected by the lens and converged into a point in the image (distance  $v$  from the lens). Parallel rays exiting the specimen are focused on the so called *back focal plane* (distance  $f$  from the lens). (b) Strengthening the lens shortens the focal length  $f$ : a weaker lens ( $f_1$ ) produces a higher magnification  $M = v / u$  than a stronger lens ( $f_2$ ). It is noted that  $u$  does not change.<sup>175</sup>

The key elements of a TEM column are briefly introduced in this paragraph (Ref. <sup>175</sup> is suggested for a deep comprehension of the technique). From the top down, a monochromatic electron beam with energy selectable between 20 and 300 keV is produced by an electron gun. The electron stream is focused to a small, coherent beam by the use of two sequential *condenser lenses*. Afterwards, a *condenser aperture* is placed, in order to intercept and thus knock out high-angle electrons (those far away from the optical axis). The function of the condenser aperture is to reduce the spherical aberration, as electrons passing through the periphery of the lens are refracted more and therefore have different focal points than the electrons travelling along the axis. The primary beam then hits the specimen, which is thinned down to  $\sim 100$  nm by standard methods of mechanical polishing and ion milling.<sup>175,176</sup> The electrons which exit from the sample are of three types: unscattered, inelastically scattered and elastically scattered (Fig. 3.32).

The transmission of unscattered electrons, that is to say electrons which have not undergone any interaction within the crossed matter, is inversely proportional to the sample thickness. In consequence, thicker areas of the specimen will have fewer unscattered electrons, and will

appear darker, than thinner regions (a similar reasoning applies in case of density differences among the materials the specimen is made of, e.g., denser areas will transmit less unscattered electrons).

Inelastically scattered electrons are those incident electrons that have interacted with specimen atoms in an inelastic fashion, losing energy at an extent that is characteristic of the elements present in the matrix. These loss energies are unique to each bonding state of each element and thus can be used, in a technique named *electron energy loss spectroscopy* (EELS),<sup>171</sup> to extract both compositional and bonding (e.g., oxidation state) information on the specimen region being examined (it is noted that, in consequence of electron inelastic scattering, also x-rays are produced, which are characteristic of the emitting element, so that an EDX analysis can be performed also in a TEM by using a suitable detector below the sample).

Elastically scattered electrons conserve their initial energy and momentum after exiting from the specimen and are considered in the following, since they represent the major source of contrast in TEM images and create the intensity distribution in diffraction patterns whenever crystalline samples are analyzed. Indeed, a crystalline sample acts as a diffraction grating for the electrons, which behave as waves.

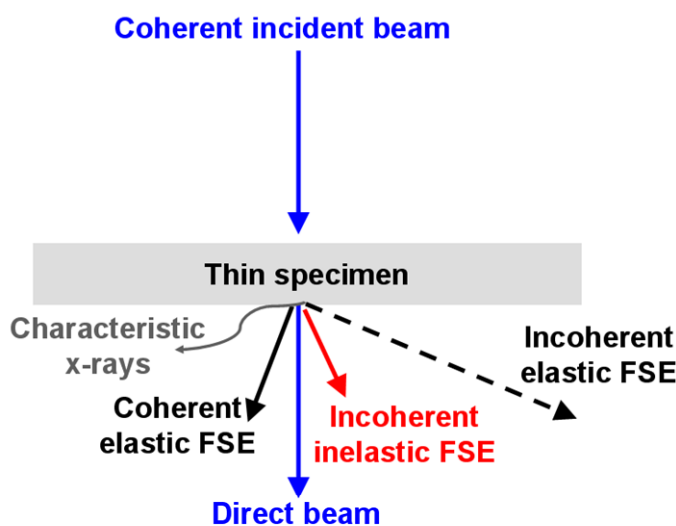


**Fig. 3.32: Signals detected in TEM under high-energy electron irradiation of a thin specimen.** Different kinds of forward scattered electrons (FSEs) are generated (angle of emission  $< 90^\circ$  with respect to the direction of the incident beam). The unscattered ones constitute the direct beam; elastically FSEs that emerge at relatively low angles ( $1\text{--}10^\circ$ ) are coherent, whereas those at higher angles ( $>\sim 10^\circ$ ) become more incoherent; inelastic scattering is almost always incoherent and relatively low angle ( $<1^\circ$ ) forward scattering. Characteristic x-rays are also emitted. Signals not measured in TEM, e. g. BSE, are not sketched. As the specimen gets thicker, less electrons are forward scattered and more are backscattered.<sup>175</sup>

Fig. 3.33 illustrates the two basic operation modes of a TEM, sketching the optics down the column between the specimen and the screen.

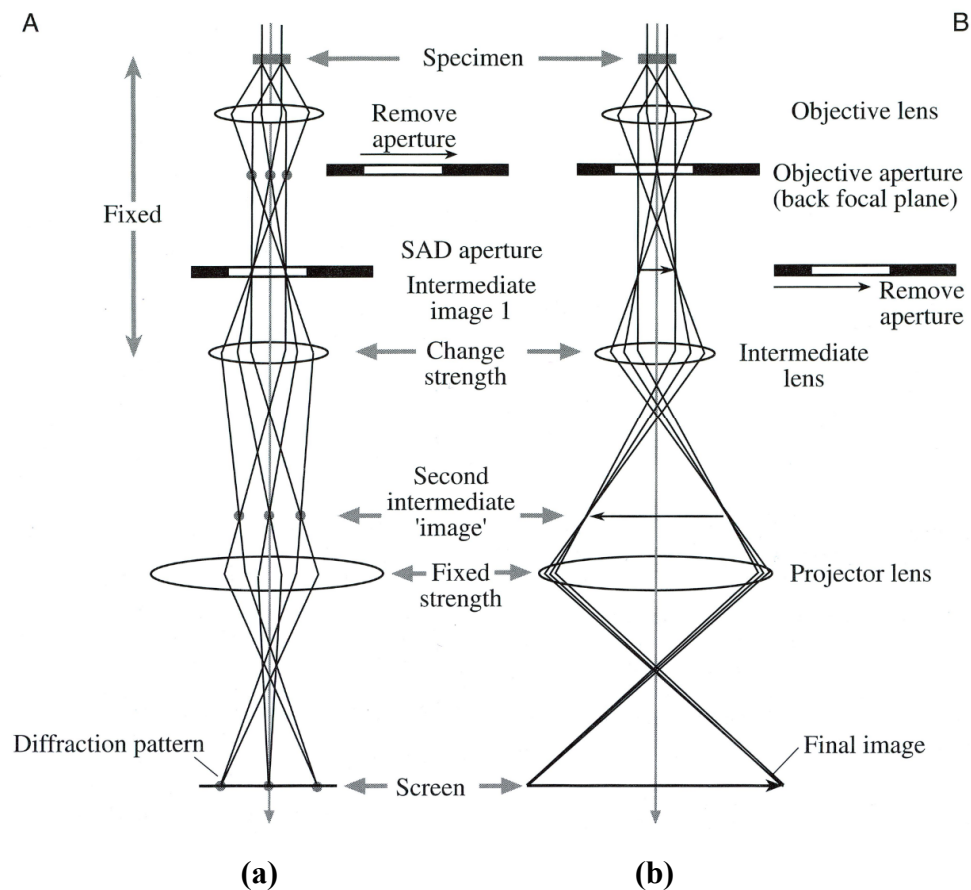


**Fig. 3.33: TEM (a) diffraction mode and (b) imaging mode. The intermediate lens selects (a) the back focal plane or (b) the image plane of the objective lens as its object.<sup>175</sup>**

The *objective lens*, which has a magnification between 20 and 100 times, gathers the electrons coming out from the specimen, disperses them to create a diffraction pattern in the back focal plane, and recombines them to form an image in the image plane (a mathematical description of the interaction between the transmitted electrons and the electromagnetic field of the TEM column can be found in Ref. <sup>177</sup>). A diffraction pattern is projected onto the screen when the strength of the next electron lens below the objective, the so called *intermediate lens*, is decreased, so that it is now focused on the back focal plane of the objective lens, as shown in Fig. 3.33(a). Since a diffraction pattern from the whole specimen is not useful (the sample is often bucked and the direct beam is often so intense that it can damage the viewing screen), the illuminated portion of the sample is reduced by inserting a *selected area diffraction* (SAD) aperture in the image plane of the objective lens. If an image of the specimen has to be obtained on the viewing screen instead of a diffraction pattern, the intermediate lens is adjusted so that its object plane is the image plane of the objective lens (Fig. 3.33(b)). Another

important optical component in Fig. 3.33(b) is the *objective aperture*, inserted into the back focal plane of the objective lens. Indeed, moving the objective aperture as schematized in Fig. 3.34, either the unscattered electrons, which get transmitted through the specimen maintaining their original trajectory along the optic axis, or some of the scattered electrons can be selected to create the image. The former imaging mode is called *bright-field* and the latter one *dark-field*. The combination of all the lenses beneath the specimen makes magnification factors up to 1 million times possible in the most evolved TEMs.

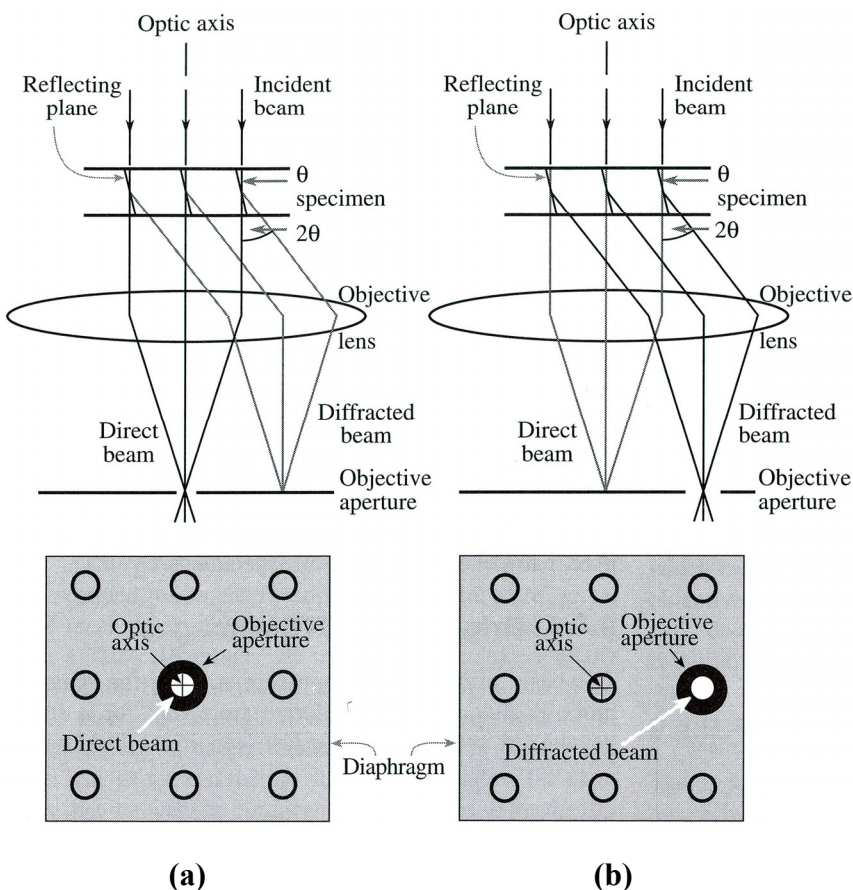


**Fig. 3.34: Ray diagrams showing how the combination objective lens / aperture is used to produce (a) a BF image formed from the direct beam and (b) a displaced-aperture DF image formed with a specific off-axis scattered beam. The area selected by the objective aperture, as seen on the screen, is shown below each ray diagram. Adapted from Ref. <sup>175</sup>.**

Throughout this thesis, two TEMs were employed to analyze the defect structure of the Ge(111) epilayer: a *Philips CM200* at the IHP laboratories (Fig. 3.35(a)) and a *FEI Tecnai F20 Cs-corrected* at the *Technical University of Dresden* (Fig. 3.35(b)). In both systems the electron beam source is a *Schottky field emission gun* (SFEG), which is essentially a tungsten tip coated with zirconia (to enhance thermionic emission at a fixed extraction voltage), run at high temperature ( $\sim 1800$  K) in UHV. A Schottky emitter combines the high brightness and

low energy spread of the cold field emitter with the high stability and low beam noise of the thermal emitters. Then, down the column, HV is sufficient. Point resolution at 200 kV, maximum applicable voltage, is  $\sim 0.27$  nm for the *Philips CM200* and  $\sim 0.11$  nm for the *FEI Tecnai F20 Cs-corrected*, owing to the presence of an hexapole corrector system, constructed for compensating aberrations of the objective lens.<sup>178,179</sup>

Finally, an illuminating tutorial about the basics of TEM, available at Ref. <sup>180</sup>, is suggested to get acquainted with TEM optics in an interactive way.



**Fig. 3.35:** (a) The *Philips CM200* TEM at IHP; (b) the *FEI Tecnai F20 Cs-corrected* TEM at the Technical University of Dresden (courtesy of Dr. D. Geiger).

Original publication: J. Appl. Phys. **103**, 084110 (2008)

available at <http://dx.doi.org/10.1063/1.2870270>

## 4 The influence of lattice oxygen on the initial growth behaviour of heteroepitaxial Ge layers on single crystalline PrO<sub>2</sub> (111) / Si(111) support systems

A. Giussani,<sup>1</sup> O. Seifarth,<sup>1</sup> P. Rodenbach,<sup>1</sup> H.-J. Müssig,<sup>1</sup> P. Zaumseil,<sup>1</sup> T. Weisemöller,<sup>2</sup> C. Deiter,<sup>2</sup> and J. Wollschläger,<sup>2</sup> P. Storck,<sup>3</sup> and T. Schroeder<sup>1,a)</sup>

<sup>1</sup>IHP, Im Technologiepark 25, 15236 Frankfurt (Oder), Germany

<sup>2</sup>University of Osnabrück, Barbarastrasse 7, 49076 Osnabrück, Germany

<sup>3</sup>SILTRONIC AG, Hanns-Seidel-Platz 4, 81737 München, Germany

---

<sup>a)</sup>Author to whom correspondence should be addressed. Electronic mail:  
[schroeder@ihp-microelectronics.com](mailto:schroeder@ihp-microelectronics.com)

Original publication: J. Appl. Phys. **105**, 033512 (2009)  
available at <http://dx.doi.org/10.1063/1.3068198>

## 5 Atomically smooth and single crystalline Ge(111) / cub- Pr<sub>2</sub>O<sub>3</sub>(111) / Si(111) heterostructures: structural and chemical composition study

A. Giussani,<sup>1,a)</sup> P. Rodenbach,<sup>1</sup> P. Zaumseil,<sup>1</sup> J. Dabrowski,<sup>1</sup> R. Kurps,<sup>1</sup> G. Weidner,<sup>1</sup> H.-J. Müssig,<sup>1</sup> P. Storck,<sup>2</sup> J. Wollschläger,<sup>3</sup> and T. Schroeder<sup>1</sup>

<sup>1</sup>IHP, Im Technologiepark 25, 15236 Frankfurt (Oder), Germany

<sup>2</sup>SILTRONIC AG, Hanns-Seidel-Platz 4, 81737 München, Germany

<sup>3</sup>University of Osnabrück, Barbarastrasse 7, 49076 Osnabrück, Germany

---

<sup>a)</sup>Author to whom correspondence should be addressed. Electronic mail:  
[giussani@ihp-microelectronics.com](mailto:giussani@ihp-microelectronics.com)

Original publication: J. Appl. Phys. **106**, (2009)  
available at <http://dx.doi.org/10.1063/1.3224947>

## 6 Defect Structure of Ge(111) / cubic Pr<sub>2</sub>O<sub>3</sub>(111) / Si(111) Heterostructures: Thickness and Annealing Dependence

A. Giussani,<sup>1,a)</sup> P. Zaumseil,<sup>1</sup> P. Rodenbach,<sup>1</sup> G. Weidner,<sup>1</sup> M. A. Schubert,<sup>1</sup> D. Geiger,<sup>2</sup> H. Lichte,<sup>2</sup> P. Storck,<sup>3</sup> J. Wollschläger,<sup>4</sup> and T. Schroeder<sup>1</sup>

<sup>1</sup>IHP, Im Technologiepark 25, 15236 Frankfurt (Oder), Germany

<sup>2</sup>Technical University Dresden, Zellescher Weg 16, 01062 Dresden, Germany

<sup>3</sup>SILTRONIC AG, Hanns-Seidel-Platz 4, 81737 München, Germany

<sup>4</sup>University of Osnabrück, Barbarastrasse 7, 49076 Osnabrück, Germany

---

<sup>a)</sup>Author to whom correspondence should be addressed. Electronic mail:  
[giussani@ihp-microelectronics.com](mailto:giussani@ihp-microelectronics.com)

## 7 Summary and outlook

### 7.1 Motivation

The integration of Ge on Si has been intensively pursued in the last years, in order to fulfil the increasing **demand for Ge substrates** in the most diverse fields.

In **microelectronics**, Ge is historically the material with which the first transistor was built up in 1947. However, after this discovery and up to today, it has been replaced with Si, mainly due to the superior properties of Si oxide compared to Ge oxide. Now that Si oxide has reached its physical limits and high-k dielectrics are being integrated in its place, Ge strongly returns on stage as channel material candidate in Complementary Metal Oxide Semiconductor (CMOS) devices, offering higher electron and hole mobility than Si.

In **optoelectronics**, extremely fast photodetectors can be realized at the standard Local Area Network (LAN) optical communication wavelength of 850 nm using Ge, which has an absorption length of only few hundred nm compared to the  $\sim 20 \mu\text{m}$  of Si. At the telecommunication wavelengths ( $\lambda > 1.2 \mu\text{m}$ ), silicon is even transparent and pure Ge needs to be employed to accomplish broadband photodetection.

In **photovoltaics**, the largest photo-to-electric efficiencies so far reported,  $\sim 40\%$ , have been achieved with GaInP / GaInAs / Ge multi-junction solar cells.

At the moment, **Ge wafers produced by the Czochralski pulling technique** are not available in large amounts and are too expensive to be relegated to niche applications, e.g., solar cells for satellite usage are Ge-based, whereas solar cells manufactured for terrestrial purposes are almost entirely Si-based. An answer to the lack of Ge substrates is the preparation of **high quality, single crystalline Ge thin films on the mature and cheap Si platform**. This solution is beneficial from many points of view. First of all, it meets the requirement for cost-effectiveness. The thin Ge films work as virtual substrates integrated on top of canonical Si wafers and can therefore be managed in a production line with Si-based manufacturing tools, without the need to develop specific fabrication techniques for Ge, which has a much lower tensile strength than Si and is hence more prone to damages. Secondly, once integrated on Si, Ge could in turn be utilized for the integration of III-V compound semiconductors, being Ge nearly lattice and thermal matched to GaAs. This would open the way to the long-dreamed assembly of III-V materials on Si, for the creation of high-

performance hybrid devices that combine optoelectronic and microelectronic properties on the same board.

Two main approaches for the integration of Ge on Si are under development: layer transfer and heteroepitaxy.

Following the latter, the growth of thin Ge epilayers on Si(111) substrates via single crystalline praseodymia was carried out by MBE and investigated in detail. Praseodymia is a polymorphic oxide, which, owing to the tiny lattice mismatch of only + 0.5%, grows on the pseudo-hexagonal Si(111) surface in the hex- $\text{Pr}_2\text{O}_3$  phase with (0001) orientation. Such an oxide with thickness 5-10 nm presents high crystalline quality, i.e., it has a very smooth surface and a very sharp interface with the Si(111) substrate, without any detectable interfacial oxide layer. However, it is not suitable for Ge overgrowth. The ABAB... stacking sequence of the (0001) planes in hex- $\text{Pr}_2\text{O}_3$  breaks the ABCABC stacking of the (111) planes in the Si(111) substrate, and this afterwards results in heavily twinned Ge(111) epilayers, when a prerequisite for a successful integration of Ge on Si is single crystallinity. A way out was found in the post-deposition annealing at  $\sim 400^\circ\text{C}$  of hex- $\text{Pr}_2\text{O}_3$ (0001). Depending on whether  $\text{N}_2$  or  $\text{O}_2$  is employed as gas during the thermal treatment, the as-grown buffer can be converted to type-B cub- $\text{Pr}_2\text{O}_3$ (111) or type-B  $\text{PrO}_2$ (111), respectively. Here, it is reminded that type-B defines a (111)-oriented epilayer, in which the stacking vector is rotated by  $180^\circ$  around the [111] surface normal with respect to the stacking vector in the (111)-oriented substrate (instead, the term *type-A* accounts for a stacking vector in the epilayer that is oriented in the same way as in the substrate). From a lattice point of view, cub- $\text{Pr}_2\text{O}_3$  is a better mediator between Si and Ge than  $\text{PrO}_2$ . Its unit cell is  $\sim 2.7\%$  bigger than twice the Si unit cell and  $\sim 1.4\%$  smaller than twice the Ge unit cell, whereas the  $\text{PrO}_2$  lattice is actually  $\sim 4.7\%$  smaller than Ge and therefore increases the 4.2% misfit between Si and Ge. Yet, cub- $\text{Pr}_2\text{O}_3$  has the bixbyite structure and a (2x2) coincidence lattice on Si(111), and consequently suffers from antiphase boundary defects. On the contrary,  $\text{PrO}_2$  has the fluorite structure and a (1x1) coincidence lattice on Si(111), and in this case the hex-to-cub phase transformation is theoretically expected to be free from antiphase boundaries in both the anion and the cation sub-lattice. As defects in the oxide buffer are likely to replicate in the growing Ge overlayer,  $\text{PrO}_2$  was selected as template for Ge epitaxy.

## 7.2 Results

Characterization of the Ge / praseodymia / Si(111) heterostructure was carried out on different levels. First, **the growth of thin Ge films on PrO<sub>2</sub>(111) was investigated in-situ** by means of instruments incorporated in the MBE cluster facility, namely, RHEED, XPS and UPS. Secondly, the **morphology of the Ge epifilms and their epitaxial relationship with the praseodymia / Si(111) support system** was studied by means of laboratory and synchrotron radiation-based techniques, namely SEM, XRR and XRD. Moreover, the **purity of the Ge epilayers** was analyzed by D-SIMS, which has a sensitivity of few ppb (part per billion) towards the presence of contamination. Finally, the **defect structure of the Ge epifilms** as a function of annealing and film thickness was examined by a combination of laboratory-settled TEM and XRD.

### 7.2.1 In-situ growth study of Ge thin epifilms

It turned out from the in-situ analyses that, in the initial growth stages of Ge evaporation at a substrate temperature of  $\sim 550^{\circ}\text{C}$ , the growing Ge deposit interacts with the underlying PrO<sub>2</sub> buffer, as sketched in Fig. 7.1. Lattice oxygen from PrO<sub>2</sub>, well known for its catalytic properties, diffuses towards the Ge deposit, oxidizing it to amorphous GeO<sub>2</sub>. The migration of oxygen stops once PrO<sub>2</sub> has been chemically reduced to cub-Pr<sub>2</sub>O<sub>3</sub>, which is thermodynamically stable in contact with Ge. Since Ge evaporation proceeds, and no additional oxygen is available for the interaction with Ge, the amorphous GeO<sub>2</sub> evolves into GeO, which is volatile at the deposition temperature and sublimates, uncovering the now stable cub-Pr<sub>2</sub>O<sub>3</sub> template. Such a reaction works out also as a self-cleaning mechanism, which recovers a clean Pr oxide surface for Ge heteroepitaxy after the exposure to air due to the ex-situ annealing. At this stage, Ge(111) islands have formed on the buffer surface, according to a Volmer-Weber growth mode. These islands deposited at high temperature are single crystalline and type-A oriented and therefore constitute a good seed for further Ge epitaxy. A smooth coalescence of such Ge nanoclusters occurs only when the growth temperature is lowered to  $300^{\circ}\text{C}$ .

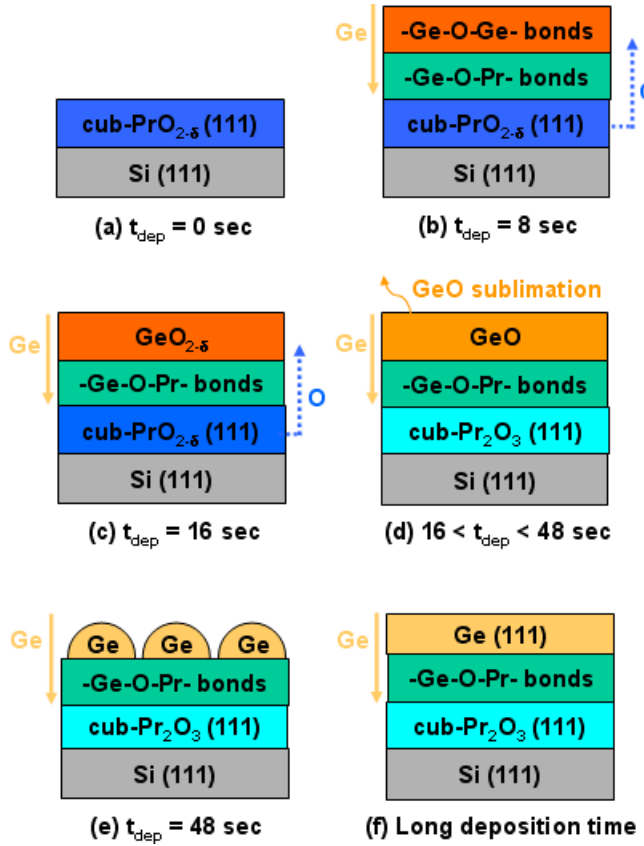


Fig. 7.1: Ge growth mechanism on  $\text{PrO}_2(111)$  /  $\text{Si}(111)$  support systems.

## 7.2.2 Morphology and structure characterization of the $\text{Ge}(111)$ epilayer

The morphology and structure study showed that atomically flat, single crystalline and type-A oriented  $\text{Ge}(111)$  epifilms with thickness in the range 20 - 1000 nm can be achieved using the above described double-step deposition recipe. The following epitaxial relationships were derived:

$$\text{Vertical} \quad \text{Ge}[111] \parallel \text{cub-}\text{Pr}_2\text{O}_3[111] \parallel \text{Si}[111]$$

$$\text{In-plane} \quad \text{Ge}<11-2> \parallel \text{cub-}\text{Pr}_2\text{O}_3<-1-12> \parallel \text{Si}<11-2>$$

The parallel and anti-parallel in-plane alignment of the Ge and cub- $\text{Pr}_2\text{O}_3$  lattices with the Si substrate azimuth, respectively, highlights the type-A / B / A stacking configuration of the  $\text{Ge}(111)$  / cub- $\text{Pr}_2\text{O}_3(111)$  /  $\text{Si}(111)$  heterostructure (Fig. 7.2).

It is noteworthy that the Ge epilayers are fully relaxed at all the investigated thicknesses, despite the very thin (5-10 nm) buffer used. This a clear advantage from a point of view of

planar integration into ICs with respect to other template systems, i.e. compositionally graded SiGe, in which the buffer thickness has to be some  $\mu\text{m}$  to get fully relaxed overlayers. The absence down to the ppb level of Si and Pr impurities inside the Ge epifilms, even after annealing at  $850^\circ\text{C}$  for 30 min in UHV, was also demonstrated. This result, which unveils that praseodymia works not only as a buffer but also as a diffusion barrier, is a key-point in view of building microelectronic or optoelectronic devices for which ultra-purity of the Ge epilayer is a must.

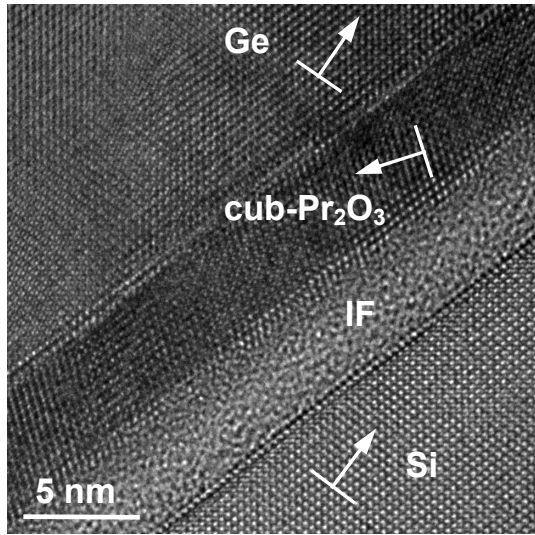


**Fig. 7.2: <1-10> TEM cross-section of the Ge(111) / cub-Pr<sub>2</sub>O<sub>3</sub>(111) / Si(111) heterostructure, highlighting the type-A / B / A stacking (arrows indicate the surface normal to the {11-1} planes).**

### 7.2.3 Defect structure of the Ge(111) epilayer

The full relaxation of the Ge epifilms is paid in terms of structural defects. The main Ge defect structure was found to be given by **rotational twins, stacking faults and microtwins**, and their dependence on Ge epilayer thickness and annealing was analyzed.

Rotational twins, that is to say, type-B oriented Ge(111) grains within the mainly type-A Ge(111) matrix, were shown to be confined to the Ge / cub-Pr<sub>2</sub>O<sub>3</sub> interface and to be partly annihilated by means of high temperature post-deposition annealing.

Defects running across {11-1} planes present a more complex scenario. Their origin was tracked to be due to the coalescence of the Ge(111) islands initially forming on the oxide surface because of the initial Volmer-Weber growth mode. When islands coalesce, stacking faults and microtwins (Fig. 7.3) are generated at the points where the islands join. Such an issue is well-known in case of 3D growth of thin epifilms, e.g., GaP and Ge on Si(001), and

$\text{ZnS}_x\text{Se}_{1-x}$  /  $\text{ZnSe}$  on  $\text{GaAs}(001)$ . It was proven that thermal treatments are effective in reducing the stacking fault density, but not the microtwin one. Yet, most microtwins do not thread up to the surface in case of layers thicker than  $\sim 300$  nm. In case of a  $\sim 1 \mu\text{m}$   $\text{Ge}(111)$  epifilm it can be clearly observed that most defects are trapped in the first 300 nm, whereas the upper part of the layer is definitely of higher structural quality. The final defect density achieved is  $\sim 10^8\text{-}10^9 \text{ cm}^{-2}$ . In conclusion, the density of all the types of defects observed in the Ge epilayers get reduced by increasing the film thickness; instead, only rotation twins and stacking faults are impacted by high temperature annealing.

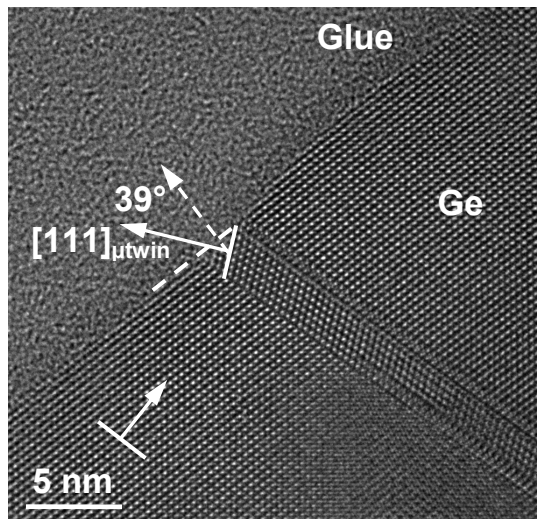


**Fig. 7.3: <1-10> TEM cross-section of a  $\mu$ twin in the  $\text{Ge}(111)$  epilayer (solid and dashed arrows indicate the  $[111]$  direction in the  $\mu$ twin and in the unflawed  $\text{Ge}(111)$  matrix, respectively).**

### 7.3 Outlook

Since the accomplished defect density is still too large to consider the  $\text{Ge}(111)$  / cub- $\text{Pr}_2\text{O}_3(111)$  /  $\text{Si}(111)$  heterostructure for device applications, hardware improvement and deposition recipe optimization are on-going.

A first progress is expected to come from the installation of an in-situ annealing chamber for the hex-to-cub phase transformation of the buffer oxide. Despite the care paid in terms of quickness of the ex-situ operations, deposition of particles, contamination, etc. are very likely to damage the oxide surface and consequently induce defects in the Ge epilayer.

Furthermore, since flaws across the  $\{11-1\}$  planes mostly originate from the Volmer-Weber growth mode of Ge, engineering of the Ge epilayer deposition on the oxide buffer from 3D to 2D since the initial stages is in progress. In the literature, it is reported that surfactant-

mediated epitaxy is a valid solution to favour layer-by-layer growth and to help reduce the film defect density. For this reason, B, Sb and H will be (separately) tested as surfactants during the evaporation of Ge on PrO<sub>2</sub>.

Finally, these “proof-of-principle” MBE studies are aimed at being transferred to mass-production deposition tools, i.e., the *Aixtron* CVD SiGe and oxide reactors in the IHP cleanroom. CVD Ge(111) epifilms with a superior structural quality compared to MBE have already been achieved on MBE-prepared PrO<sub>2</sub> epilayers on Si(111) wafers in the course of this PhD thesis. Though depositions and investigations have just started, the lower defect density of the CVD Ge epifilms seems to be attributable to the role of surfactant played by H in the CVD growth process, coming from the dissociation of the GeH<sub>4</sub> precursor and the H<sub>2</sub> carrier gas, and the possibility to grow the whole film at a high temperature of 600°C. The biggest issue at the moment is the lack of suitable precursors for the growth of Pr oxide, which is under discussion with different suppliers, and would allow for the realization of a fully CVD-grown Ge(111) / cub-Pr<sub>2</sub>O<sub>3</sub>(111) / Si(111) heterostructure.

# Scientific visibility during the PhD

## Publications in peer-reviewed journals

- 1) T. Schroeder, I. Costina, A. Giussani, G. Weidner, O. Seifarth, C. Wenger, P. Zaumseil, C. Mocuta, T. H. Metzger, D. Geiger, and H. Lichte, J. Appl. Phys. **102**, 034107 (2007)
- 2) T. Schroeder, I. Costina, P. Storck, A. Wilke, O. Seifarth, A. Giussani, H. J. Mussig, and P. Zaumseil, J. Appl. Phys. **103**, 084102 (2008)
- 3) A. Giussani, O. Seifarth, P. Rodenbach, H. J. Müssig, P. Zaumseil, T. Weisemoeller, C. Deiter, J. Wollschläger, P. Storck, and T. Schroeder, J. Appl. Phys. **103**, 084110 (2008)
- 4) T. Weisemoeller, C. Deiter, F. Bertram, S. Gevers, A. Giussani, P. Zaumseil, T. Schroeder, and J. Wollschläger, Appl. Phys. Lett. **93**, 032905 (2008)
- 5) T. Schroeder, P. Zaumseil, O. Seifarth, A. Giussani, H. J. Müssig, P. Storck, D. Geiger, H. Lichte, and J. Dabrowski, New J. Phys. **10**, 113004 (2008)
- 6) C. Borschel, C. Ronning, H. Hofsass, A. Giussani, P. Zaumseil, C. Wenger, P. Storck, and T. Schroeder, J. Vac. Sci. Technol., B **27**, 305 (2009)
- 7) A. Giussani, P. Rodenbach, P. Zaumseil, J. Dabrowski, R. Kurps, G. Weidner, H. J. Mussig, P. Storck, J. Wollschläger, and T. Schroeder, J. Appl. Phys. **105**, 033512 (2009)
- 8) T. Schroeder, A. Giussani, J. Dabrowski, P. Zaumseil, H.-J. Müssig, O. Seifarth, and P. Storck, Phys. Stat. Sol. (C) **6**, 653 (2009)
- 9) T. Schroeder, A. Giussani, H.-J. Muessig, G. Weidner, I. Costina, C. Wenger, M. Lukosius, P. Storck, and P. Zaumseil, Microelectron. Eng. **86**, 1615 (2009)
- 10) P. Zaumseil, A. Giussani, P. Rodenbach, and T. Schroeder, Phys. Status Solidi A **206**, 1809 (2009)
- 11) T. Weisemoeller, F. Bertram, S. Gevers, A. Greuling, C. Deiter, H. Tobergte, M. Neumann, J. Wollschläger, A. Giussani, and T. Schroeder, J. Appl. Phys. **105**, 124108 (2009)
- 12) A. Giussani, P. Zaumseil, P. Rodenbach, G. Weidner, M. A. Schubert, D. Geiger, H. Lichte, P. Storck, J. Wollschläger, and T. Schroeder, J. Appl. Phys. **106**, 073502 (2009)
- 13) P. Zaumseil, A. Giussani, P. Storck, and T. Schroeder, J. Phys. D: Appl. Phys. **42**, 215411 (2009)
- 14) P. Zaumseil, A. Giussani, O. Seifarth, T. Arguirov, M. A. Schubert, and T. Schroeder, Solid State Phenom. **156-158**, 467 (2010)

## Publications in conference proceedings

- 1) **A. Giussani**, C. Wenger, O. Seifarth, A. Wilke, P. Rodenbach, P. Storck, J. Dabrowski, P. Zaumseil, H.-J. Müssig, M. Lukosius, and T. Schroeder, 15<sup>th</sup> Workshop on Dielectrics in Microelectronics, Bad Saarow (Germany), 2008, p. 291
- 2) Borschel, C. Ronning, H. Hofsäss, **A. Giussani**, P. Zaumseil, C. Wenger, P. Storck, and T. Schroeder, 15<sup>th</sup> Workshop on Dielectrics in Microelectronics, Bad Saarow (Germany), 2008, p. 243
- 3) **A. Giussani**, O. Seifarth, P. Rodenbach, P. Zaumseil, G. Weidner, H.-J. Muessig, P. Storck, and T. Schroeder, ECS Transactions **16**, 287 (2008)

## Presentations at conferences and courses

- 1) Oral presentation at the *DPG Spring Meeting*, March 26-30, 2007, Regensburg (Germany)
- 2) Poster presentation at the *HASYLAB User's Meeting*, January 25, 2008, Hamburg (Germany)
- 3) Poster presentation at the *214<sup>th</sup> ECS Meeting / SiGe, Ge and Related Compounds: Materials, Processing and Devices Symposium*, October 12-17, 2008, Honolulu (Hawaii - USA)
- 4) Oral presentation at the *DPG Spring Meeting*, February 25-29, 2008, Berlin (Germany)
- 5) Oral presentation at the *PhD Symposium*, April 23-25, 2008, Szklarska Poreba (Poland)
- 6) Poster presentation at the *HSC10: Synchrotron Radiation Techniques Contribution to Nanoscience*, May 18-22, 2009, Grenoble (France)
- 7) Poster presentation at the *E-MRS Spring Meeting*, June 08-12, 2009, Strasbourg (France)
- 8) Poster presentation at the *WE-Heraeus Physics School*, August 02-08, 2009, Physikzentrum, Bad Honnef (Germany)

## Bibliography

- <sup>1</sup> E. A. Fitzgerald, Mater. Sci. Eng., B **124–125**, 8 (2005).
- <sup>2</sup> S. F. Fang, K. Adomi, S. Iyer, H. Morkoc, H. Zabel, C. Choi, and N. Otsuka, J. Appl. Phys. **68**, R31 (1990).
- <sup>3</sup> M. Myronov, Y. Shiraki, T. Mouri, and K. M. Itoh, Thin Solid Films **517**, 359 (2008).
- <sup>4</sup> C. Claeys and E. Simoen, *Germanium-based Technologies: From Materials to Devices* (Elsevier, 2007).
- <sup>5</sup> Y. Kamata, Mater. Today **11**, 30 (2008).
- <sup>6</sup> available at <http://www.esrf.eu/UsersAndScience/Experiments/StructMaterials/ID32/>.
- <sup>7</sup> D. E. Guberman, *Germanium [Advance Release], U.S. Geological Survey Minerals Yearbook 2007* (October, 2008).
- <sup>8</sup> “*Index of Refraction*”, CVI Melles Griot, available at [http://www.cvilaser.com/Common/PDFs/Index\\_of\\_Refraction.pdf](http://www.cvilaser.com/Common/PDFs/Index_of_Refraction.pdf).
- <sup>9</sup> A. Wilson, “*IR lenses maximize detector potential*”, (2005), available at [http://www.vision-systems.com/articles/article\\_display.html?id=228887](http://www.vision-systems.com/articles/article_display.html?id=228887).
- <sup>10</sup> S. M. Sze and Kwok K. NG, *Physics of Semiconductor Devices*, Third ed. (Wiley, Hoboken, New Jersey, 2007).
- <sup>11</sup> G. E. Moore, Electronics **38** (1965).
- <sup>12</sup> K. Rim, J. L. Hoyt, and J. F. Gibbons, Electron Devices, IEEE Transactions on **47**, 1406 (2000).
- <sup>13</sup> G. D. Wilk, R. M. Wallace, and J. M. Anthony, J. Appl. Phys. **89**, 5243 (2001).
- <sup>14</sup> Intel®, “*Innovation That Breaks the Performance Barrier*”, available at <http://www.intel.com/technology/architecture-silicon/45nm-core2/index.htm>.
- <sup>15</sup> R. Penning de Vries, “*Innovations in the 'More than Moore' era*”, (06/30/2009), available at <http://www.eetimes.eu/218102043>.
- <sup>16</sup> M. L. Lee, E. A. Fitzgerald, M. T. Bulsara, M. T. Currie, and A. Lochtefeld, J. Appl. Phys. **97**, 011101 (2005).
- <sup>17</sup> F. Schäffler, Semicond. Sci. Technol. **12**, 1515 (1997).
- <sup>18</sup> K. Kita, S. Suzuki, H. Nomura, T. Takahashi, T. Nishimura, and A. Toriumi, Jpn. J. Appl. Phys. **47**, 2349 (2008).
- <sup>19</sup> K. Oishi and Y. Matsuo, Thin Solid Films **274**, 133 (1996).
- <sup>20</sup> V. V. Afanas'ev and A. Stesmans, Appl. Phys. Lett. **84**, 2319 (2004).

- <sup>21</sup> N. Wu, Q. Zhang, C. Zhu, D. S. H. Chan, A. Du, N. Balasubramanian, M. F. Li, A. Chin, J. K. O. Sin, and D.-L. Kwong, IEEE Electron Device Lett. **25**, 631 (2004).
- <sup>22</sup> A. Dimoulas, G. Mavrou, G. Vellianitis, E. Evangelou, N. Boukos, M. Houssa, and M. Caymax, Appl. Phys. Lett. **86**, 032908 (2005).
- <sup>23</sup> M. Houssa, G. Pourtois, F. Bellenger, M. Caymax, M. Meuris, and M. Heyns, ECS Transactions **11**, 471 (2007).
- <sup>24</sup> K. Kita, K. Kyuno, and A. Toriumi, Appl. Phys. Lett. **85**, 52 (2004).
- <sup>25</sup> W. C. Lee, B. H. Chin, L. K. Chu, T. D. Lin, Y. J. Lee, L. T. Tung, C. H. Lee, M. Hong, and J. Kwo, J. Cryst. Growth **311**, 2187 (2009).
- <sup>26</sup> L. K. Chu, W. C. Lee, M. L. Huang, Y. H. Chang, L. T. Tung, C. C. Chang, Y. J. Lee, J. Kwo, and M. Hong, J. Cryst. Growth **311**, 2195 (2009).
- <sup>27</sup> D. P. Bruno, B. De Jaeger, G. Eneman, A. Satta, V. Terzieva, L. Souriau, F. E. Leys, G. Pourtois, M. Houssa, K. Opsomer, G. Nicholas, M. Meuris, and M. Heyns, ECS Transactions **11**, 479 (2007).
- <sup>28</sup> G. Masini, L. Colace, and G. Assanto, Mater. Sci. Eng., B **89**, 2 (2002).
- <sup>29</sup> S. J. Koester, J. D. Schaub, G. Dehlinger, and J. O. Chu, IEEE Journal of Selected Topics in Quantum Electronics **12**, 1489 (2006).
- <sup>30</sup> G. Dehlinger, S. J. Koester, J. D. Schaub, J. O. Chu, Q. C. Ouyang, and A. Grill, Photonics Technology Letters, IEEE **16**, 2547 (2004).
- <sup>31</sup> G. K. Celler and S. Cristoloveanu, J. Appl. Phys. **93**, 4955 (2003).
- <sup>32</sup> H. H. Silvestri, H. Bracht, J. Lundsgaard Hansen, A. Nylandsted Larsen, and E. E. Haller, Semicond. Sci. Technol. **21**, 758 (2006).
- <sup>33</sup> J. Liu, J. Michel, W. Giziewicz, D. Pan, K. Wada, D. D. Cannon, S. Jongthammanurak, D. T. Danielson, L. C. Kimerling, J. Chen, F. O. Ilday, F. X. Kartner, and J. Yasaitis, Appl. Phys. Lett. **87**, 103501 (2005).
- <sup>34</sup> T. H. Loh, H. S. Nguyen, R. Murthy, M. B. Yu, W. Y. Loh, G. Q. Lo, N. Balasubramanian, D. L. Kwong, J. Wang, and S. J. Lee, Appl. Phys. Lett. **91**, 073503 (2007).
- <sup>35</sup> M. Oehme, J. Werner, E. Kasper, S. Klinger, and M. Berroth, Appl. Phys. Lett. **91**, 051108 (2007).
- <sup>36</sup> H. Tanoto, S. F. Yoon, W. K. Loke, E. A. Fitzgerald, C. Dohrman, B. Narayanan, M. T. Doan, and C. H. Tung, J. Vac. Sci. Technol., B **24**, 152 (2006).
- <sup>37</sup> “Energy Information Administration, International Energy Annual 2004”, (2006), available at <http://www.eia.doe.gov/iea/overview.html>.
- <sup>38</sup> S. Kurtz, D. Friedman, J. Geisz, and W. McMahon, J. Cryst. Growth **298**, 748 (2007).
- <sup>39</sup> W. Shockley and H. J. Queisser, J. Appl. Phys. **32**, 510 (1961).

- <sup>40</sup> F. Dimroth and S. Kurtz, MRS Bull. **32**, 230 (2007).
- <sup>41</sup> R. R. King, D. C. Law, K. M. Edmondson, C. M. Fetzer, G. S. Kinsey, H. Yoon, R. A. Sherif, and N. H. Karam, Appl. Phys. Lett. **90**, 183516 (2007).
- <sup>42</sup> S. E. Shaheen, D. S. Ginley, and G. E. Jabbour, MRS Bull. **30** (2005).
- <sup>43</sup> D. Rakwal and E. Bamberg, J. Mater. Process. Technol. **209**, 3740 (2009).
- <sup>44</sup> M. Yamaguchi, Sol. Energy Mater. Sol. Cells **75**, 261 (2003).
- <sup>45</sup> W. C. Dash, J. Appl. Phys. **29**, 736 (1958).
- <sup>46</sup> W. C. Dash, J. Appl. Phys. **30**, 459 (1959).
- <sup>47</sup> B. Depuydt, A. Theuwis, and I. Romandic, Mater. Sci. Semicond. Process. **9**, 437 (2006).
- <sup>48</sup> E. Bamberg and D. Rakwal, J. Mater. Process. Technol. **197**, 419 (2008).
- <sup>49</sup> R. Parker, “*Slicing Method Cuts Cost of Germanium Solar Cells*”, (2008), available at <http://www.futurepundit.com/archives/005544.html>.
- <sup>50</sup> A. Sakai and T. Tatsumi, Appl. Phys. Lett. **64**, 52 (1994).
- <sup>51</sup> L. Colace, G. Masini, F. Galluzzi, G. Assanto, G. Capellini, L. Di Gaspare, E. Palange, and F. Evangelisti, Appl. Phys. Lett. **72**, 3175 (1998).
- <sup>52</sup> D. J. Eaglesham and M. Cerullo, Phys. Rev. Lett. **64**, 1943 (1990).
- <sup>53</sup> M. Diani, D. Aubel, J. L. Bischoff, L. Kubler, and D. Bolmont, Surf. Sci. **291**, 110 (1993).
- <sup>54</sup> B. Cunningham, J. O. Chu, and S. Akbar, Appl. Phys. Lett. **59**, 3574 (1991).
- <sup>55</sup> V. Alberts, J. H. Neethling, and J. S. Vermaak, J. Mater. Sci. - Mater. Electron. **3**, 240 (1992).
- <sup>56</sup> J. M. Hartmann, A. M. Papon, V. Destefanis, and T. Billon, J. Cryst. Growth **310**, 5287 (2008).
- <sup>57</sup> D. Choi, Y. Ge, J. S. Harris, J. Cagnon, and S. Stemmer, J. Cryst. Growth **310**, 4273 (2008).
- <sup>58</sup> H.-C. Luan, D. R. Lim, K. K. Lee, K. M. Chen, J. G. Sandland, K. Wada, and L. C. Kimerling, Appl. Phys. Lett. **75**, 2909 (1999).
- <sup>59</sup> J. M. Hartmann, A. Abbadie, A. M. Papon, P. Holliger, G. Rolland, T. Billon, J. M. Fedeli, M. Rouviere, L. Vivien, and S. Laval, J. Appl. Phys. **95**, 5905 (2004).
- <sup>60</sup> E. A. Fitzgerald, M. T. Currie, S. B. Samavedam, T. A. Langdo, G. Taraschi, V. Yang, C. W. Leitz, and M. T. Bulsara, Phys. Stat. Sol. (A) **171**, 227 (1999).
- <sup>61</sup> S. B. Samavedam and E. A. Fitzgerald, J. Appl. Phys. **81**, 3108 (1997).

- <sup>62</sup> M. T. Currie, S. B. Samavedam, T. A. Langdo, C. W. Leitz, and E. A. Fitzgerald, *Appl. Phys. Lett.* **72**, 1718 (1998).
- <sup>63</sup> J. S. Park, J. Bai, M. Curtin, B. Adekore, M. Carroll, and A. Lochtefeld, *Appl. Phys. Lett.* **90**, 052113 (2007).
- <sup>64</sup> Z. R. Zytkiewicz, *Thin Solid Films* **412**, 64 (2002).
- <sup>65</sup> J. S. Park, M. Curtin, J. M. Hydrick, J. Bai, J. T. Li, Z. Cheng, M. Carroll, J. G. Fiorenza, and A. Lochtefeld, *Electrochem. Solid-State Lett.* **12**, H142 (2009).
- <sup>66</sup> M. Bruel, *Electron. Lett.* **31**, 1201 (1995).
- <sup>67</sup> K. Prabhakaran, F. Maeda, Y. Watanabe, and T. Ogino, *Appl. Phys. Lett.* **76**, 2244 (2000).
- <sup>68</sup> L. Clavelier, C. L. Royer, Y. Morand, C. Deguet, B. Vincent, J.-F. Damlencourt, J.-M. Hartmann, O. Kermarrec, T. Signamarcheix, B. Depuydt, A. Theuwis, C. Quaeyhaegens, N. Cherkashin, P. Rivallin, C. Tabone, S. Lagrasta, Y. Campidelli, S. Descombes, L. Sanchez, T. Akastu, A. Rigny, D. Bensahel, T. Billon, N. Kernevez, and S. Deleonibus, *ECS Transactions* **3**, 789 (2006).
- <sup>69</sup> J. M. Zahler, C.-G. Ahn, S. Zaghi, H. A. Atwater, C. Chu, and P. Iles, *Thin Solid Films* **403-404**, 558 (2002).
- <sup>70</sup> T. Tezuka, N. Sugiyama, and S. Takagi, *Appl. Phys. Lett.* **79**, 1798 (2001).
- <sup>71</sup> P. E. Hellberg, S. L. Zhang, F. M. d'Heurle, and C. S. Petersson, *J. Appl. Phys.* **82**, 5779 (1997).
- <sup>72</sup> S. Nakaharai, T. Tezuka, N. Hirashita, E. Toyoda, Y. Moriyama, N. Sugiyama, and S. Takagi, *J. Appl. Phys.* **105**, 024515 (2009).
- <sup>73</sup> G. Taraschi, A. J. Pitera, and E. A. Fitzgerald, *Solid-State Electron.* **48**, 1297 (2004).
- <sup>74</sup> T. Tezuka, N. Sugiyama, S. Takagi, and T. Kawakubo, *Appl. Phys. Lett.* **80**, 3560 (2002).
- <sup>75</sup> S. Nakaharai, T. Tezuka, N. Sugiyama, Y. Moriyama, and S.-i. Takagi, *Appl. Phys. Lett.* **83**, 3516 (2003).
- <sup>76</sup> J. W. Seo, C. Dieker, A. Tapponnier, C. Marchiori, M. Sousa, J.-P. Locquet, J. Pompeyrine, A. Ispas, C. Rossel, Y. Panayiotatos, A. Sotiropoulos, and A. Dimoulas, *Microelectron. Eng.* **84**, 2328 (2007).
- <sup>77</sup> N. A. Bojarczuk, M. Copel, S. Guha, V. Narayanan, E. J. Preisler, F. M. Ross, and H. Shang, *Appl. Phys. Lett.* **83**, 5443 (2003).
- <sup>78</sup> S. G. Thomas, E. S. Johnson, C. Tracy, P. Maniar, L. Xiuling, B. Roof, Q. Hartmann, and D. A. Ahmari, *Electron Device Letters, IEEE* **26**, 438 (2005).
- <sup>79</sup> S. J. Koester, J. D. Schaub, G. Dehlinger, and J. O. Chu, *Selected Topics in Quantum Electronics, IEEE Journal of* **12**, 1489 (2006).
- <sup>80</sup> S. Chakrabarti, "Towards III-Vs on GoP", (2007), available at <http://www.specknet.org/publications/6thWorkshop2007/ColinStanley.pdf>.

- <sup>81</sup> T. Schroeder, A. Giussani, J. Dabrowski, P. Zaumseil, H.-J. Müssig, O. Seifarth, and P. Storck, *Phys. Stat. Sol. (C)* **6**, 653 (2009).
- <sup>82</sup> Y. H. Lo, *Appl. Phys. Lett.* **59**, 2311 (1991).
- <sup>83</sup> G. Saint-Girons, C. Priester, P. Regreny, G. Patriarche, L. Largeau, V. Favre-Nicolin, G. Xu, Y. Robach, M. Gendry, and G. Hollinger, *Appl. Phys. Lett.* **92**, 241907 (2008).
- <sup>84</sup> F. Niu, B. H. Hoerman, and B. W. Wessels, *Appl. Surf. Sci.* **161**, 74 (2000).
- <sup>85</sup> J. Cheng, X. Meng, P. Yang, and J. Chu, *J. Cryst. Growth* **194**, 89 (1998).
- <sup>86</sup> P. A. Stampe and R. J. Kennedy, *Thin Solid Films* **326**, 63 (1998).
- <sup>87</sup> C.-S. Lee, S.-W. Chung, Y.-C. Kim, I.-S. Chung, D.-M. Wee, and W.-J. Lee, *Surf. Coat. Technol.* **90**, 229 (1997).
- <sup>88</sup> S. Ohmi, K. Tsutsui, and S. Furukawa, *Jpn. J. Appl. Phys.* **33**, 1121 (1994).
- <sup>89</sup> T. Asano and H. Ishiwara, *J. Appl. Phys.* **55**, 3566 (1984).
- <sup>90</sup> R. W. Fathauer and L. J. Schowalter, *Appl. Phys. Lett.* **45**, 519 (1984).
- <sup>91</sup> L. J. Schowalter, R. W. Fathauer, R. P. Goehner, L. G. Turner, R. W. DeBlois, S. Hashimoto, J.-L. Peng, W. M. Gibson, and J. P. Krusius, *J. Appl. Phys.* **58**, 302 (1985).
- <sup>92</sup> R. W. Fathauer, N. Lewis, E. L. Hall, and L. J. Schowalter, *J. Appl. Phys.* **60**, 3886 (1986).
- <sup>93</sup> H. Mizukami, K. Tsutsui, and S. Furukawa, *Jpn. J. Appl. Phys.* **30**, 3349 (1991).
- <sup>94</sup> N. S. Sokolov, J. C. Alvarez, Y. V. Shusterman, N. L. Yakovlev, R. M. Overney, Y. Itoh, I. Takahashi, and J. Harada, *Appl. Surf. Sci.* **104-105**, 402 (1996).
- <sup>95</sup> C. R. Wang, B. H. Müller, and K. R. Hofmann, *Thin Solid Films* **410**, 72 (2002).
- <sup>96</sup> C. R. Wang, M. Bierkandt, S. Paprotta, T. Wietler, and K. R. Hofmann, *Appl. Phys. Lett.* **86**, 033111 (2005).
- <sup>97</sup> J. Wollschläger, C. Deiter, M. Bierkandt, A. Gerdes, M. Bäumer, C. R. Wang, B. H. Müller, and K. R. Hofmann, *Surf. Sci.* **600**, 3637 (2006).
- <sup>98</sup> E. P. Rugeramigabo, C. Deiter, and J. Wollschläger, *Appl. Surf. Sci.* (2007).
- <sup>99</sup> T. Inoue, M. Osonoe, H. Tohda, M. Hiramatsu, Y. Yamamoto, A. Yamanaka, and T. Nakayama, *J. Appl. Phys.* **69** (1991).
- <sup>100</sup> D. O. Klenov, L. F. Edge, D. G. Schlom, and S. Stemmer, *Appl. Phys. Lett.* **86**, 051901 (2005).
- <sup>101</sup> T. Weisemoeller, C. Deiter, F. Bertram, S. Gevers, A. Giussani, P. Zaumseil, T. Schroeder, and J. Wollschlager, *Appl. Phys. Lett.* **93**, 032905 (2008).
- <sup>102</sup> T. Weisemoeller, F. Bertram, S. Gevers, A. Greuling, C. Deiter, H. Tobergte, M. Neumann, J. Wollschlager, A. Giussani, and T. Schroeder, *J. Appl. Phys.* **105**, 124108 (2009).

- <sup>103</sup> A. Schaefer, V. Zielasek, T. Schmidt, A. Sandell, M. Schowalter, O. Seifarth, L. E. Walle, C. Schulz, J. Wollschlager, T. Schroeder, A. Rosenauer, J. Falta, and M. Baumer, Phys. Rev. B **80**, 045414 (2009).
- <sup>104</sup> G.-y. Adachi and N. Imanaka, Chem. Rev. **98**, 1479 (1998).
- <sup>105</sup> H. Fukumoto, T. Imura, and Y. Osaka, Appl. Phys. Lett. **55**, 360 (1989).
- <sup>106</sup> H. B. Kim, M. H. Cho, S. W. Whangbo, C. N. Whang, S. C. Choi, W. K. Choi, J. H. Song, and S. O. Kim, Nucl. Instrum. Methods Phys. Res., Sect. B **142**, 393 (1998).
- <sup>107</sup> M. E. Hunter, M. J. Reed, N. A. El-Masry, J. C. Roberts, and S. M. Bedair, Appl. Phys. Lett. **76**, 1935 (2000).
- <sup>108</sup> J. Kwo, M. Hong, A. R. Kortan, K. T. Queeney, Y. J. Chabal, J. P. Mannaerts, T. Boone, J. J. Krajewski, A. M. Sergent, and J. M. Rosamilia, Appl. Phys. Lett. **77**, 130 (2000).
- <sup>109</sup> M. H. Cho, D. H. Ko, J. G. Seo, S. W. Whangbo, K. Jeong, I. W. Lyo, C. N. Whang, D. Y. Noh, and H. J. Kim, Thin Solid Films **382**, 288 (2001).
- <sup>110</sup> J. Kwo, M. Hong, A. R. Kortan, K. L. Queeney, Y. J. Chabal, R. L. Opila, D. A. Muller Jr., S. N. G. Chu, B. J. Sapjeta, T. S. Lay, J. P. Mannaerts, T. Boone, H. W. Krautter, J. J. Krajewski, A. M. Sergnt, and J. M. Rosamilia, J. Appl. Phys. **89**, 3920 (2001).
- <sup>111</sup> G. Mavrou, G. Vellianitis, G. Apostolopoulos, K. Argyropoulos, A. Dimoulas, and R. Scholz, Mater. Sci. Eng., B **109**, 39 (2004).
- <sup>112</sup> C. Borschel, C. Ronning, H. Hofmann, A. Giussani, P. Zaumseil, C. Wenger, P. Storck, and T. Schroeder, J. Vac. Sci. Technol., B **27**, 305 (2009).
- <sup>113</sup> E. J. Tarsa and J. S. Speck, Appl. Phys. Lett. **63**, 539 (1993).
- <sup>114</sup> J. P. Liu, P. Zaumseil, E. Bugiel, and H. J. Osten, Appl. Phys. Lett. **79**, 671 (2001).
- <sup>115</sup> T. Schroeder, T. L. Lee, J. Zegenhagen, C. Wenger, P. Zaumseil, and H. J. Müssig, Appl. Phys. Lett. **85**, 1229 (2004).
- <sup>116</sup> T. Schroeder, T.-L. Lee, L. Libralesso, I. Joumard, J. Zegenhagen, P. Zaumseil, C. Wenger, G. Lupina, G. Lippert, J. Dabrowski, and H.-J. Müssig, J. Appl. Phys. **97**, 074906 (2005).
- <sup>117</sup> X. Guo, W. Braun, B. Jenichen, V. M. Kaganer, B. P. Tinkham, A. Trampert, and K. H. Ploog, J. Appl. Phys. **100**, 023536 (2006).
- <sup>118</sup> X. Guo, W. Braun, B. Jenichen, and K. H. Ploog, J. Cryst. Growth **290**, 73 (2006).
- <sup>119</sup> T. Schroeder, P. Zaumseil, G. Weidner, C. Wenger, J. Dabrowski, and H.-J. Müssig, J. Appl. Phys. **99**, 014101 (2006).
- <sup>120</sup> L. Libralesso, T. L. Lee, and J. Zegenhagen, Appl. Phys. Lett. **90**, 222905 (2007).
- <sup>121</sup> N. M. Jeutter, W. Moritz, A. Sidorenko, and A. Stierle, Appl. Phys. Lett. **90**, 062906 (2007).

- <sup>122</sup> T. Watahiki, B. P. Tinkham, B. Jenichen, W. Braun, and K. H. Ploog, *J. Cryst. Growth* **301-302**, 381 (2007).
- <sup>123</sup> S. Chen, Y. Y. Zhu, R. Xu, Y. Q. Wu, X. J. Yang, Y. L. Fan, F. Lu, Z. M. Jiang, and J. Zou, *Appl. Phys. Lett.* **88**, 222902 (2006).
- <sup>124</sup> C. P. Chen, M. Hong, J. Kwo, H. M. Cheng, Y. L. Huang, S. Y. Lin, J. Chi, H. Y. Lee, Y. F. Hsieh, and J. P. Mannaerts, *J. Cryst. Growth* **278**, 638 (2005).
- <sup>125</sup> T. Watahiki, B. Jenichen, R. Shayduk, B. P. Tinkham, W. Braun, and H. Riechert, *J. Cryst. Growth* **311**, 2179 (2009).
- <sup>126</sup> J. X. Wang, A. Laha, A. Fissel, D. Schwendt, R. Dargis, T. Watahiki, R. Shayduk, W. Braun, T. M. Liu, and H. J. Osten, *Semicond. Sci. Technol.* **24**, 045021 (2009).
- <sup>127</sup> M. Czernohorsky, D. Tetzlaff, E. Bugiel, R. Dargis, H. J. Osten, H. D. B. Gottlob, M. Schmidt, M. C. Lemme, and H. Kurz, *Semicond. Sci. Technol.* **23**, 035010 (2008).
- <sup>128</sup> R. A. McKee, F. J. Walker, and M. F. Chisholm, *Phys. Rev. Lett.* **81**, 3014 (1998).
- <sup>129</sup> K. Eisenbeiser, J. M. Finder, Z. Yu, J. Ramdani, J. A. Curless, J. A. Hallmark, R. Droopad, W. J. Ooms, L. Salem, S. Bradshaw, and C. D. Overgaard, *Appl. Phys. Lett.* **76**, 1324 (2000).
- <sup>130</sup> C. J. Forst, C. R. Ashman, K. Schwarz, and P. E. Blochl, *Nature* **427**, 53 (2004).
- <sup>131</sup> J. W. Seo, J. Fompeyrine, A. Guiller, G. Norga, C. Marchiori, H. Siegwart, and J. P. Locquet, *Appl. Phys. Lett.* **83**, 5211 (2003).
- <sup>132</sup> K. Egami, M. Mikami, and H. Tsuya, *Appl. Phys. Lett.* **43**, 757 (1983).
- <sup>133</sup> M. Ihara, Y. Arimoto, M. Jifuku, T. Kimura, S. Kodama, H. Yamawaki, and T. Yamaoka, *J. Electrochem. Soc.* **129**, 2569 (1982).
- <sup>134</sup> C. Merckling, M. El-Kazzi, G. Delhaye, M. Gendry, G. Saint-Girons, G. Hollinger, L. Largeau, and G. Patriarche, *Appl. Phys. Lett.* **89**, 232907 (2006).
- <sup>135</sup> C. Merckling, M. El-Kazzi, V. Favre-Nicolin, M. Gendry, Y. Robach, G. Grenet, and G. Hollinger, *Thin Solid Films* **515**, 6479 (2007).
- <sup>136</sup> C. Merckling, M. El-Kazzi, G. Saint-Girons, G. Hollinger, L. Largeau, G. Patriarche, V. Favre-Nicolin, and O. Marty, *J. Appl. Phys.* **102**, 024101 (2007).
- <sup>137</sup> L. Eyring and B. Holmberg, *Adv. Chem. Ser.* **39**, 4657 (1961).
- <sup>138</sup> L. Eyring and N. C. Baenziger, *J. Appl. Phys.* **33**, 428 (1962).
- <sup>139</sup> J. Zhang, R. B. Von Dreele, and L. Eyring, *J. Solid State Chem.* **122**, 53 (1996).
- <sup>140</sup> Z. C. Kang and L. Eyring, *J. Alloys Compd.* **408-412**, 1123 (2006).
- <sup>141</sup> B. D. Cullity, *Elements of x-ray diffraction*, Addison-Wesley Series in Metallurgy and Materials (Addison-Wesley, Massachusetts, USA, 1967, 3<sup>rd</sup> printing).

- <sup>142</sup> T. Schroeder, P. Zaumseil, G. Weidner, G. Lupina, C. Wenger, and H.-J. Müssig, *J. Appl. Phys.* **98**, 123513 (2005).
- <sup>143</sup> C. C. Cho, H. Y. Liu, B. E. Gnade, T. S. Kim, and Y. Nishioka, *J. Vac. Sci. Technol., A* **10**, 769 (1992).
- <sup>144</sup> T. Asano and H. Ishiwara, *Appl. Phys. Lett.* **42**, 517 (1983).
- <sup>145</sup> T. Schroeder, P. Zaumseil, O. Seifarth, A. Giussani, H. J. Müssig, P. Storck, D. Geiger, H. Lichte, and J. Dabrowski, *New J. Phys.* **10**, 113004 (2008).
- <sup>146</sup> D. Hull and D. J. Bacon, *Introduction to dislocations*, International series on materials science and technology, 3rd ed. (Pergamon, Oxford, 1984).
- <sup>147</sup> T. Weisemoeller, PhD Thesis, University of Osnabrück, Osnabrück, 2009, available at [http://nbn-resolving.de/urn:nbn:de:hbz:5:1-100000000000000000](#)
- <sup>148</sup> T. Weisemoeller, F. Bertram, S. Gevers, C. Deiter, A. Greuling, and J. Wollschlager, *Phys. Rev. B* **79**, 245422 (2009).
- <sup>149</sup> D. T. Margulies, F. T. Parker, M. L. Rudee, F. E. Spada, J. N. Chapman, P. R. Aitchison, and A. E. Berkowitz, *Phys. Rev. Lett.* **79**, 5162 (1997).
- <sup>150</sup> H. Tabata, E. Ishii, and H. Okuda, *J. Cryst. Growth* **52**, 956 (1981).
- <sup>151</sup> I. V. Markov, *Crystal Growth for Beginners: fundamentals of nucleation, crystal growth, and epitaxy*, 2nd ed. (World Scientific Publishing Co. Pte. Ltd., 2003).
- <sup>152</sup> W. Kern, *Handbook of Semiconductor Wafer Cleaning Technology* (Noyes Publications Park Ridge NJ, 1993).
- <sup>153</sup> B. E. Warren, *X-Ray Diffraction* (Dover Publications, Inc., New York, 1990).
- <sup>154</sup> M. Birkholz, *Thin Film Analysis by X-Ray Scattering* (Wiley VCH Verlag GmbH, Weinheim, 2006).
- <sup>155</sup> J. Als-Nielsen and D. McMorrow, *Elements of Modern X-Ray Physics* (Wiley, West Sussex, 2001).
- <sup>156</sup> A. Krolzig, G. Materlik, and J. Zegenhagen, *Nucl. Instrum. Methods* **208**, 613 (1983).
- <sup>157</sup> C. Mocuta, J. Stangl, K. Mundboth, T. H. Metzger, G. Bauer, I. A. Vartanyants, M. Schmidbauer, and T. Boeck, *Phys. Rev. B* **77**, 245425 (2008).
- <sup>158</sup> A. V. Zozulya, O. M. Yefanov, I. A. Vartanyants, K. Mundboth, C. Mocuta, T. H. Metzger, J. Stangl, G. Bauer, T. Boeck, and M. Schmidbauer, *Phys. Rev. B* **78**, 121304 (2008).
- <sup>159</sup> A. Diaz, C. Mocuta, J. Stangl, B. Mandl, C. David, J. Vila-Comamala, V. Chamard, T. H. Metzger, and G. Bauer, *Phys. Rev. B* **79**, 125324 (2009).
- <sup>160</sup> “*X-Ray Interactions With Matter*”, available at [http://henke.lbl.gov/optical\\_constants/](#).
- <sup>161</sup> L. Libralesso, Ph.D. Thesis, Universite Joseph Fourier Grenoble 1, 2006, available at [http://tel.archives-ouvertes.fr/docs/00/13/46/38/PDF/PhDthesis\\_LibralessoLaure.pdf](#).

- <sup>162</sup> P. Zaumseil, *Rocking and Reflectivity Simulation Software (RCRefSimW)* (IHP, Frankfurt (Oder)).
- <sup>163</sup> W. Braun, *Applied RHEED: reflection high energy electron diffraction during crystal growth*, Springer Tracts in Modern Physics Vol. 154 (Springer, Berlin Heidelberg, 1999).
- <sup>164</sup> A. Ichimiya and P. I. Cohen, *Reflection High Energy Electron Diffraction* (Cambrdge University Press, Cambridge, UK, 2004).
- <sup>165</sup> J. F. Watts and J. Wolstenholme, *An Introduction to Surface Analysis by XPS and AES* (John Wiley & Sons, West Sussex, 2003).
- <sup>166</sup> S. Hüfner, *Photoelectron Spectroscopy: Principles and Applications*, 3rd ed. (Springer, Berlin, 2003).
- <sup>167</sup> A. Einstein, Ann. Phys. **17**, 132 (1905).
- <sup>168</sup> J. F. Moulder, W. F. Stickle, P. E. Sobol, and K. D. Bomben, *Handbook of X-ray Photoelectron Spectroscopy* (Perkin-Elmer Corporation, Eden Prairie, 1992).
- <sup>169</sup> D. Briggs and M. P. Seah, *Practical surface analysis Volume 1 - Auger and X-ray Photoelectron Spectroscopy*, 2nd ed. (Wiley, West Sussex, 1990).
- <sup>170</sup> C. J. Powell, A. Jablonski, I. S. Tilinin, S. Tanuma, and D. R. Penn, J. Electron Spectrosc. Relat. Phenom. **98-99**, 1 (1999).
- <sup>171</sup> H. Bubert and H. Jenett, *Surface and Thin Film Analysis: Principles, Instrumentation, and Applications* (Wiley-VCH Verlag GmbH, Weinheim, 2002).
- <sup>172</sup> J. C. Vickerman, *Surface Analysis: The Principal Techniques* (John Wiley & Sons, West Sussex, 1997).
- <sup>173</sup> D. Briggs and M. P. Seah, *Practical Surface Analysis Volume 2 - Ion and Neutral Spectroscopy*, 2nd ed. (John Wiley & Sons, West Sussex, 1992).
- <sup>174</sup> J. Goldstein, D. E. Newbury, D. C. Joy, C. E. Lyman, P. Echlin, E. Lifshin, L. C. Sawyer, and M. J. R. Healy, *Scanning Electron Microscopy and X-ray Microanalysis* 3rd ed. (Springer, New York, 2002).
- <sup>175</sup> D. B. Williams and B. C. Carter, *Transmission Electron Microscopy: A Textbook for Materials Science* (Plenum Press, New York, 1996).
- <sup>176</sup> P. J. Goodhew, *Specimen Preparation For Transmission Electron Microscopy Of Materials* (Oxford University Press, USA, 1984).
- <sup>177</sup> I. Németh, Ph. D. Thesis, Phillips-Universität Marburg, Marburg, 2008, available at <http://archiv.ub.uni-marburg.de/diss/z2008/0142/>.
- <sup>178</sup> M. Haider, H. Rose, S. Uhlemann, E. Schwan, B. Kabius, and K. Urban, Ultramicroscopy **75**, 53 (1998).
- <sup>179</sup> H. H. Rose, Sci. Technol. Adv. Mater. **9**, 014107 (2008).

- <sup>180</sup> P. Goodhew, D. Brook, B. Tanovic, A. Green, and I. Jones, “*TEM Basics*”, University of Liverpool, (2000), available at <http://www.matter.org.uk/tem/>.
- <sup>181</sup> T. Akatsu, C. Deguet, L. Sanchez, F. Allibert, D. Rouchon, T. Signamarcheix, C. Richtarch, A. Boussagol, V. Loup, F. Mazen, J.-M. Hartmann, Y. Campidelli, L. Clavelier, F. Letertre, N. Kernevez, and C. Mazure, Mater. Sci. Semicond. Process. **9**, 444 (2006).
- <sup>182</sup> A. Sakai, T. Tatsumi, and K. Aoyama, Appl. Phys. Lett. **71**, 3510 (1997).
- <sup>183</sup> A. Giussani, O. Seifarth, P. Rodenbach, H. J. Müsing, P. Zaumseil, T. Weisemöller, C. Deiter, J. Wollschläger, P. Storck, and T. Schroeder, J. Appl. Phys. **103**, 084110 (2008).
- <sup>184</sup> T. Schroeder, I. Costina, A. Giussani, G. Weidner, O. Seifarth, C. Wenger, P. Zaumseil, C. Mocuta, T. H. Metzger, D. Geiger, and H. Lichte, J. Appl. Phys. **102**, 034107 (2007).
- <sup>185</sup> A. Giussani, P. Rodenbach, P. Zaumseil, J. Dabrowski, R. Kurps, G. Weidner, H. J. Müsing, P. Storck, J. Wollschläger, and T. Schroeder, J. Appl. Phys. **105**, 033512 (2009).
- <sup>186</sup> N. Franco, N. P. Barradas, E. Alves, A. M. Valléra, R. J. H. Morris, O. A. Mironov, and E. H. C. Parker, Mater. Sci. Eng., B **124-125**, 123 (2005).
- <sup>187</sup> P. Zaumseil, A. Giussani, P. Rodenbach, and T. Schroeder, Phys. Status Solidi A **206**, 1809 (2009).
- <sup>188</sup> P. Zaumseil, A. Giussani, O. Seifarth, T. Arguirov, M. A. Schubert, and T. Schroeder, Solid State Phenom. **156-158**, 467 (2010).
- <sup>189</sup> B. D. Cullity and S. R. Stock, Elements of x-ray diffraction, 3rd ed. (Prentice Hall, Upper Saddle River, 2001), Chap. 2.
- <sup>190</sup> R. Drosd and J. Washburn, J. Appl. Phys. **53**, 397 (1982).
- <sup>191</sup> W. Bollmann, *Crystal Defects and Crystalline Interfaces* (Springer-Verlag, Berlin, 1970).
- <sup>192</sup> M. E. Twigg, E. D. Richmond, and J. G. Pellegrino, Appl. Phys. Lett. **54**, 1766 (1989).
- <sup>193</sup> D. B. Holt and B. G. Yacobi, *Extended Defects in Semiconductors* (Cambridge University Press, Cambridge, 2007).
- <sup>194</sup> P. Zaumseil and T. Schroeder, J. Appl. Phys. **104**, 023532 (2008).
- <sup>195</sup> U. Beck, T. H. Metzger, J. Peisl, and J. R. Patel, Appl. Phys. Lett. **76**, 2698 (2000).
- <sup>196</sup> D. Luebbert, J. Arthur, M. Sztucki, T. H. Metzger, P. B. Griffin, and J. R. Patel, Appl. Phys. Lett. **81**, 3167 (2002).
- <sup>197</sup> A. Boulle, D. Chaussende, L. Latu-Romain, F. Conchon, O. Masson, and R. Guinebretiere, Appl. Phys. Lett. **89**, 091902 (2006).
- <sup>198</sup> A. Boulle, D. Chaussende, F. Pecqueux, F. Conchon, L. Latu-Romain, and O. Masson, Phys. Stat. Sol. (A) **204**, 2528 (2007).
- <sup>199</sup> P. Klang, V. Holý, J. Kuběna, R. Štoudek, and J. Šik, J. Phys. D: Appl. Phys. **36** **38**, A105 (2005).

- <sup>200</sup> F. Ernst and P. Pirouz, *J. Appl. Phys.* **64**, 4526 (1988).
- <sup>201</sup> E. Polychroniadis, M. Syväjärvi, R. Yakimova, and J. Stoemenos, *J. Cryst. Growth* **263**, 68 (2004).
- <sup>202</sup> P. Zaumseil, *J. Phys. D: Appl. Phys.* **41**, 135308 (2008).
- <sup>203</sup> Y. Takagi, H. Yonezu, K. Samonji, T. Tsuji, and N. Ohshima, *J. Cryst. Growth* **187**, 42 (1998).
- <sup>204</sup> A. Sakai and T. Tatsumi, *Phys. Rev. Lett.* **71**, 4007 (1993).
- <sup>205</sup> L. H. Kuo, L. Salamanca-Riba, B. J. Wu, G. M. Haugen, J. M. DePuydt, G. Hofler, and H. Cheng, *J. Vac. Sci. Technol. B* **13**, 1694 (1995).
- <sup>206</sup> T. Schmidt, R. Kroger, T. Clausen, J. Falta, A. Janzen, M. Kammler, P. Kury, P. Zahl, and M. Horn-von Hoegen, *Appl. Phys. Lett.* **86**, 111910 (2005).
- <sup>207</sup> D. Dentel, J. L. Bischoff, T. Angot, and L. Kubler, *Surf. Sci.* **402-404**, 211 (1998).
- <sup>208</sup> T. Schroeder, A. Giussani, H.-J. Muessig, G. Weidner, I. Costina, C. Wenger, M. Lukosius, P. Storck, and P. Zaumseil, *Microelectron. Eng.* **86** 1615 (2009).